A journey towards coalescence: from minor galaxy mergers to massive black hole binary evolution

Cognome / Surname: Varisco   Nome / Name: Ludovica

Matricola / Registration number: 777348

Abstract

According to the hierarchical formation paradigm, galaxies form through mergers of smaller entities and super massive black holes (SMBHs), if present, tend to shrink to the center where they may form binary systems. The formation and evolution of SMBH binaries, and in particular their coalescence timescale, are particularly relevant for current and future facilities aimed at detecting the gravitational-wave signal produced by the SMBH close to coalescence.

In the first part of my thesis, I explore the impact of the rotation of the stellar host on the efficacy of bound binary hardening, driven by three-body stellar interactions. In line with previous investigations, I observe that the center of mass (CoM) of a prograde super massive black hole binary (SMBHB) within a rotating environment starts moving around the system's center on nearly circular orbits shortly after the formation of a bound SMBHB. In our simulations, the oscillation radius is approximately 0.25 (0.1) times the binary influence radius for equal-mass SMBHBs (SMBHBs with a mass ratio of 1:4). Conversely, retrograde binaries remain fixed at the center of the host. The binary shrinking rate is twice as rapid when the binary CoM exhibits net orbital motion, facilitated by a more effective repopulation of the loss cone, even in our spherical stellar systems.

I develop a model that captures the CoM oscillations of prograde binaries. I posit that the gain in CoM angular momentum per unit time correlates with the internal angular momentum of the binary, resulting in the majority of the displacement being triggered by stellar interactions around the time of formation of a bound SMBHB. However, the subsequent enhancement of angular momentum is ultimately suppressed by the impact of dynamical friction.

In the second part of my thesis I investigate minor galactic merger, particularly focusing on the effect of tidal forces in eroding the satellite mass. While most of the studies targeting this process are based on N-body simulations, the high computational cost makes a complete parameter exploration prohibitive. Semi-analytic approaches represent a valid alternative, but they require ad-hoc prescriptions for the mass loss of the merging galaxies in minor mergers due to tidal stripping, which is not commonly considered or at most assumes very idealised geometries. In this work, I propose a novel, effective model for the tidal stripping in axisymmetric potentials, to be implemented in semi-analytic models. I validate my semi-analytic approach against N-body simulations considering different galaxy sizes, inclinations, and eccentricities, finding only a moderate dependence on the orbit eccentricity. In particular, I find that, for almost circular orbits, our model mildly overestimates the mass loss, and this

is due to the adjustment of the stellar distribution after the mass is removed. Nonetheless, the model exhibits a very good agreement with simulations in all the considered conditions, and thus represents an extremely powerful addition to semi-analytic calculations.

This thesis contributes to a deeper knowledge of SMBHBs and their path towards the coalescence. When combined with a detailed modelling of galactic mergers, where SMBHB are formed, it can provide valuable insights for future LISA (Amaro-Seoane et al., 2023) predictions.

Contents

1

Super massive black holes and galaxy mergers

Black holes (BHs) – regions of spacetime with such extreme gravity that not even light can escape – stand as some of the most captivating objects in our Universe. As one of the most fascinating predictions of Einstein's General Relativity, these objects have drawn scientific attention since the early decades of the 20th century. Although their existence is now well-established, just a few decades ago they were considered mere mathematical curiosities, with severe doubts about their actual existence in Nature. The concept of a black hole dates back to 1783 when Michell proposed the idea of "dark stars" (Michell, 1784), which, according to Newtonian dynamics, were believed to possess enough mass to prevent any object from escaping their gravitational pull. In 1915, Einstein published the theory of General Relativity, laying the foundation for the study of black holes. However, for a long time, the idea that Nature could permit the existence of such extreme and exotic objects was deemed impossible, to the extent that Einstein himself, in 1939, employed his own general relativity to argue against the possibility of black hole existence (Einstein, 1939).

Subsequently, extensive research has been conducted on general relativity and, in particular, on black holes.

In the 1960s, the discovery of the first quasar by Schmidt (1963) marked a pivotal moment making the concept of black holes transitioning from being purely theoretical to a subject of active investigation. This breakthrough initiated an era of intense efforts in searching for BH candidates.

1.1 Astrophysical black holes

Despite being the most extreme environments in the Universe, astrophysical BHs are very simple entities, fully characterized by two parameters: mass and spin. From a theoretical point of view, the recipe to create a BH is very simple too. The only ingredients needed are a mass M and a physical process capable

of confining it within its horizon, whose linear size can be approximated by (or is equal to, in the case of a non-rotating BH) the Schwarzschild radius:

$$R_S = \frac{2GM}{c^2}, \tag{1.1}$$

where G is the gravitational constant, M is the BH mass and c is the speed of light. In this perspective, indeed, any object can turn into a BH, on the only condition that its mass is squeezed to a size smaller than R_S.

Due to the paucity of information about the BH spin, astrophysical BH are typically classified by their mass only: stellar-mass BHs, intermediate-mass BHs (IMBHs), and supermassive BHs (SMBHs). Stellar-mass black holes, with masses spanning the range $2M_\odot \lesssim M_\bullet \lesssim 100M_\odot$, are formed as a consequence of the gravitational collapse of massive stars. When massive stars reach the end of their lives, most of their material is ejected during a violent supernova event. If the mass of the resulting remnant exceeds the Tolman-Oppenheimer-Volkoff limit (Kippenhahn et al., 2012), it undergoes direct collapse into a BH. The first evidence of the existence of stellar-mass black holes arose in the 1970s with observations in X-rays of stellar binaries, identifying Cyg X-1 as the first candidate to host a BH of stellar origin (Webster & Murdin, 1972).

The high end of the BH mass distribution is populated by SMBHs, with masses ranging from $10^5 M_\odot$ up to several $10^{10} M_\odot$. The origin of these sources is still under debate. Among the plausible possibilities there is the collapse of popIII stars - stars of the first generation made up of the pristine gas from the cosmological nucleosynthesis - which may lead to the formation of a BH with a mass of about $100M_\odot$ (e.g. Heger et al., 2003; Madau & Rees, 2001). This BH seed then needs to steadily accrete mass to grow up to the enormous masses observed. Other possibilities include the direct collapse of gas clouds at the center of proto-galaxies (e.g. Haehnelt & Rees, 1993; Luo et al., 2018; Shlosman et al., 2016), runaway stellar collisions in dense stellar clusters, where the cluster does not collapse, but the central stars merge into a very massive star around $\sim 1000M_\odot$ (e.g. Devecchi & Volonteri, 2009; Devecchi et al., 2010, 2012; Reinoso et al., 2020), and the runaway merger of stellar-mass BHs in the cluster core, again leading to masses around $\sim 1000M_\odot$ (e.g. Lupi et al., 2014).

Bridging the gap between stellar BHs and SMBHs, IMBHs, including the population of seed SMBH formed through the mechanism above-mentioned, cover a mass range of $100M_\odot \lesssim M_\bullet \lesssim 10^5 M_\odot$. So far, only a handful of sources have been indicated as IMBH candidates. The reasons why this mass range is so poorly populated is uncertain. It is unclear whether there are physical processes that render these objects effectively rare in our Universe or if the reason is to be attributed to observational biases that make IMBHs challenging to detect.

1.2 Super massive black holes

SMBHs serve as fundamental building blocks in the formation and evolution of galaxies, making the understanding of their formation and evolution a fundamental objective in modern cosmology and astrophysics. Since their discovery in the 1960s, it has become clear that the highly energetic emissions characterizing quasars have a gravitational origin (see e.g. Salpeter, 1964; Zel'dovich & Novikov, 1964). Having excluded all alternative explanations, the luminosity of such sources has been attributed to the accretion of matter onto a lurking black hole. Further, given the Eddington limit, to justify the production of such enormous luminosities, the central engine should possess a mass millions or even billions time larger than the solar mass, thus providing strong indications of the existence of SMBHS.

1.2.1 SMBH and stellar host

It is now well known that SMBHs inhabits most of galactic nuclei featuring a sizable spheroidal stellar component, the latter being either the approximately spherical stellar distributions of elliptical galaxies, or the bulge component present in the centeral region of many spiral galaxies. The surface brightness profile $I(R)$ - where R represents the projected distance from the center of the galaxy - of spheroidal distribution of stars is typically well fitted with a simple parametric model called the Sérsic profile (Sersic, 1968):

$$\ln I(R) = \ln I(R_e) - b(n)\left[\left(\frac{R}{R_e}\right)^{1/n} - 1\right]. \tag{1.2}$$

Here, the b parameter is usually chosen such that R_e, the effective radius, coincides with the projected radius containing half of the total galaxy light. The shape parameter n, usually called Sérsic index, shows a dependence with the size of the stellar distribution, with higher values of n corresponding to a better fit for larger spheroids. Besides it simple form, the widespread use of the Sérsic profile is justified by the fact that it well fits the surface brightess of many galaxies over a vast range of radii.

SMBH influence on stellar dynamics

The gravitational field generated by a SMBH is so strong to significantly influence the dynamics of the surrounding material at distances up to million times the extent of its event horizon. The region wherein the gravitational potential dominates the dynamics of gas and stars is referred to as the "sphere of influence" of the SMBH. The outer boundary of this region is the "influence radius radius", r_m, and it is determined such that the enclosed mass in stars is twice the mass of the SMBH:

$$M_*(r < r_m) = 2M_\bullet. \tag{1.3}$$

An alternative definition for the influence radius, that we denote as r_h, has been proposed based on more easily measurable quantities. In this formulation, r_h is defined requiring that the circular velocity of a test particle, at a distance r_h from the SMBH, equals the velocity dispersion σ:

$$r_h = \frac{GM_\bullet}{\sigma^2}. \tag{1.4}$$

At $r = r_m$, the gravitational force is contributed to one-third by the SMBH and the remaining portion by the stars. At higher distances the SMBH's contribution becomes negligible, and the dynamics is dominated by the distribution of stars. Conversely, on smaller scales, as the distance approaches the event horizon, the velocities increase, reaching values of significant fractions of the speed of light. Here, general relativity effects must be taken into account to properly describe the orbital motions.

SMBH-host relations

Even if SMBHs are able to influence the motion of objects at distances of many orders of magnitude larger than their own event horizon, a comparison of the SMBH influence radius with the characteristic dimension of the whole galaxy shows that the influence sphere is just a tiny region of the entire host galaxy, r_h being $\sim 10^{-5} - 10^{-6} R_e$. Nonetheless, numerous observational studies have consistently demonstrated a tight correlation between the mass of SMBHs and the large-scale properties of their host galaxies. Suprisingly, the SMBH mass was found to correlate with the velocity dispersion of the stellar component of its host (e.g. Ferrarese & Merritt, 2000; Gebhardt et al., 2000; Gültekin et al., 2009; Tremaine et al., 2002). The $M_\bullet - \sigma$ relation proposed by (Gültekin et al., 2009) is:

$$\log(M/M_\odot) = (8.12 \pm 0.08) + (4.24 \pm 0.41)\log(\sigma/200\,\mathrm{km\,s^{-1}}) \tag{1.5}$$

The $M_\bullet - \sigma$ relation for a sample of 49 SMBH-host-galaxy pairs is shown in fig. 1.1.

 Similar correlations have been found to exist between the SMBH mass and the bulge luminosity in the K-band ($M_\bullet - L_{\mathrm{bulge}}$)(Kormendy & Richstone, 1995; Marconi & Hunt, 2003) and the bulge mass $M_\bullet - M_{\mathrm{bulge}}$(Häring & Rix, 2004; Magorrian et al., 1998; Marconi & Hunt, 2003).

 The small intrinsic scatter of the scaling relations between SMBHs and bulges has widely been interpreted with a co-evolutionary scenario (Di Matteo et al., 2005; Granato et al., 2004). The growth of SMBHs occurs primarily through the accretion of gas. As the SMBH attains sufficient mass - thus lying on the aforementioned relations -, the active galactic nucleus (AGN) feedback, which operates on galactic scales (Silk & Rees, 1998), becomes intense enough to suppress both accretion and star formation.
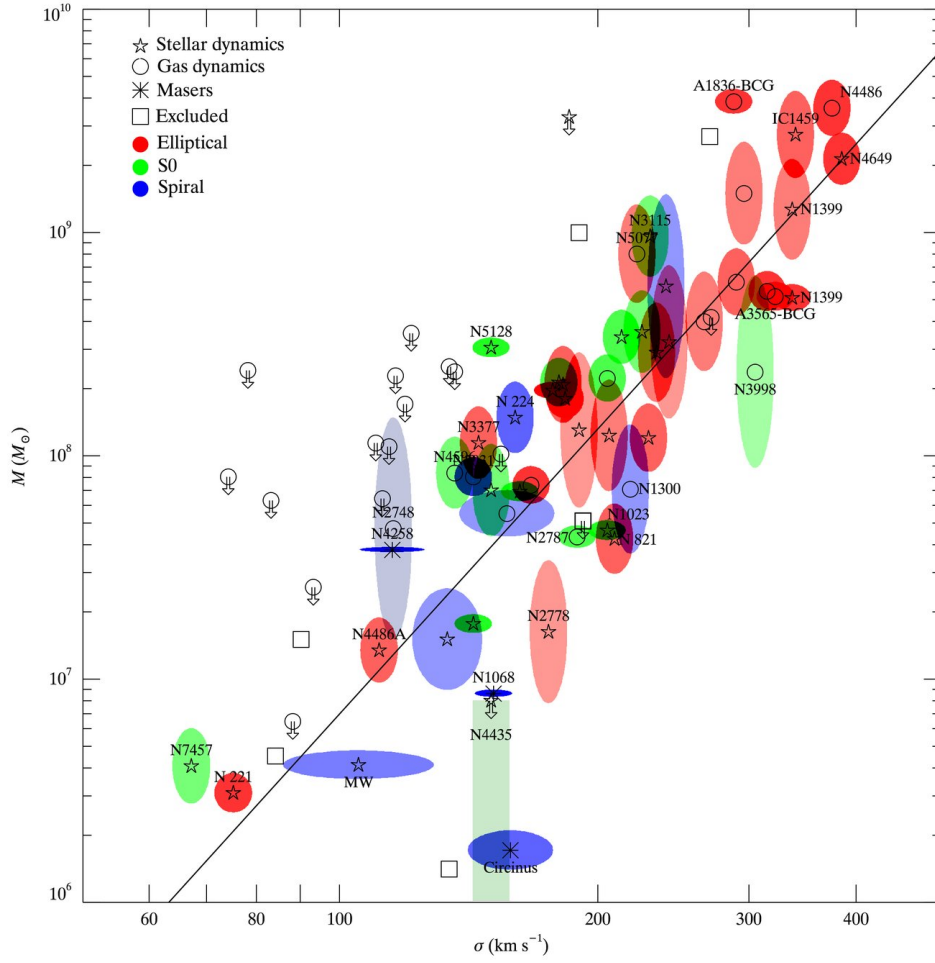
Figure 1.1: The plot, taken from (Gültekin et al., 2009), shows SMBH masses as a function of the stellar velocity dispersion for a sample of 49 sources. The black solid line display the best fit to the sample, given by eq. 1.5.

An alternative explanation explores a non-causal origin, negating the necessity for a synchronized growth of SMBHs and their host bulges. This explanation relies instead on a process of statistical convergence. If we consider an initially arbitrary distribution of $M_\bullet/M_*$ at high redshifts, repeated merging events may cause the mass ratios of black holes to bulges to converge to a linear relation. In this scenario, akin to the central limit theorem, if the number of mergers is sufficiently large, the extreme values in the initial distribution of $M_\bullet/M_*$ will be effectively averaged out (Jahnke & Macciò, 2011; Peng, 2007).

1.2.2 Observational techniques for SMBH mass estimates

Detecting SMBHs practically translates in the ability of measuring their mass $M_\bullet$. Various techniques have been developed for this purpose, which are primarly divided in two categories: direct and indirect methods (see e.g. Peterson, 2014, for a review). Direct methods are based on the dynamics of gas and star in the vicinity of the SMBH, being therefore, due to resolution limitations, feasible in a restricted number of cases. The most reliable technique is based on the detection of the orbital motion of individual stars accelerated by the SMBH gravity, as done in the case of Sgr A* at the center of the Milky Way (Genzel et al., 2010; Meyer et al., 2012). Other possibilities rely on fitting the dynamics of megamaser disks or detecting the line of sight velocity rise, which goes as:

$$v^2 \propto \frac{GM_\bullet}{r},\qquad(1.6)$$

in the integrated emission of the whole unresolved stars/gas population in the proximity of the SMBH. Finally, an alternative direct method is available for measuring $M_\bullet$ in Type I AGNs. These systems have a near face-on orientation with respect to our line of sight, therefore the innermost regions surrounding the central MBH remain unobscured by the dusty torus, allowing the nuclear continuum emission and the broad lines to be visible. For such sources, the method known as "reverberation mapping" can be employed, wherein the SMBH mass is measured using an analogous equation to eq. 1.6. Here the velocity v of the emitting gas is measured from the Doppler broadening of the gas emission lines, while the extension r of the emitting region - the Broad Line Region (BLR) - is estimated by the time delay in the variability of the broad emission lines with respect to the variability of the continuum emission.

On the contrary, indirect methods infer the SMBH mass using the phenomenological relations described above ($M_\bullet - \sigma$, $M_\bullet - L_{\text{bulge}}$ and $M_\bullet - M_{\text{bulge}}$). Despite being very useful for estimating the SMBH mass of a large number of sources, this methods inherently preclude the detection of potential modifications to these relations over cosmological timescales.

1.3   Galaxy mergers

Galaxies, along with the dark matter (DM) halos in which they are embedded, do not exist in isolation. The ΛCDM model of cosmology predicts a hierarchical aggregation of structures over cosmic time (Press & Schechter, 1974; White & Rees, 1978). In this framework, galaxies and their host DM halos experience growth through mergers with systems of comparable mass in the so-called "major mergers" ($q \gtrsim 1/4$, where q is the ratio between the more massive and the less massive systems), as well as through the accretion of smaller systems, leading to "minor mergers" ($q < 1/4$).

1.3.1   Minor mergers

While the literature extensively explores the effects of major mergers on the final mass and morphology of massive galaxies (e.g. Darg et al., 2010), recent studies emphasize the significant contribution that minor mergers can bring. Minor mergers occur frequently, with a recurrence approximately 3-4 times higher than major mergers in late epochs (e.g. Kaviraj et al., 2009), as indicated by both theoretical and observational studies. Although individual minor merger events may have a almost paltry impact on massive galaxies, their cumulative effect over cosmic time is substantial, influencing both the stellar content and the structural properties of the primary merging galaxy.

As we delve into further detail in the following section and in Chapter 4, the proper characterization the evolution of galaxies during mergers is crucial. This importance stems from the fact that these merging processes serve as the factories where binary SMBHs are formed and evolve.

1.3.2   Mass removal due to tidal forces

When minor mergers occur, satellite galaxies, while orbiting within their hosts, are subjected to tidal forces that remove part of their mass, sometimes leading to their complete disruption even after a single pericenter passage. Two main mechanisms have been identified for removing mass from the satellite, depending on the rapidity at which the external tidal field varies. When the satellite experiences a slowly changing tidal field, the effect of the tidal forces is that of stripping material from the outer regions of the satellite, forming a clear external boundary often called the tidal radius (R_t). This process is identified as *tidal stripping*. On the contrary, when the satellite undergoes a rapid change in the external tidal field, part of its orbital energy is converted into internal energy, leading to an overall heating of the satellite. The amount of energy injected into the system during fast pericenter passages and transferred to the stars can be enough to unbind a significant fraction of the satellite mass. This effect is known as *tidal heating* or *tidal shocking*.

Tidal heating

The most severe tidal heating takes place during close and fast encounters. An interaction gives rise to tidal shocking when the duration of the encounter is shorter compared to the satellite dynamical time.

Consider a system composed of a satellite galaxy orbiting within its host galaxy. We denote as $r_s(t)$ the trajectory of the satellite center in the inertial frame of the host, and with r the distance of a test star from the satellite center. The radius vector of the test star in the galaxy reference frame is $\mathbf{r}_* = \mathbf{r_s}(t) + \mathbf{r}$. Thus, the equation of motion can be written as:

$$\ddot{\mathbf{r}}_{\mathbf{s}} + \ddot{\mathbf{r}} = -\left(\frac{\partial \Phi_G}{\partial \mathbf{r_s}}\right)_{r_s} - \left(\frac{\partial \Phi_c}{\partial \mathbf{r}}\right)_{r_*} - \left(\frac{\partial^2 \Phi_G}{\partial \mathbf{r_s}\partial \mathbf{r_s}}\right)_{r_s} \cdot \mathbf{r} - ..., \tag{1.7}$$

where Φ_G and Φ_c are the potentials of the galaxy and the satellite respectively. The leading term $\partial \Phi_G/\partial \mathbf{r_s}$ in the above equation defines the trajectory of the satellite center, thus in the tidal approximation:

$$\ddot{\mathbf{r}} = -\left(\frac{\partial \Phi_c}{\partial \mathbf{r}}\right) - \left(\frac{\partial^2 \Phi_G}{\partial \mathbf{r_s}\partial \mathbf{r_s}}\right) \cdot \mathbf{r} \tag{1.8}$$

If the host galaxy is spherically symmetric, its gravitational potential can be expressed as:

$$\Phi_G = -\frac{GM(r)}{r} - 4\pi G \int_r^\infty \rho(r')r'dr', \tag{1.9}$$

from which the resulting tidal force per unit mass is:

$$\mathbf{F}_{\text{tid}} \equiv -\left(\frac{\partial^2 \Phi_G}{\partial \mathbf{r_s}\partial \mathbf{r_s}}\right) \cdot \mathbf{r} = \frac{GM_G}{r_s^3}[(3\mu - \mu')(\mathbf{n} \cdot \mathbf{r})\mathbf{n} - \mu\mathbf{r}], \tag{1.10}$$

where M_G is the total mass of the host and $\mathbf{n}$ is the direction to the satellite center, $\mu(r)$ and $\mu'(r)$ are defined as follows:

$$\mu(r) = \frac{M(r)}{M_s}, \tag{1.11}$$

and

$$\mu'(r) = \frac{\mathrm{d}\mu(r)}{\mathrm{d}\ln(r)}. \tag{1.12}$$

Under the impulsive approximation, i.e. assuming that the particle motions are negligible during the encounter, the change in the velocity of stars is given by:

$$\Delta\mathbf{v} = \int \mathbf{F}_{\text{tid}}\,\mathrm{d}t, \tag{1.13}$$

where the integral is evaluated over the satellite orbit. This time-dependent perturbation leads to a net heating of the satellite by increasing the stellar random motions. The corresponding averaged energy gain of stars with initial energy E is:

$$\langle \Delta E \rangle_E = \langle \frac{1}{2}(\Delta v)^2 \rangle \tag{1.14}$$

Assuming an eccentric orbit, the resulting velocity variation can be expressed as:

$$\Delta \mathbf{v} = \left(\frac{GM_G}{a^3} \right)^{\frac{1}{2}} \frac{1}{j(\alpha, e)} \{ (B_1 - B_3)x, (B_2 - B_3)y, B_3 z \}, \tag{1.15}$$

with:

$$B_1 = \int_{-\theta_m}^{\theta_m} \frac{3\mu(r) - \mu'(r)}{r/a} \cos^2 \theta \, d\theta, \tag{1.16}$$

$$B_2 = \int_{-\theta_m}^{\theta_m} \frac{3\mu(r) - \mu'(r)}{r/a} \sin^2 \theta \, d\theta, \tag{1.17}$$

$$B_3 = \int_{-\theta_m}^{\theta_m} \frac{\mu(r)}{r/a} d\theta. \tag{1.18}$$

In the above equations a is the host galaxy scale length, e is the satellite orbital eccentricity and j is its dimensionless angular momentum. α is a dimensionless parameter defined as the ratio between a and the pericenter distance R_p. Finally, the variable θ represents the position angle in polar coordinates. $\theta = 0$ corresponds to the pericenter, while $-\theta_m$ and θ_m refers to two subsequent apocenters. The change in the energy of stars is [1]:

$$\langle \Delta E \rangle_E = \frac{GM_G}{a^3} r^2 \frac{(B_1 - B_3)^2 + (B_2 - B_3)^2 + B_3^2}{6j^2(\alpha, e)} A(\omega, \tau). \tag{1.19}$$

Here, the term $A(\omega, \tau)$ is needed to account for adiabatic corrections, which depends only on the duration of the encounter τ and on the orbital frequency of the stellar particles in the satellite ω. Indeed, the impulsive approximation is only valid for the the least bound stars. For the highly bound stars, residing in the most internal regions of the satellite, the dynamical time can result to be significantly shorter than the duration of the encounter. For these particles, the pericenter passage is adiabatic, and the adiabatic invariants conservation prevents these stars to gain energy (see e.g. Spitzer, 1987).

The energy injected in the satellite during tidal shocks can be so high to unbind a large fraction of the satellite mass, and, in some cases, leading to its complete disruption even during a single pericenter passage.

---

[1]For the details of the derivation see Gnedin et al. (1999)

Tidal stripping

While the tidal shocks occur when the external tidal field changes rapidly in time, another effect drives the satellite mass loss in the opposite scenario, when the external tidal field is almost static: the tidal stripping.

In these context, a quantitative assessment of how mass is stripped from infalling satellite galaxies requires a careful estimation of the tidal radius. Beyond this limit, the object's material undergoes stripping due to tidal forces exerted by the larger host. First introduced by von Hoerner (1957) within the context of Milky Way globular clusters, the tidal radius was theoretically defined strictly for satellites following circular orbits, where it coincides with the position of L1/L2 Lagrange points (Binney & Tremaine, 1987). A different attempt to define such radius also for eccentric motion was explored by King (1962), who argued that instead of using the instantaneous value of the tidal radius along the orbit, satellites are truncated to the size indicated by the pericentric tidal radius. This is because the most significant mass truncation occurs in correspondence with the pericenter passage, while the internal relaxation does not proceed rapidly enough to increase the satellite size between two successive pericenter passages.

The idea under the definition of the King's tidal radius is the following. Consider a satellite galaxy orbiting within the potential of a *spherically symmetric* host galaxy. Let R_S and θ_s represent the polar coordinates specifying the location of the satellite center in relation to the host center. Consider a rotating coordinate system (x, y) with the origin at the center of the satellite, where the x-axis consistently points in the opposite direction to the host center. During the pericenter passage, stars situated at considerable distances from the satellite center will become unbound due to the tidal force exerted by the host, while stars in close proximity will remain bound. Consequently, the limiting radius, beyond which the satellite mass is stripped, can be identified as the distance from the satellite center along the direction connecting the centers of the two systems where a test star is neither accelerated toward the satellite nor toward the host. The acceleration of the satellite with respect to the host center at the pericenter can be evaluated as:

$$\frac{\mathrm{d}^2 R_S}{\mathrm{d}t^2} = -\frac{\mathrm{d}\Phi_G(R)}{\mathrm{d}R}\bigg|_{R_S} + R_S\,\Omega^2, \tag{1.20}$$

where Ω is the satellite angular velocity and $\Phi_G(R)$ the host galaxy potential. At the same moment, the acceleration of the test star, located at a distance R_* form the host center, is:

$$\frac{\mathrm{d}^2 R_*}{\mathrm{d}t^2} = \frac{\mathrm{d}\Phi_G(R)}{\mathrm{d}R}\bigg|_{R_*} - GM_S(|R_* - R_S|)\frac{(R_* - R_S)}{|R_* - R_S|^3} + R_*\,\Omega^2. \tag{1.21}$$

Here $M_S(R)$ is the mass profile of the satellite galaxy. Thus, the relative

acceleration results:

$$\frac{\mathrm{d}^2}{\mathrm{d}t^2}(R_* - R_S) = (R_* - R_S)\Omega^2 - \frac{\mathrm{d}\Phi_G(R)}{\mathrm{d}R}\bigg|_{R_*} + \frac{\mathrm{d}\Phi_G(R)}{\mathrm{d}R}\bigg|_{R_S} - GM_s(|R_* - R_S|)\frac{(R_* - R_S)}{|R_* - R_S|^3}$$

(1.22)

In the distant-tide approximation, where $|r_* - R_S| \ll R_S$, it becomes:

$$\frac{\mathrm{d}^2}{\mathrm{d}t^2}(R_* - R_S) \simeq \left(\Omega^2 - \frac{\mathrm{d}^2\Phi_G(R)}{\mathrm{d}R^2}\bigg|_{R_S} - \frac{GM_s(|R_* - R_S|)}{|R_* - R_S|^3}\right)(R_* - R_S). \quad (1.23)$$

The value of $|R_* - R_S|$ for which eq. 1.23 vanishes determines the amplitude of the tidal radius:

$$R_t = \left[\frac{GM_S(R_t)}{\Omega^2 - \frac{\mathrm{d}^2\Phi_G(R)}{\mathrm{d}R^2}\big|_{R_S}}\right]^{1/3}, \quad (1.24)$$

or alternatively:

$$R_t = R_S \left[\frac{M_S(R_t)/M_G(R_S)}{2 + \frac{\Omega^2 R_S^3}{GM_G(R_S)} - \frac{\mathrm{d}\ln M_G}{\mathrm{d}\ln R}\big|_{R_S}}\right]^{1/3}, \quad (1.25)$$

where $M_G(R)$ is the host galaxy mass distribution. In the approximation of circular orbits $\Omega = v_c(R)/R$, thus eq. 1.24 can be rewritten as:

$$R_t = R_S \left[\frac{M_S(R_t)/M_G(R_S)}{3 - \frac{\mathrm{d}\ln M_G}{\mathrm{d}\ln R}\big|_{R_S}}\right]^{1/3}. \quad (1.26)$$

Despite being widely used in literature, eqs. 1.24, 1.25, 1.26 represents only approximate estimations for the limiting radius generated by tidal forces on the satellite, and for this reason is worthwhile making some considerations:

1. The locus of points determined by the distances from the satellite at which the radial acceleration of a test star vanishes is not a spherical surface, and therefore cannot be defined by a single value of the tidal radius.

2. The above calculation neglects the impact of the internal motion of the satellite stars. In a more recent study, Read et al. (2006) derived an expression for the tidal radius taking into account different orbit types of the stars within the satellite: prograde, radial, and retrograde. The analysis revealed that the tidal radius for retrograde orbits exceeds that of radial orbits, which, in turn, is larger than the tidal radius for prograde orbits.

3. The definitions of R_t were derived under the assumption of distant tides, requiring that the separation between the centers of the two systems is significantly larger than R_t. This condition holds true for quasi-circular and distant orbits. However, on eccentric orbits, the pericenter may be located at distances from the host center that are comparable to or even smaller than the dimensions of the satellite.

4. Eqs. 1.24, 1.25, 1.26, along with the majority of attempts to estimate the tidal radius, have predominantly focused on spherically symmetric host galaxies. This makes them particularly well-suited for investigating systems such as merging DM halos (see e.g., van den Bosch et al., 2018). However, a significant portion of systems, where the primary object undergoing minor mergers deviates considerably from spherical symmetry, is not adequately addressed by these methods. Examples include the disk component of spiral galaxies with flattened potentials or regions near galactic bars characterized by a strongly non-axisymmetric potential.

Chapter 4 of the present thesis will be fully devoted to address these issues, proposing a new prescription for the mass loss of satellite galaxies driven by tidal-stripping in generic potentials.

1.3.3   Dynamical friction

Another process that plays a pivotal role in the evolution of satellite galaxies – and massive perturbers in general – is dynamical friction. When a massive object with mass M_S and velocity $\mathbf{v_S}$ moves across a collisionless system[2] consisting of particles with mass $m \ll M_S$ (the field stars), it is subjected to a dragging force, known as *dynamical friction*, through which energy and momentum are transferred from M_S to the background particles. Intuitively, dynamical friction can be explained by the fact that two-body interactions cause particles to exchange energy in such a way that the whole system evolves towards the thermodynamic equilibrium. In systems composed of multiple mass populations, each characterized by a different mass m_i, due to two-body interactions the system will tend to the energy equipartition, where locally the mean kinetic energy per particle is the same for all the populations $m_1\langle v_1^2\rangle = m_2\langle v_2^2\rangle = ... = m_n\langle v_n^2\rangle$. In the scenerio of a massive perturber travelling within a sea of lighter stars, there are two distinct populations: the first composed of the subject mass M_S while the second includes all the field stars. Since $M_S \gg m$ and given the fact that in an inhomogeneous self-gravitating system particles at similar radii have comparable orbital velocities, the subject mass will have typically a larger kinetic energy with respect to the surrounding field stars with which it interacts. As a consequence, the overall effect of the encounters will be a net tendency of the subject mass to lose energy and momentum. A schematic representation of the effect of dynamical friction is shown in fig. 1.2

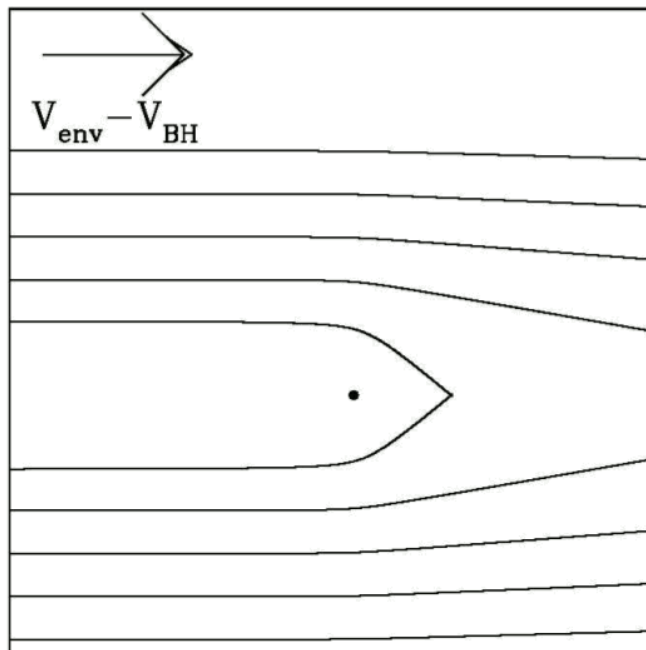[2]Refer to sec. 2.1.2 for the definition of a collisionless system

Figure 1.2: Schematic representation of DF acting on a massive perturber moving within a system of lighter collisionless particles. Image credits: Massimo Dotti.

The first derivation for the dynamical friction was performed by Chandrasekhar (1943a), who considered the deceleration of a massive perturber moving in a sea of background particles as the cumulative effect of uncorrelated hyperbolic two-body encounters with field stars. When a point-like particle with mass M_S and initial velocity $\mathbf{v_S}$ undergoes to a two-body interaction with another point-like particle of mass m, the change in the subject velocity, decomposed along the directions parallel and perpendicular to the initial direction of $\mathbf{v_S}$ will be:

$$|\Delta\mathbf{v}_{S,\parallel}| = \frac{2mbv_\infty^3}{G(M_S+m)^2}\left[1 + \frac{b^2v_\infty^4}{G^2(M_S+m)^2}\right]^{-1},$$ (1.27)

and

$$|\Delta\mathbf{v}_{S,\perp}| = \frac{2mv_\infty}{(M_S+m)}\left[1 + \frac{b^2v_\infty^4}{G^2(M_S+m)^2}\right]^{-1},$$ (1.28)

where b is the impact parameter of the encounter and $v_\infty = |\mathbf{v}_m - \mathbf{v}_S|$ is the relative velocity of the two particles before the encounter. The above equations neglect the contribution of the external potential generated by all the other particles, thus the derivation in valid only under the assumption of an infinite and homogeneous distribution of field stars. As the massive perturber moves within its host system of background particles, it will be subjected to repeated encounters, each occurring with different values of b and v_∞. The total velocity change of $\mathbf{v}_S$ due to the cumulative effect of all the interactions is given by:

$$\left(\frac{\mathrm{d}\mathbf{v}_S}{\mathrm{d}t}\right)_{(\parallel/\perp)} = \int\int \Delta\mathbf{v}_{S_{(\parallel/\perp)}}(b,\mathbf{v}_m)\frac{\mathrm{d}N}{\mathrm{d}b\,\mathrm{d}^3\mathbf{v}_m\,\mathrm{d}t}\mathrm{d}b\,\mathrm{d}^3\mathbf{v}_m,$$ (1.29)

with N number of interactions. For a homogeneous distribution of particles, the distribution function $f(\mathbf{x},\mathbf{v})$ only depends on $\mathbf{v}$, and the net velocity change in the perpendicular direction vanishes due to the compensation of the induced changes, effectively averaging to zero. The dominant contribution determining dynamical friction is therefore the velocity change occurring along the parallel direction. Finally, the number of interactions with impact parameter in the range $[b, b+\mathrm{d}b]$ occurring in a time interval of Δt is:

$$\frac{\mathrm{d}N}{\mathrm{d}b\,\mathrm{d}^3\mathbf{v}_m\,\mathrm{d}t} = 2\pi b|\mathbf{v}_m - \mathbf{v}_S|f(\mathbf{v}_m).$$ (1.30)

Using eq. 1.27 and eq. 1.30 in eq. 1.29 and integrating over the impact parameter, leads to:

$$\left(\frac{\mathrm{d}\mathbf{v}_S}{\mathrm{d}t}\right) = \left(\frac{\mathrm{d}\mathbf{v}_S}{\mathrm{d}t}\right)_\parallel = -4\pi G^2(M_S+m)m\int \mathrm{d}^3\mathbf{v}_m\,f(\mathbf{v}_m)\ln\Lambda\frac{\mathbf{v}_S-\mathbf{v}_m}{|\mathbf{v}_S-\mathbf{v}_m|^3}$$ (1.31)

where:

$$\ln \Lambda \equiv \frac{1}{2} \ln \left[1 + \frac{b_{\max}}{b_{\min}} \right] \simeq \ln \left(\frac{b_{\max}}{b_{\min}} \right) \tag{1.32}$$

is called *Coulomb Logarithm* and is simply the logarithm of the ratio between the maximum and minimum impact parameters. $b_{\max}$ is generally chosen as the maximum scale length of the system under study in order to prevent 1.29 to logarithmically diverge for large values of b.[3] The minimum impact parameter $b_{\min}$ is typically chosen to correspond to the impact parameter of a 90°-deflection in the two-body interaction $b_{min} = b_{90} \equiv G(M_S + m)/v_\infty^2$. Although the minimum impact parameter depends on v_∞, in principle requiring integration of $\ln \Lambda$ over the velocity space, the large ratio $b_{\max}/b_{\min}$ allows for the approximation of v_∞ with a constant value v_{typ} representing a typical encounter speed. In this way the Coulomb logarithm can be placed outside the integration.

Under the assumption of an isotropic velocity distribution, and recalling that $M_S \gg m$, the dynamical friction acceleration results:

$$\begin{aligned}
\mathbf{a_{DF}} = \frac{d\mathbf{v}_S}{dt} &= -16\pi^2 G^2 M_S m \ln \Lambda \left[\int_0^{v_s} f(v_m) v_m^2 \, dv_m \right] \frac{\mathbf{v}_S}{v_S^3} \\
&= -4\pi M_S \left(\frac{G}{v_s} \right)^2 \ln \rho(< v_S) \frac{\mathbf{v}_S}{v_S^3},
\end{aligned} \tag{1.33}$$

with $\rho(< v_S)$ representing the density of field stars with a pre-encounter velocity lower than the subject particle. In the limit of low velocities the dynamical friction acceleration is linear in v_S, while as the velocities approaches to v_S it decreases as v_S^{-2}.

Accurately characterizing dynamical friction acting on massive perturbers is crucial in various astrophysical scenarios. In the context of this work, it holds significant relevance on multiple fronts. Firstly, it determines the orbital decay time of SMBHBs, strongly shaping the chance of forming a bound binary system that may potentially undergo coalescence within a Hubble time. Secondly, it plays a pivotal role in the evolutionary dynamics of satellite galaxies involved in minor mergers, establishing a tight connection with the mass removal triggered by tidal forces imparted by the host galaxy. Dynamical friction induces the sinking of the satellite towards the host center, where tidal forces are more pronounced, thereby facilitating mass removal. Conversely, the process of tidal-driven mass loss, through the erosion of the satellite's mass, diminishes the efficiency of dynamical friction, thus decelerating its decay within the host system.

---

[3]The introduction of a large scale cutoff is intrinsically connected with the fact that the gravitational interaction (as well as the electromagnetic one) is a long large interaction that formally vanishes only at infinity.

Limitations and extensions of Chandrasekhar formula

Despite being extensively used in literature, it is important to recall that the Chandrasekhar formula has been derived under the simplistic assumption of an infinite and homogeneous stellar background. For finite-size host systems, with masses $M_h \gg M_S$, the value of the maximum impact parameter is usually chosen to correspond to the size of the host system r_h, and if one considers the subject mass to be on a circular orbit about the host center, the Coulomb logarithm can be approximate as $\ln \Lambda \simeq \ln(M_h/M_S)$. More recent studies showed that 1.33 can be quite easily extended to well reproduce the result of N-body simulations for more realistic systems by adopting position-dependent maximum and minimum impact parameter (see e.g. Hashimoto et al., 2003; Just et al., 2011; Just & Peñarrubia, 2005).

Another crucial assumption in the Chandrasekhar formula is that the massive perturber is a point-like particle. However, an accurate prescription for dynamical friction is essential for predicting the orbital evolution and decay time of extended objects, such as satellite galaxies, globular clusters, and dark matter subhalos. Therefore, for systems with non-zero sizes, the physical dimensions of the perturber must be considered. It has been demonstrated that the extension of the perturber contributes to dynamical friction only by influencing the amplitude of the Coulomb logarithm, which results to be smaller compared to cases of point-like perturbers. In this context, White (1976) showed that the Coulomb logarithm for extended bodies can be expressed as:

$$\ln \Lambda = \frac{1}{M_S} \int_0^{b_{\max}} I_S^2(b) b^3 \, \mathrm{d}b, \tag{1.34}$$

with

$$I_S(b) = \frac{1}{M_S} \int_0^{b_{\max}} I_S^2(b) b^3 \, \mathrm{d}b, \tag{1.35}$$

Moreover, if the mass of the extended massive perturber is allowed to vary, i.e. if the mass loss due to tidal forces is taken into account, eq. 1.3.3 can be rewritten as:

$$\ln \Lambda = \ln \left(\frac{b_{\max}}{k R_t} \right). \tag{1.36}$$

Here R_t is the perturber tidal radius, while $k = 1/M_S \int_0^{b_{\max}} I_S^2(b) b^3 \, \mathrm{d}b$ which for realistic density distribution $k \approx 0.2 - 0.3$ (White, 1976).

Dynamical friction in flattened and rotating systems

Eq. 1.33, along with all its aforementioned extensions, is valid when the host system exhibits an isotropic velocity distribution. Conversely, in situations

where the host system displays a net rotation - as initially observed by Dotti et al. (2006) in the context of SMBH in circumnuclear discs - a massive object undergoes orbit circularization as a result of its interaction with the surrounding medium. Specifically, massive perturbers corotating orbits tend to decrease in eccentricity, while initially counter-rotating orbits tend to reverse the angular momentum direction to align it with the angular momentum of the background, than proceeding towards circularization. Interestingly, this effect is observed to arise independently of the (stellar or gaseous) nature of the surrounding medium.

In contrast to isotropic scenarios, the dynamical friction acceleration exerted on massive perturbers within rotationally supported discs does not consistently oppose the motion of the massive object relative to the center of the whole system. Instead, for counter-rotating or co-rotating eccentric orbits, the dynamical friction acceleration instantaneously acts in the opposite direction with respect to the relative velocity between the massive perturber and the matter in the near proximity. In such configuration, the main dependence of the dynamical friction direction is given by the velocity more than on the density profile. Despite this tendency toward corotational circularization - often called "drag towards circular corotation" - emerged from several numerical studies (see e.g. Callegari et al., 2011; Dotti et al., 2006; Fiacconi et al., 2013), only recently Bonetti et al. (2021a, 2020a) proposed a semi-analytical prescription for the dynamical friction induced on massive perturbers by flattened and rotationally supported hosts, successfully validated against N-body experiments. Fig 1.3 shows the comparison of the semi-analytical model proposed in Bonetti et al. (2021a) with N-body simulations.

The resulting expression for the dynamical friction acceleration induced by a rotating disc is qualitatively very similar to the Chandrasekhar formula and is given by:

$$\mathbf{a}_{\text{DF, disk}} = -2\pi G^2 \ln(1 + \Lambda^2) m_p \rho_p(R, z) \times$$

$$\times \left(\text{erf}(X) - \frac{2X e^{-X^2}}{\pi^{1/2}} \right) \frac{\mathbf{v}_{\text{rel}}}{|\mathbf{v}_{\text{rel}}|^3}. \tag{1.37}$$

Here, m_p is the perturber mass and $\rho_d(R, z)$ is the disk density profile, while $\mathbf{v}_{\text{rel}} = \mathbf{v}_{\text{p}} - \mathbf{v}_{\text{rot}}(R)$ and $X = |\mathbf{v}_{\text{rel}}|/(\sqrt{2}\sigma_R)$, with σ_R representing the radial velocity dispersion. Eq. 1.3.3 is derived under the assumption that the velocities of the disk particles are distributed as an isotropic Gaussian with center in the local rotational velocity. Finally, in the Coulomb logarithm the maximum impact parameter is taken to be equal to the disk scale height $b_{\text{max, disk}} = z_d$, while the minimum impact parameter is given by:

$$b_{\text{min, disk}} = \frac{G m_p}{v_{\text{rel}}^2 + \sigma_R^2}, \tag{1.38}$$

thus setting a minimum effective distance for the massive perturber-disk particles interactions.
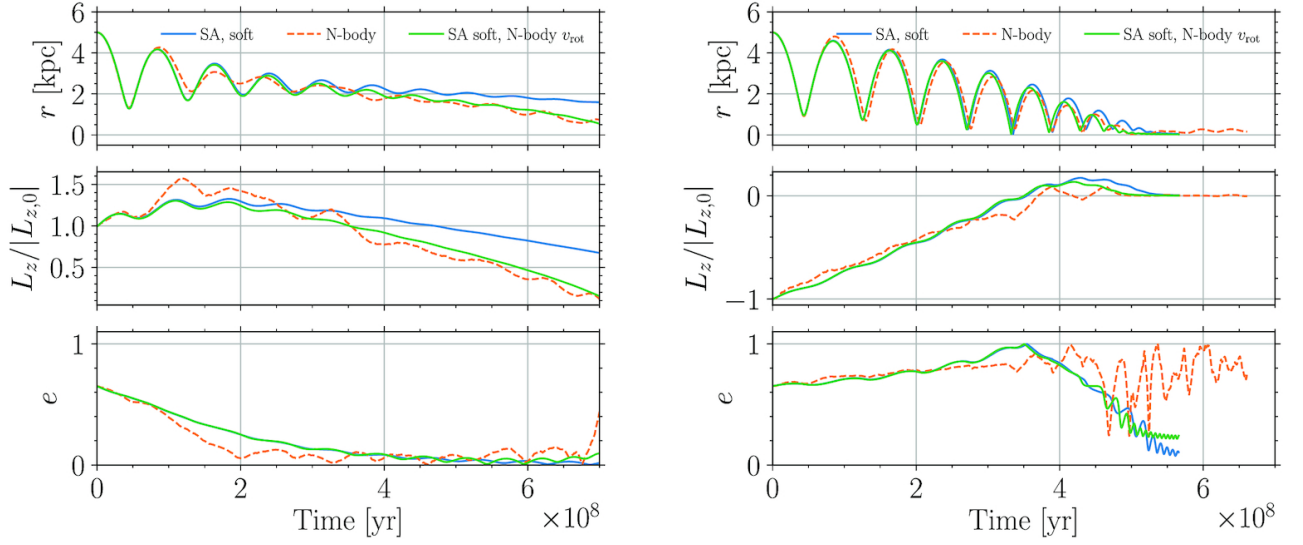
Figure 1.3: From top to bottom, evolution of the radial separation, the z component of the angular momentum- normalized to its initial value- and eccentricity for a massive perturber in a multi-component host galaxy, composed of a DM halo, an exponential disk and a central bulge. Solid lines show the evolution obtained from the semi-analytical model (in blue with $v_{\rm rot}$ computed as , and in green using a $v_{\rm rot}$ profile fitted on the N-body simulations), while the orange dashed line displays the result from the N-body runs. Left panels refers to a system hosting a co-rotating massive perturber, while right panels show the same system but in an intitially counter-rotation configuration. Image credits: Bonetti et al. (2021a).

1.4   Super massive black hole binaries

As discussed in the previous sections, the ΛCDM model of hierarchical formation of cosmic structures predicts galaxies to aggregate in a "bottom-up fashion", with a large number of galactic merger occurring along the cosmic time. Concurrently it is well-established that the center of most galaxies is inhabited by a SMBH. Therefore as natural outcome of galaxy mergers, binary SMBH (SMBHB) are expected to form (Begelman et al., 1980a). From observations of galactic centers, a number of SMBHB candidates have been proposed on the basis on different observational features. These features includes, "X-shaped" jets emission displayed by some radio galaxies (Capetti et al., 2002; Leahy & Williams, 1984; Wang et al., 2003, e.g.), which has been proposed to be associated to a sudden re-orientation of the BH spin direction induced by the merger with another SMBH (Ekers et al., 1978). Double-lobed radio galactic sources (Schoenmakers et al., 2000), showing a pair - internal and external- of radio emitting structures aligned along the same axis, suggest a phase of interruption of the jet emission. This suspension is typically ascribed to a temporary quenching of the accretion activity - and of the jet emission it powers- possibly caused by the infalling secondary SMBH (Liu et al., 2003). The presence of binary SMBHs can also been inferred by periodic variability in the optical emission (Pursimo et al., 2000; Valtaoja et al., 2000). This can arise as a consequence of tidal perturbations due to the secondary SMBH approaching the primary BH accretion disc, thus leading to a boost in the accretion activity, which result in a peak in the light-curve (Lehto & Valtonen, 1996; Sillanpaa et al., 1988). Alternatively, the torques exerted on the accretion disc by the presence of the companion SMBH induce disc precession. As a consequence jets start oscillating, thus generating a modulation of the light intensity produced by Doppler-boosting (Katz, 1997). Another observational feature that can hint for the presence of SMBHBs is the shift in the velocity peak of the broad lines, emitted from a region close to at least one SMBH, in comparison to the velocity of the host galaxy traced from the velocity peak of the narrow lines. The narrow line region, being situated further out from the center of the host, is not affected by the motion of the binary (Begelman et al., 1980b).

More recently, spatially resolved pairs of emitting regions embedded in a common host galaxy have been discovered, at projected separations of few hundreds of parsec or lower, which have been suggested as potential candidates for SMBH pairs. X-ray observation performed with Chandra showed the presence of dual AGNs at the center of both the starburst galaxy NGC 6240 (Komossa et al., 2003) and the spiral galaxy NGC 3393 (Fabbiano et al., 2011). The most compact spatially resolved SMBHB discovered so far is hosted in the radio galaxy 0402+379. VLBA observations of this source show a inter-SMBH projected distance of ~ 7 pc (Rodriguez et al., 2006).

The investigation of how SMBHB form, evolve and reach the coalescence has always been a focal point in astrophysical research. This significance is

particularly highlighted by the critical role SMBHBs play in understanding the connection between SMBHs and their host galaxies, as detailed in sec. 1.2.1. In the last decade the interest toward these sources has surged as the gravitational waves (GW) astronomy era begun.

Gravitational waves represent distortions in space-time induced by the acceleration of massive objects, propagating through the Universe at the speed of light carrying with them invaluable information about the systems that generated them. First predicted as a consequence of Einstein's General Relativity (Einstein & Lawson., 1961), the actual direct observation of gravitational waves occurred only $\sim$ half a century later, specifically in 2015 when the Laser Interferometer Gravitational-Wave Observatory (LIGO) collaboration (Abbott et al., 2016) revealed signals produced by the coalescence of a stellar-mass BH binary.

The final evolutionary stage of SMBHBs is expected to produce the loudest source of gravitational waves in the Universe. These sources will be the main target of the forthcoming gravitational wave observatory LISA (Laser Interferometer Space Antenna, Amaro-Seoane et al., 2023), covering the frequency range of $10^{-4} - 1$ Hz. This ambitious experiment will be able to detect the last month-to-year of the pre-merger phase of SMBHBs in the mass range $10^4 - 10^6 M_\odot$. At even lower frequencies ($10^{-9} - 10^{-7}$ Hz) Pulsar Timing Array (PTA) (Agazie et al., 2023; Antoniadis et al., 2023) experiments are constantly monitoring the time of arrival of radio pulses from arrays of millisecond pulsars in our Galaxy. Tiny deviations from the expected time of arrival of the radio signals can reveal the specific pattern perturbation ascribable to low frequency GWs. The main PTA collaborations have recently claimed the detection of a GW signal possibly generated by the incoherent superposition of the GW radiation emitted by the whole SMBHB population across the Universe (Agazie et al., 2023; EPTA Collaboration et al., 2023; Reardon et al., 2023). With refined and prolonged observations the nature of the signal will be dissected and will possibly also reveal single SMBHBs sources shining in the GW spectrum. The possibility of exploring such low frequency ranges is crucial for many astrophysical reasons. Concerning SMBHBs, it will allow to obtain unprecedented estimations of SMBH masses, spins and distances.

1.4.1   SMBHB evolution

As first presented in the seminal paper by Begelman, Blandfors and Rees (Begelman et al., 1980b), the journey towards the coalescence of SMBHBs in gas-poor environments can be roughly divided in three subsequent phases.

Pairing phase and dynamical friction driven inspiral

As a consequence of galactic mergers the SMBHs hosted at the center of the progenitor systems are injected in the newly formed galaxy remnant. In the case of major mergers the two SMBHs linger bound to their high density cusps,
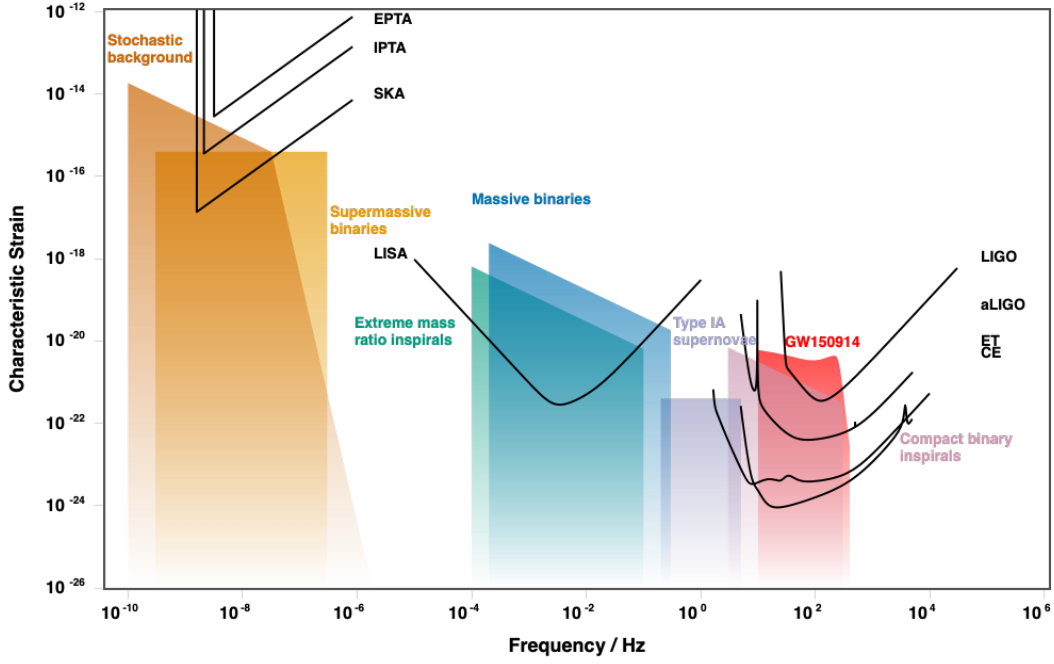
Figure 1.4: Plot of the characteristic strain versus GW frequency for various sources. The black solid lines represent sensitivity curves corresponding to different GW detectors. Image credits: http://gwplotter.com.

gradually decaying toward the center of the whole system surrounded by their original stellar environment, until the two nuclear galactic cores merge and the two SMBHs start orbiting as individual entities. Conversely, in minor mergers tidal forces erodes the mass of the smaller galaxy and the secondary SMBH sinks towards the primary SMBH with just a partial or, if tidal forces are strong enough and the satellite core is loosely bound, even no residual of the progenitor stellar environment. In both scenarios, the initial stage of the evolution of the SMBH pair is driven by dynamical friction (see section 1.3).

This initial pairing phase is characterized by a fast shrinking of the inter-SMBH distance as dynamical friction efficiently extract energy and angular momentum from the SMBHs. The typical decay time can be estimated on the basis of eq. 1.33. Considering a SMBH of mass $M_\bullet$, embedded in a stellar system, whose density profile is assumed to be that of an isothermal sphere $\rho(r) = \sigma^2/(2\pi G r^2)$, with a Maxwellian velocity distribution, the dynamical friction decay time results (Binney & Tremaine, 2008):

$$t_{\mathrm{DF}} = \frac{19\mathrm{Gyr}}{\ln \Lambda} \left(\frac{R_i}{5\mathrm{kpc}} \right)^2 \frac{\sigma}{200\mathrm{kpc\, s^{-1}}} \frac{10^8 M_\odot}{M}, \tag{1.39}$$

where R_i is the initial distance of the SMBH from the host system center. This estimate assumes the scenario of a SMBH orbiting within the main host galaxy completely deprived of its original stellar host, thus possibly leading to a substantial overestimation of the real SMBH decay time and a consequest

21

inaccurate estimate SMBHB merger rates. A more realistic dynamical friction timescale was proposed by (Dosopoulou & Antonini, 2017), which consider the sinking SMBH to be surrounded by a tidally-truncated remnant of the original stellar host[4], yielding to the following estimate for the dynamical friction decay time:

$$t_{\mathrm{DF}}^{\mathrm{ss}} \sim 0.15 \mathrm{Gyr} \frac{2}{\ln \Lambda} \left(\frac{R_e}{10 \mathrm{kpc}} \right) \left(\frac{\sigma}{300 \mathrm{km\,s^{-1}}} \right)^2 \left(\frac{\sigma_{ss}}{100 \mathrm{km\,s^{-1}}} \right)^{-3}, \qquad (1.40)$$

with R_e representing the effective radius of the primary host galaxy. σ and σ_{ss} are the velocity dispersions of the primary galaxy and of the SMBH stellar surrounding, respectively.

Slingshot ejection phase

After a galaxy merger the SMBHs have an initially large mutual separation ($\sim$ kpc), thus the BH-pair in the first stages of its evolution is unbound.

However, as the SMBHs migrate towards the nuclear region, the relative distance diminishes, eventually leading to formation of a bound binary system when the SMBH separation reaches the influence radius (see eq. 1.3) of the less massive BH $a_f = a_{h2}$. The time corresponding to the instant of the binary formation is denoted as t_f.

Once the binary has formed, its orbit can be described trough the Keplerian orbital parameters. Consider a SMBHB whose constituent objects have masses $M_{1\bullet}$ and $M_{2\bullet}$. $M_{1\bullet}$ refers to the most massive SMBH, such that the mass ratio is $q = M_{2\bullet}/M_{1\bullet} \leq 1$. Let $M_\bullet = M_{1\bullet} + M_{2\bullet}$ be the total mass, $\mu = M_{1\bullet}M_{2\bullet}/M_\bullet$ the binary reduced mass and r the binary separation. Neglecting the contribution from the surrounding stars, the binary binding energy is:

$$E = -\frac{GM_{1\bullet}M_{2\bullet}}{2a}. \qquad (1.41)$$

Here a denotes the binary semi-major axis, which together with the eccentricity e is defined as:

$$a = \left(\frac{2}{r} - \frac{v^2}{GM} \right)^{-1}, \qquad (1.42)$$

$$e = \left(1 - \frac{h^2}{GM_\bullet a} \right)^{1/2}, \qquad (1.43)$$

where $h = |\mathbf{r} \times \mathbf{v}|$ is the binary specific angular momentum and v is the module of the relative velocity.

---

[4]In this derivation, the truncation radius for the SMBH stellar surrounding is assumed to be the Hill's radius, defined as $R_t = (GM_h r^2/4\sigma^2)^{1/3}$ (see Binney & Tremaine, 2008), where M_h is the total mass of the primary host galaxy.

After the formation of a bound SMBHBs, the strong self-gravity makes the action of dynamical friction to become less efficient. This happens as the bound system partially decouples from the stellar environment. This means that only quite nearby stars can effectively interact with the SMBHBs. Those stars play a crucial role in further reducing the binary separation, which occurs through the slingshot ejection mechanism. Under the combined effect of both slingshot ejection and dynamical friction, the binary undergoes a phase of fast decrease in the relative separation between the BHs. However, as the system becomes more tightly bound and reaches the so-called *hard binary separation*:

$$a_h = \frac{GM_\bullet}{4\sigma^2}, \tag{1.44}$$

the binary shrinking slows down. Indeed, at this stage dynamical friction becomes totally inefficient and the slingshot ejection becomes the only efficient mechanism for extracting energy and angular momentum from the binary.

Practically, the slingshot mechanism is a complex three-body interaction involving the SMBHB and stars in its close proximity. When a field star passes at a distance of few times the the binary semi-major axis from the SMBHB, the latter preferentially transfers energy and angular momentum to the interacting star due to the tendency of the system toward energy equipartiton. Due to the huge mass difference, the amount of energy gained by the star in the interaction can be sufficient to cause the star to be expelled from the system. As a consequence, after each encounter, the binary becomes more tightly bound. The cumulative effect of many successive interaction will make the SMBHB progressively tighter (or harder using the terminology of stellar binaries evolving in stellar clusters).

The rate at which the binary semi-major axis shrinks as a consequence of interactions with the surrounding stars is commonly referred to as the *binary hardening rate*, denoted by s, and is defined as follows:

$$s \equiv \left(\frac{\mathrm{d}}{\mathrm{d}t}\right)\frac{1}{a} = H\frac{G\rho_*}{\sigma_*}, \tag{1.45}$$

where ρ_* and σ_* represent the mass density and velocity dispersion of the surrounding stellar system, respectively, while H is a dimensionless parameter that parametrizes the efficiency of energy transfer between the SMBHBs and stars. The value of the hardening rate parameter H can be estimated through three-body scattering experiments, as conducted in previous studies such as Quinlan (1996) and Sesana et al. (2006), resulting in $H \approx 15 - 18$.

If the stellar reservoir that fuels the three body interactions is assumed to be unlimited - which we will see that is not the case in real SMBHBs - the time required for a binary to shrink its semi-major axis to a value a is via slingshot ejection is (Colpi, 2014):

$$t_{\mathrm{hard}} \approx \frac{\sigma}{\pi G\rho_* a} \approx 70\mathrm{Myr}\left(\frac{\sigma_*}{100\mathrm{kms}^{-1}}\right)\left(\frac{10^{-3}\mathrm{pc}}{a}\right)\left(\frac{10^4 M_\odot \mathrm{pc}^{-3}}{\rho}\right). \tag{1.46}$$

Interestingly, the hardening timescale increases with decreasing a. This hints to a possible binary stalling that can arise at small binary separations.

Gravitational waves emission and binary coalescence

If the slingshot ejection mechanism is efficient enough to bring the SMBHs at a separation of $\sim 10^{-2} - 10^{-3}$ pc, further hardening of the binary occurs through the emission of GWs, which efficiently reduces the SMBHB separation eventually leading the binary to coalesce. A first investigation of the GW emission from two point-like masses orbiting each other under the mutual gravitational influence was conducted by Peters (1964). In his seminal work, Peters presented a model for GW emission and provided an approximate expression detailing the consequent evolution of the binary eccentricity and semi-major axis:

$$\left.\frac{\mathrm{d}a}{\mathrm{d}t}\right|_{\mathrm{GW}} = -\frac{64}{5}\frac{G^3}{c^5}\frac{M_{1\bullet}M_{2\bullet}M_{\bullet}}{a^3(1-e^2)^{7/2}}\left(1 + \frac{73}{24}e^2 + \frac{37}{96}e^4\right) \tag{1.47}$$

$$\left.\frac{\mathrm{d}e}{\mathrm{d}t}\right|_{\mathrm{GW}} = -\frac{304}{15}\frac{G^3}{c^5}\frac{M_{1\bullet}M_{2\bullet}M_{\bullet}}{a^4(1-e^2)^{5/2}}e\left(1 + \frac{121}{304}e^2\right). \tag{1.48}$$

Those equations reveal that the rate at which the binary evolves is a strong function of the separation, meaning that only very tight binaries can substantially shrink via GW emission on timescales shorter than the age of the Universe. Additionally, as appear clear from eq. 1.48, GW emission causes the orbital eccentricity to decrease. From eq. 1.47 it is possible to estimate the time required for the binary to coalesce through GW emission, under the simplifying assumption of a constant eccentricity:

$$t_{\mathrm{GW}} = \frac{5}{256}\frac{c^5}{G^3}\frac{1}{F(e)}\frac{a^4}{\mu M_{\bullet}} \approx 580\,\mathrm{Gyr}\,\frac{1}{F(e)}\left(\frac{a}{0.1\mathrm{pc}}\right)^4\left(\frac{\mu}{10^7 M_{\odot}}\right)^{-1}\left(\frac{M_{\odot}}{10^8 M_{\odot}}\right)^{-2}, \tag{1.49}$$

with $F(e) = (1-e^2)^{7/2}\left(1+\frac{73}{24}e^2+\frac{37}{96}e^4\right)$. From the definition of $F(e)$ it is possible to infer that the binary shrinking via GW emission is more efficient for highly eccentric binaries (i.e. close pericentre passages) for which the coalescence time result to be significantly smaller.

1.4.2   Final parsec problem and possible solutions

In the framework of the SMBHB formation and evolution discussed in the previous section, the transition between the stellar driven hardening phase and the GW emission regime is recognized as a bottleneck in the binary path towards coalescence. A generic star can undergo an efficient slingshot ejection during its interaction with the SMBHB only when on a sufficiently centrophilic orbit,

such that its periapsis distance is comparable to the binary semi-major axis. This criterion is essential for the efficient extraction of energy from the binary during the encounter and can be expressed as a condition on the magnitude of the angular momentum L of the interacting stars, which must satisfy

$$L \leq L_{\mathrm{LC}} = \sqrt{2GM_{\bullet}a}. \tag{1.50}$$

The region of the phase-space populated by the stars with angular momenta lower than L_{LC} is denoted as *loss-cone*(Merritt, 2013). When a star interacts with the SMBHB in such a way that it undergoes a slingshot ejection, it leaves the central region of the host galaxy and is consequently removed from the binary loss cone. Repeated interaction result in a gradual depletion of the binary loss cone, which is efficiently emptied within a dynamical time. The ultimate fate of the binary critically hinges on the efficiency with which new stars are led to repopulate the loss cone. If the loss cone refilling is inefficient, the binary hardening ceases, making the binary to stall at separations of the order of ~ 1 pc thus preventing the binary from reaching the GW emission phase and the final coalescence. This scenario became known as the *Final parsec problem*(Milosavljević & Merritt, 2001).

To overcome the binary stallation, the most direct mechanism capable of repopulating the binary loss cone is two-body relaxation (Milosavljević & Merritt, 2003a; Valtonen, 1996; Yu, 2002). However, the relaxation timescale - over which two-body relaxation takes place - exceeds the Hubble time in the majority of massive galaxies hosting SMBHB of $\sim 10^6 M_{\odot}$ or more, making this process highly inefficient.

Several alternative processes have been proposed in the literature to efficiently replenish the loss cone on timescales shorter than the age of the Universe. The so-called "secondary slingshot" mechanism involves repeated interactions between the SMBHB and a star. This star, having undergone acceleration in a prior encounter with the binary, failed to acquire sufficient energy to completely escape the system (Milosavljević & Merritt, 2003b), thus possibly undergoing repeated interactions with the binary before being definitively expelled from the central region of the host, where the binary resides.

Moreover, as proposed by (Perets & Alexander, 2008), the presence of extended massive perturbers, such as clusters or giant molecular clouds, promote the relaxation process which can become significantly more efficient if compared to the stellar relaxation alone.

Another mechanism that can affect the refilling of the loss cone is the Brownian motion of the binary center of mass induced by repeated recoils resulting from interactions with stars. As the slingshot ejection process proceeds, stars are progressively ejected from the host nuclear region, causing a reduction in the central density distribution of stars. Consequently, the potential well responsible for maintaining the binary at the center of the host becomes shallower, allowing for a wider binary wandering. This, in turn, permits interactions with an increased number of stars(Bortolas et al., 2016; Chatterjee et al., 2003).

All the possible solutions of the final parsec problem mentioned so far apply for gas-poor environments. Escala et al. (2005) investigated the impact of nuclear gas discs on the evolution and hardening of SMBHBs. They found that in the initial stages of the binary pairing the relative distance between the SMBHs is decreased due to the dynamical friction exerted by the surrounding gaseous medium. In the later phases, the gas distribution responds by forming an ellipsoidal over-density whose axis rotates lagging behind the binary major axis. In this configuration, the resulting gravitational torques exerted on the binary promote continuing loss of angular momentum, thus reducing the binary semi-major axis down to distances at which GW emission becomes efficient.

Returning to collisionless system, a very efficient way to refill the binary loss cone, which has been claimed to be the ultimate solution of the final parsec problem (Gualandris et al., 2017; Vasiliev et al., 2014; Yu, 2002), is the deviation of the host galaxy potential from the spherical symmetry naturally arising as a consequence of galaxy mergers. In spherical potentials, the total specific angular momentum L of stars is conserved along their orbits. Consequently, once the majority of stars initially populating the loss cone are expelled, no physical processes can efficiently lead to loss cone refilling. Conversely, in host potential deviating from spherical symmetry, the total angular momentum of each stars is not conserved and instead undergoes oscillations exerted by the torques induced by the non-spherical potential. Thus, in such configurations a larger fraction of stars during their evolution can at some point have small enough total angular momenta such that $L < L_{\rm LC}$. In axisymmetric systems, the angular momentum of stars is conserved only along the direction parallel to the symmetry axis of the host L_z. In such galaxies, it is possible that some stars initially laying out of the loss cone (due to their total angular momentum exceeding $L_{\rm LC}$) have the conserved component of the angular momentum $L_z < L_{\rm LC}$. Such stars may at some point attain a total angular momentum $L \sim L_z < L_{\rm LC}$, thus entering the loss cone and interacting with the binary. Finally if the host potential is triaxial, none of the angular momentum components of a star is conserved, and during its evolution can at some point have $L < L_{\rm LC}$ (Merritt & Vasiliev, 2011; Poon & Merritt, 2004).

This scenario suggests that the final parsec problem may arise as a consequence of the oversimplified assumption of the purely spherical symmetry of the host galaxy, and that the collisionless loss-cone refilling in more realistic systems may efficiently lead the binary to the GW emission phase with the subsequent coalescence.

Numerous N-body experiments have been conducted to substantiate this scenario, starting with two initially isolated merging galaxies (Gualandris & Merritt, 2012; Khan et al., 2011; Preto et al., 2011) and subsequently tracking the evolution of the SMBHB from its initial phases. These investigations have demonstrated that the collisionless loss cone repopulation, occurring in more realistic, merger-induced non-spherical systems, efficiently shrink the binary separation, facilitating its coalescence with estimates ranging between ~ 10

Myr and 10 Gyr (Khan et al., 2016, 2012), i.e. generally well within the Hubble time.

However due to the limitation in the number of particles that can be simulated using direct summation methods, typically $N \lesssim 10^7$, the reliability of these results has not been completely verified. This limitation introduces concerns about the robustness of the results. Indeed, restricted number of particles may accentuate the Brownian motion of the binary center of mass (Merritt, 2001b) and induce unrealistically efficient two-body relaxation (Vasiliev et al., 2014). These effects may lead to a significant underestimation of the time required for the binary to achieve coalescence.

In ch. 3 I extensively investigate another possible mechanism of collisionless loss cone repopulation: the impact of the rotation of the host galaxy spherical bulge on the evolution and hardening of SMBHBs.

2

Galaxy models and numerical codes

This chapter is dedicated to the exploration of stellar dynamics within galaxies. Here, the fundamental concept of stellar dynamics is introduced, emphasising its significance in understanding the behaviour of stars within galactic environments. The N-body problem is discussed in detail, highlighting the distinction between collisional and collisionless systems. Furthermore, I provide an insight into the numerical codes utilised for performing the numerical simulations presented in this work, along with a comprehensive overview of the galactic models employed in this thesis. This chapter serves as a foundation for understanding the behaviour of the stellar component of galaxies, setting the stage for the subsequent investigations presented in this thesis.

2.1 Stellar dynamics

Albeit being the weakest among the fundamental forces in nature, at least 29 orders of magnitude weaker than the other forces at subatomic scales, gravity dominates at large distances. The vast majority of astrophysical systems, from planetary systems up to the large-scale structures in the Universe can be treated as an ensamble of point-like masses gravitationally interacting among each others.

The branch of astrophysics that tackles this problem is stellar dynamics, which aims at statistically describing the evolution of stellar systems influenced by mutual gravitational attraction. Stellar dynamics encompasses the study of isolated or interacting self-gravitating systems. The latter being defined as systems whose dynamics is completely determined by their mass distribution. Examples of self-gravitating systems include stellar clusters and galaxies, and, on larger scales and under specific conditions, extend to galaxies within clusters and even the clustering of galaxies.

2.1.1   Nbody problem

The *N-body problem* is the long-standing issue of predicting individual motions of a system of N particles interacting with each other under their mutual gravitational attraction solely. Considering such a system, equations of motion governing the dynamics are:

$$\ddot{\mathbf{r}}_i = -G \sum_{j=1,\, j\neq i}^{j=N} m_j \frac{\mathbf{r}_i - \mathbf{r}_j}{|\mathbf{r}_i - \mathbf{r}_j|^3}. \tag{2.1}$$

Here, $\mathbf{r}_i$ and m_i are the position and mass of the i-th particle. Eq. 2.1 is analytically solvable only for system with a number of particle $N < 3$ - however, under specific conditions also systems with $N = 3$ allow for analytical solutions, such as in the case of the "restricted three-body problem". For larger numbers of particles, the resolution of the equations of motion necessitates the application of numerical methods. First N-body simulations dates back to 1960s. In 1960, von Hoerner (von Hoerner, 1960) conducted the first computer simulation for a 16-body system. Just few years later, Aarseth started his seminal work, becoming in 1963 the first to reach $N = 100$ (Aarseth, 1963). Since then, the rapid development and optimization of N-body simulations have promoted a significant increase in the number of simulated particles, which, in accordance with Moore's Law, has seen an approximately twofold increase every two years. Nowadays, N-body simulations can be performed including a large number of particles, with $N \sim 10^{11}$ for collisionless simulations and $N \sim 10^6$ for the collisional ones. These two distinct classes of simulations have been specifically tailored for different astrophysical systems, as elucidated below.

2.1.2   Collisional vs collisionless systems

Gravitational systems can be essentially divided into two categories: *collisional* and *collisionless* systems. This distinction is based on whether the two-body relaxation timescale t_{rel} is shorter than the characteristic lifetime of the system (collisional systems) or not (collisionless systems). The relaxation time is defined as the timescale over which the two-body encounters between stars cause a significant change in the stars orbital energy and angular momentum. In other words, after one relaxation time a star in the system has lost memory of its initial conditions. A standard definition of the relaxation time is (Spitzer, 1987):

$$t_{\mathrm{rel}} = \frac{\sigma^3}{G^2 m_* \rho \ln \Lambda}, \tag{2.2}$$

where σ is the one-dimensional stellar velocity dispersion, m_* is the mass of a single star, ρ is the density of stars, and $\ln \Lambda$ is the Coulomb logarithm. The

relaxation time can also be express as a function of the crossing time of the system $t_C \equiv R/\sigma$, where R is the typical radius of the system:

$$t_{\text{rel}} \sim \frac{N}{\ln N} t_C \tag{2.3}$$

Galaxies are typically composed of 10^{11} stars and are just few hundred crossing times old, thus - a part for their nuclear region- are well approximated as collisionless systems.

Collisional dynamics concerns those systems for which stellar interactions are efficient within the system life-time. Conversely, in collisionless systems, encounters between stars are negligible, and its components can be treated as moving within the gravitational potential of a smooth distribution of mass.

2.1.3   Collisionless Boltzmann equation

Since in collisionless systems individual stellar interactions are negligible, the stars can be represented by means of a *distribution function* (DF) $f(\mathbf{x}, \dot{\mathbf{x}}, t) \geq 0$. At any time t, the number of particles in the six-dimensional volume element $\mathrm{d}\mathbf{x}^3 \mathrm{d}\dot{\mathbf{x}}^3$ of the phase space centered in $(\mathbf{x}, \dot{\mathbf{x}})$ is given by $f(\mathbf{x}, \dot{\mathbf{x}}, t) \, \mathrm{d}\mathbf{x}^3 \mathrm{d}\dot{\mathbf{x}}^3$. The spatial density and the gravitational potential generated by the stellar distribution can be expressed as:

$$\rho(\mathbf{x}, t) = \int \mathrm{d}^3\dot{\mathbf{x}} \, f(\mathbf{x}, \dot{\mathbf{x}}, t), \tag{2.4}$$

$$\Phi(\mathbf{x}, t) = -G \int \mathrm{d}^3\mathbf{x}' \, \frac{\rho(\mathbf{x}', t)}{|\mathbf{x} - \mathbf{x}'|} = -G \int \int \mathrm{d}\dot{\mathbf{x}} \mathrm{d}\mathbf{x}' \frac{f(\mathbf{x}, \dot{\mathbf{x}}, t)}{|\mathbf{x} - \mathbf{x}'|}, \tag{2.5}$$

respectively. If the trajectories of stars are continuous and smooth, the DF f obeys a continuity equation (Binney & Tremaine, 2008):

$$\frac{\partial f}{\partial t} + \dot{\mathbf{x}} \cdot \frac{\partial f}{\partial \mathbf{x}} - \frac{\partial \Phi}{\partial \mathbf{x}} \frac{\partial f}{\partial \dot{\mathbf{x}}} = 0, \tag{2.6}$$

where the accelerations have been written as $\ddot{\mathbf{x}} = -\partial\Phi/\partial\mathbf{x}$. Eq. 2.6 is known as the *collisionless Boltzmann equation* and states that the phase-space density of the fluid around a specific star remains unchanged. In a steady state, i.e. if $\partial f/\partial t = 0$, f is constant along the trajectories. Moreover, $\partial f/\partial t = 0$ also implies $\partial\Phi/\partial t$, which means that the trajectories of stars are the orbits determined by the time-independent gravitational potential $\Phi(\mathbf{x})$.

Both the avenues of investigation presented in the present thesis involve the study of collisionless systems.

2.2   N-body codes

In this section I briefly describe the numerical codes used in the present work.

2.2.1 Force softening

Consider a collisionless system composed of N particle. Let r_i and m_i be the position and the mass of the a subject particle. The gravitational potential felt by the subject particle due to the presence of a second point mass m_j at r_j is:

$$\Phi_{ij} \equiv \Phi(\mathbf{r}_i) = -G \frac{m_i m_j}{|\mathbf{r}_i - \mathbf{r}_j|}. \tag{2.7}$$

This form of the potential makes numerically solving the N-body problem a quite difficult task. Indeed, as the distance between the two bodies approaches zero, both gravitational potential in eq. 2.7 and the gravitational force $\mathbf{F}_{ij} = -\nabla \Phi_{ij}$ diverges to infinity, giving rise to the so-called *ultraviolet divergence*. This divergence is completely unphysical in collisionless systems since the gravitational potential to be modelled is smooth, and is caused by the particle sampling. This may lead to an incorrect system evolution. A widely used method to overcame the ultraviolet divergence is the introduction of the *softening parameter* ϵ. In this approximation, the gravitational potential $\Phi(\mathbf{r}_i)$ felt by a particle and generated by the contribution of all the other bodies is replaced by:

$$\Phi(\mathbf{r}_{ij}) = -G \sum_{i=1,\, i \neq j}^{i=N} S(r_{ij}, \epsilon) m_i m_j, \tag{2.8}$$

where the function $S(r_{ij}, \epsilon)$ is the *softening kernel density* and $r_{ij} = |\mathbf{r}_i - \mathbf{r}_j|$. Consequently, the gravitational force exerted on the subject particle can be expressed as:

$$\mathbf{F}_i = -G m_i \sum_{i=1,\, i \neq j}^{i=N} S_f(r_{ij}, \epsilon) m_j \frac{\mathbf{r}_i - \mathbf{r}_j}{r_{ij}}. \tag{2.9}$$

Here $S_f(\mathbf{r}_{ij}, \epsilon)$ represents the force softening kernel, which is the first derivative of $S(\mathbf{r}_{ij})$ with respect of r_{ij}. The force softening kernel employed in the evaluation of the force suppresses the divergence at small separation -thus making collisionless simulation more realistic-, while decreases as $r_{ij^{-2}}$ for separations much larger than ϵ. The most commonly used form of the softening kernel function is that of the Plummer softening:

$$S(\mathbf{r}_{ij}, \epsilon) = -\frac{1}{\sqrt{r_{ij}^2 + \epsilon^2}}. \tag{2.10}$$

With this expression, the softened gravitational force takes the form of the force acting between a point-like mass and a spherical Plummer distribution with scale radius ϵ.

2.2.2 HiGPUs

The investigation of the hardening of SMBHBs driven by the encounters with single stars detailed in ch. 3 was carried out with the direct-summation N-body code HiGPUs (Capuzzo-Dolcetta et al., 2013), which combines the efficiency of GPUs as computational accelerators used for the evaluation of pairwise forces, with the precision of a high order Hermite integrator. The coarse-grained parallelization ensures a one-to-one correspondence between the MPI processes and the computational nodes, with the MPI process managing all the available GPUs per node.

Hermite scheme

The equation of motion in HiGPUs are integrated using a 6th order Hermite predictor-corrector integrator with individual blocked timesteps.

Consider system composed of N bodies, at a time t_0, the i-th particles has position $\mathbf{x}_{i,0}$, velocity $\mathbf{v}_{i,0}$, acceleration $\mathbf{a}_{i,0}$, and acceleration time derivatives $\dot{\mathbf{a}}_{i,0}$, $\ddot{\mathbf{a}}_{i,0}$, $\dddot{\mathbf{a}}_{i,0}$ [1] The first step of the integrator consists of predicting the particle velocity and acceleration. These quantities can be predicted at a time $t_1 > t_0$ using:

$$\mathbf{r}_{i,1\,\text{pred}} = \mathbf{r}_{i,0} + \mathbf{v}_{i,0}\Delta t + \frac{1}{2}\mathbf{a}_{i,0}\Delta t^2 + \frac{1}{6}\dot{\mathbf{a}}_{i,0}\Delta t^3 + \frac{1}{24}\ddot{\mathbf{a}}_{i,0}\Delta t^4 + \frac{1}{120}\dddot{\mathbf{a}}_{i,0}\Delta t^5, \quad (2.11)$$

$$\mathbf{v}_{i,1\,\text{pred}} = \mathbf{v}_{i,0} + \mathbf{a}_{i,0}\Delta t + \frac{1}{2}\dot{\mathbf{a}}_{i,0}\Delta t^2 + \frac{1}{6}\ddot{\mathbf{a}}_{i,0}\Delta t^3 + \frac{1}{24}\dddot{\mathbf{a}}_{i,0}\Delta t^4, \quad (2.12)$$

$$\mathbf{a}_{i,1\,\text{pred}} = \mathbf{a}_{i,0} + \dot{\mathbf{a}}_{i,0}\Delta t + \frac{1}{2}\ddot{\mathbf{a}}_{i,0}\Delta t^2 + \frac{1}{6}\dddot{\mathbf{a}}_{i,0}\Delta t^3, \quad (2.13)$$

where $\Delta t = t_1 - t_0$. The particle acceleration, along with its first and second derivatives can be evaluated directly, thus not requiring any differentiation, using the predicted position, velocity and acceleration, through the following relations:

$$\mathbf{a}_{i,1} = \sum_{j=1,j\neq i}^{j=N} \mathbf{a}_{ij,1} = \sum_{j=1,j\neq i}^{j=N} m_j \frac{\mathbf{r}_{ij}^{\ 3}}{r_{ij}}, \quad (2.14)$$

$$\dot{\mathbf{a}}_{i,1} = \sum_{j=1,j\neq i}^{j=N} \dot{\mathbf{a}}_{ij,1} = \sum_{j=1,j\neq i}^{j=N} \left(m_j \frac{\mathbf{v}_{ij}^{\ 3}}{r_{ij}} - 3\alpha_{ij}\mathbf{a}_{ij,1} \right), \quad (2.15)$$

---

[1]The first, second and third time derivative of acceleration, $\dot{\mathbf{a}}$, $\ddot{\mathbf{a}}$, $\dddot{\mathbf{a}}$, are called *jerk*, *snap* and *crackle*, respectively.

$$\ddot{\mathbf{a}}_{i,1} = \sum_{j=1,j\neq i}^{j=N} \ddot{\mathbf{a}}_{ij,1} = \sum_{j=1,j\neq i}^{j=N} \left(m_j \frac{\mathbf{a}_{ij}^{\,3}}{r_{ij}} - 6\alpha_{ij}\dot{\mathbf{a}}_{ij,1} - 3\beta\mathbf{a}_{ij,1} \right), \tag{2.16}$$

with $\alpha = \mathbf{r}_{ij}\cdot\mathbf{v}_{ij}/r_{ij}^2$, $\beta = (v_{ij}^2 + \mathbf{r}_{ij}\cdot\mathbf{v}_{ij} + \alpha_{ij}^2\mathbf{r}_{ij}^2)/r_{ij}$ and $\mathbf{r}_{ij} = \mathbf{r}_{1,\mathrm{pred},i} - \mathbf{r}_{1,\mathrm{pred},j}$, where the subscripts i and j refer to the ith and the jth particle. Similar holds for $\mathbf{v}_{ij}$, $\mathbf{a}_{ij}$ and $\dot{\mathbf{a}}_{ij}$.

Finally, positions and velocity are corrected using the acceleration and its time derivatives evaluated above, resulting in :

$$\mathbf{v}_{i,\mathrm{corr}} = \mathbf{v}_{i,0} + \frac{\Delta t_{i,0}}{2}(\mathbf{a}_{i,1} + \mathbf{a}_{i,0}) - \frac{\Delta t_{i,0}^2}{10}(\dot{\mathbf{a}}_{i,1} + \dot{\mathbf{a}}_{i,0}) + \frac{\Delta t_{i,0}^3}{120}(\ddot{\mathbf{a}}_{i,1} + \ddot{\mathbf{a}}_{i,0}), \tag{2.17}$$

$$\mathbf{r}_{i,\mathrm{corr}} = \mathbf{r}_{i,0} + \frac{\Delta t_{i,0}}{2}(\mathbf{v}_{i,1} + \mathbf{v}_{i,0}) - \frac{\Delta t_{i,0}^2}{10}(\mathbf{a}_{i,1} + \mathbf{a}_{i,0}) + \frac{\Delta t_{i,0}^3}{120}(\dot{\mathbf{a}}_{i,1} + \dot{\mathbf{a}}_{i,0}). \tag{2.18}$$

Timestep

In general, given the wide range of timescales involved in N-body problems, spanning from days up to Gyrs, it is not convenient employing a fixed timestep for evolving an N-body system. Consequently, a more effective approach involves assigning an appropriate timestep to each particle based on its acceleration. During close encounters, a particle experiences an increase in acceleration, requiring a smaller timestep for accurate integration. Conversely, an isolated particle undergoes minimal changes in velocity over time, enabling the use of a longer timestep to avoid unnecessary computational overhead. The particle step in HiGPUs is computed using the *generalized Aarseth criterion* (Aarseth, 2003; Nitadori & Makino, 2008):

$$\Delta t_i = \eta \left(\frac{A^{(1)}}{A^{(p-2)}} \right)^{1/(p-3)}, \tag{2.19}$$

where p is the order of the integrator and $A^k = \sqrt{|\mathbf{a}^{(k-1)}||\mathbf{a}^{(k+1)}| + |\mathbf{a}^{(k)}|^2}$, where $A^{(k)}$ indicates the kth derivative of the acceleration.

2.2.3   GADGET-4

Direct summation of the gravitational force for each particle is computationally very expensive ($\mathcal{O}(N^2)$), thus limiting the number of particle that can be simulated. Different methods have been proposed for reducing the algorithmic complexity, the most commonly used being the *tree algorithm*. The underlying idea behind tree codes is that the gravitational potential of distant particles can be effectively approximated through a (low-order) multipole expansion centred

around their common centre of mass. Exploiting this concept, tree codes are designed to organise particles into a hierarchical tree-like structure.

In our investigation of the tidal stripping-driven mass loss of satellite galaxies in minor mergers presented in ch. 4, we validated our semi-analytical model against N-body simulations. In order to obtain a realistic evolution of the merger, not significantly affected by numerical effects, the total system to simulate is composed of $N \gtrsim 10^7$ particles. Direct-summation codes are too computationally expensive for such a number of particles. For this reason, the N-body simulations for this investigation have been carried out using GADGET-4. GADGET-4 is an openly accessible parallel cosmological N-body/SPH code, suitable for investigating a vast range of astrophysically significant phenomena, spanning from merging of galaxies to the large-scale structure formation in the Universe.

Out of the variety of methods with which GADGET-4 is equipped, in this section, we briefly describe only those that we have employed for our simulations.

Hierarchical tree structure

The idea under this method is the following: the entire space of the simulation is embedded in a 3-dimensional ideal cube, which is divided into eight equal cubes. If any of these cubes is populated by more than one particle, it is in turn divided in other identical eight sub-cubes. This procedure is recursively repeated until each cube contains only one particle. This hierarchical partition of the space is called *oct-tree*, a schematic representation of which is shown in fig. 2.1.

The gravitational potential generated by the particles in a cube can be expressed as:

$$\Phi(\mathbf{x}) = -G \sum_{j \in \text{cube}} m_j \, g(\mathbf{x}_j - \mathbf{x}), \tag{2.20}$$

where $g(\mathbf{x})$ is the Green's function, which for the Newtonian case is $g(\mathbf{x}) = 1/|\mathbf{x}|$. Denoting with $\mathbf{s}$ the center of mass of the particles in the cube, a Taylor expansion of the order p of $\Phi(\mathbf{x})$ around $\mathbf{s}$ is:

$$\Phi(\mathbf{x}) = -G \sum_{n=0}^{p} \frac{1}{n!} \mathbf{Q}_n \cdot \mathbf{D}_n(\mathbf{s} - \mathbf{x}) + \mathcal{O}(\theta^{p+1}), \tag{2.21}$$

where θ represent the angular extension under which the cube is seen. $\mathbf{Q}_n$ and $\mathbf{D}_n(\mathbf{x})$ are the cartesian multiple moments and the derivative tensor, defined as:

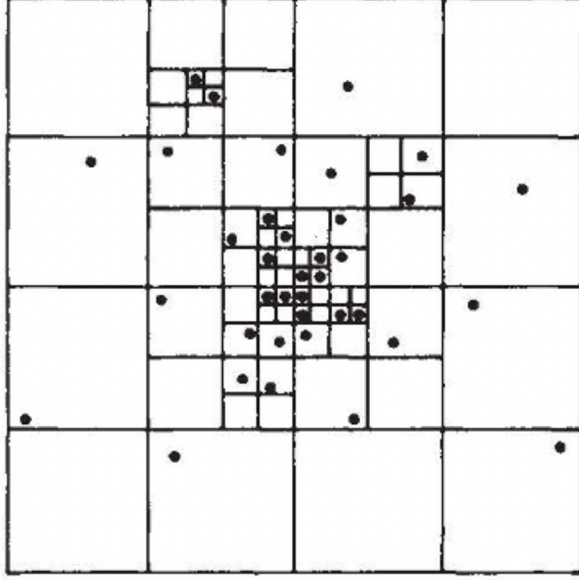$$\mathbf{Q}_n \equiv \sum_{j \in \text{cube}} m_j \, (\mathbf{s} - \mathbf{x})^{(n)}, \tag{2.22}$$

Figure 2.1: 2-dimensional representation of an oct-tree hierarchical space partition. Image
credits: Barnes & Hut (1986).

$$\mathbf{D}_n = \nabla^{(n)} g(\mathbf{x}). \tag{2.23}$$

where the superscript $^{(n)}$ refers to the nth outer product of the vector. Note
that since the expansion is performed around the cube center of mass, the
dipole moment always vanishes. Analogously, the acceleration exereted on a
particle at a location $\mathbf{x}$ can be expressed as:

$$\mathbf{a}(\mathbf{x}) = -\nabla\Phi(\mathbf{x}) = -G\sum_{n=0}^{p-1} \frac{1}{n!}\mathbf{Q}_n \cdot \mathbf{D}_{n+1}(\mathbf{s} - \mathbf{x}) + \mathcal{O}(\theta^p) \tag{2.24}$$

Once the hierarchical tree structure is set, the gravitational forces acting
on the particles are computed by performing a walk through the tree, starting
from the root. As the tree walk advances, each cube is sequentially examined.
In order to decide if the multiple expansion of the present cube is to be accepted
or not, different criteria can be used. In GADGET-4, the criterion is based
on the comparison between an approximation of the error of the expected force
with the magnitude of the total force:

$$\frac{M}{r^2}\left(\frac{l}{r}\right)^p < \alpha|\mathbf{a}|, \tag{2.25}$$

where $|\mathbf{a}|$ is the total acceleration, l is the length of the side of the cube, r is the
separation between the target point coordinates and the cube center of mass

location. If the criterion is not accepted, the multiple expansion is discarded, and smaller sub-cubes are considered.

In GADGET-4, the pure tree algorithm can be replaced by a hybrid method in which the tree algorithm is combined with the PM method. In short, the potential $\Phi(\mathbf{x})$ of the system of particles can be split in the Fourier space into two components: a long-range term Φ_k^{long} and Φ_k^{short}, $\Phi_k = \Phi_k^{\text{long}} + \Phi_k^{\text{short}}$. The short-range term is computed using the tree algorithm, which thus has to be applied on a small region in the proximity of the each target particle. The long term instead, is almost exact and not approximated as in the pure tree case.

Symplectic leapfrog method

Symplectic schemes are integration methods that preserve geometric structures by exactly solving the perturbed Hamiltonian. As a result, the numerical time evolution is described by a canonical map, ensuring the exact conservation of certain quantities, such as energy and angular momentum.

In a very general way, in typical N-body problems, the Hamiltonian is separable into two components:

$$H = H_{\text{kin}} + H_{\text{pot}}. \tag{2.26}$$

If this holds, for each of the parts the time-evolution operators can be computed exactly. Consequently, the *drift* and *kick* operator can be expressed as:

$$D_t(\Delta t) : \begin{cases} \mathbf{p}_i \mapsto \mathbf{p}_i \\ \mathbf{x}_i \mapsto \mathbf{x}_i + \frac{\mathbf{p}_i}{m_i} \int_t^{t+\Delta t} \frac{\mathrm{d}t}{a^2} \end{cases} \tag{2.27}$$

$$K_t(\Delta t) : \begin{cases} \mathbf{x}_i \mapsto \mathbf{x}_i \\ \mathbf{p}_i \mapsto \mathbf{p}_i + f_i \int_t^{t+\Delta t} \frac{\mathrm{d}t}{a} \end{cases} \tag{2.28}$$

where f_i is the force on the ith particle, and a is the cosmic scale factor.

The time integration scheme can be derived via operator splitting. Thus, it is possible to approximate the time evolution operator $U(\Delta t)$ for a time interval Δt by:

$$\tilde{U}(\Delta t) = K\left(\frac{\Delta t}{2}\right) D(\Delta t) K\left(\frac{\Delta t}{2}\right) \tag{2.29}$$

which corresponds to the kick-drift-kick leapfrog integrators.

Hierarchical timestepping

One of the main novelties of the present version of GADGET with respect to the previous ones consists in the possibility of adopting a hierarchical time

integration, based on a hierarchical and systematic decomposition of the dynamics of the Hamiltonian. In general, for system in which the Hamiltonian can be expressed in the form $H = H_1 + H_2$, the second-order split method used to integrate the Hamiltonian can be applied, which can be written for instance as:

$$E(H, \Delta t) \simeq E\left(H_1, \frac{\Delta t}{2}\right) \circ E(H_2, \Delta t) \circ E\left(H_1, \frac{\Delta t}{2}\right), \tag{2.30}$$

where $E(H, \tau)$ represents the system time evolution operator over a time τ and for a Hamiltionan H .

Consider a system of particles P described by an Hamiltonian that can be written as in 2.26. Assuming to be in a certain timestep Δt, the particles of the system can be split into a "slow" S and a "fast" F part: $P = F + S$. The particles in S are selected such that an integrator with the given timestep is sufficiently accurate. Conversely, F is composed of all the particles requiring to be evolved on shorter timesteps. After this partition of the particles, the Hamiltonian can be written as:

$$H = H_{\text{kin}}^S + H_{\text{pot}}^S + H_{\text{kin}}^F + H_{\text{pot}}^F + H_{\text{pot}}^{FS}, \tag{2.31}$$

where the term H_{pot}^{FS} includes all the potential terms involving mixed particle pairs.

At this point, the system can be evolved in time as:

$$E(H, \Delta t) \simeq E\left(H_{pot}^{FS}, \frac{\Delta t}{2}\right) \circ E\left(H_{pot}^F, \frac{\Delta t}{2}\right) \circ E(H^S, \Delta t)\circ$$
$$E\left(H_{pot}^F, \frac{\Delta t}{2}\right) \circ E\left(H_{pot}^{FS}, \frac{\Delta t}{2}\right). \tag{2.32}$$

Here, the particles in S are evolved over Δt, whereas for the particles in F the timestep size is set to be $\Delta t/2$. Note that this timestep can not be sufficient for an accurate time evolution of all the particles in F, thus requiring further iteration of the procedure. Finally, the term H_{pot}^{FS}, is assumed to be accurately evolved on the timestep $\Delta t/2$, since involving one of the slow particles.

Focusing on kick and drift operators for the time evolution, one can write:

$$E(H, \Delta t) \simeq K_F^S\left(\frac{\Delta t}{2}\right) K_S^F\left(\frac{\Delta t}{2}\right) E\left(H_F, \frac{\Delta t}{2}\right)$$
$$K_S^S\left(\frac{\Delta t}{2}\right) D(\Delta t) K_S^S\left(\frac{\Delta t}{2}\right) \tag{2.33}$$
$$E\left(H_F, \frac{\Delta t}{2}\right) K_S^F\left(\frac{\Delta t}{2}\right) K_F^S\left(\frac{\Delta t}{2}\right)$$

Since the term K_S^S commutes with $E(H_F)$, D_S can be interchanged with all the terms involving exclusively the fast components, and all the kick operators

can be interchanged, the above equation can be rewritten as:

$$
\begin{aligned}
E(H, \Delta t) \simeq & K_P^P\left(\frac{\Delta t}{2}\right) K_F^F\left(-\frac{\Delta t}{2}\right) E\left(H_F, \frac{\Delta t}{2}\right) D(\Delta t) \\
& E\left(H_F, \frac{\Delta t}{2}\right) K_F^F\left(-\frac{\Delta t}{2}\right) K_P^P\left(\frac{\Delta t}{2}\right)
\end{aligned}
\tag{2.34}
$$

The process is reiterated as follows. First the force on the whole system P is computed and is used to distinguish among fast and slow particles with a timestep criterion. For the particles belonging to F, the forces are recomputed only accounting for the fast particles. At this point the F systems becomes the "new" global system P' which in turn will be split in a slow and in a fast component, this time with the reference timestep size being $\Delta t/2$. This approach can then be recursively repeated until all the particles are evolved over an appropriate timestep.

Differences between GADGET-4 and previous versions

Besides the adoption of the hierarchical time stepping discussed above, the main novelties implemented in GADGET-4 with respect of previous version are:

- **Integer coordinates**: Floating-point numbers, commonly employed for particle coordinates, exhibit variable absolute positional accuracy in different regions of the simulation box. GADGET-4, to ensure uniform resolution, stores particle coordinates as integers. This approach also streamlines the construction of the oct-tree, as it allows for the employment of fast bit-shift operations to determine the sub-cube to which the particles belong. The relative distances between particles are first computed as integers and then are re-converted to floating-point values which can be used for subsequent calculations.

- **Parallelization**: New parallelization techniques have been implemented based on an improved domain decomposition, in which the domain is subdivided as though each MPI rank resided in an independent distributed memory node, which allow for a an extended scalability of GADGET-4.

Here we just referred to the new features directly employed in our simulations.

2.3   Galaxy models and initial conditions

2.3.1   Spherical models

In order to initialize numerical simulations involving galaxies, it is crucial that the model describing the system is in a state of dynamical equilibrium. The

simplest cases involve spherically symmetric isotropic models. In such systems, the gravitational potential and the mass density depend solely on the distance r from the system center, i.e. $\Phi(\mathbf{r}) = \Phi(r)$ and $\rho(\mathbf{r}) = \rho(r)$. The relation between density and potential is governed by the Poisson equation:

$$\nabla^2 \Phi(r) = 4\pi G \rho(r). \tag{2.35}$$

Moreover, from the density profile $\rho(r)$ it is possible to obtain the cumulative mass distribution by simply performing a volume integral:

$$M(r) = 4\pi \int_0^r \mathrm{d}r' \, r'^2 \rho(r'). \tag{2.36}$$

Spherical isotropic models have a phase space distribution which only depends on the energy $\mathcal{E}$, which is defined as $\mathcal{E} = -\frac{1}{2}v^2 + \Psi(r)$ where $\Psi = -\Phi + \Phi_0$ is the relative potential. Here, Φ_0 is a constant which for isolated and infinitely extended system is $\Phi_0 = 0$. The phase space distribution can be computed from the *Eddington formula* (Binney & Tremaine, 2008):

$$f(\mathcal{E}) = \frac{1}{\sqrt{8}\pi^2} \frac{\mathrm{d}}{\mathrm{d}\mathcal{E}} \int_0^{\mathcal{E}} \frac{\mathrm{d}\rho}{\mathrm{d}\Phi} \frac{\mathrm{d}\Phi}{\sqrt{\mathcal{E} - \Phi}}. \tag{2.37}$$

Below, I present the galactic models utilized in my numerical investigations.

2.3.2 Dehnen models

For the investigation into minor mergers detailed in ch. 4, I assume that the less massive satellite galaxy follows a Hernquist (Hernquist, 1990) density distribution, which belongs to the family of Dehnen models (Dehnen, 1993). Dehnen models exhibit spherically symmetric potentials and density profiles. Specifically, these models have a density distribution that behaves as $r^{-\gamma}$ at small radii, while at larger radii, it decreases as r^{-4}. The parameter γ can take values in the range $0 \leq \gamma < 3$. The model corresponding to $\gamma = 1$ is known as the Hernquist model. The density profile in Dehnen models is:

$$\rho(r) = \frac{(3 - \gamma)M}{4\pi} \frac{a}{r^{\gamma}(r + a)^{4-\gamma}}, \tag{2.38}$$

where M is the total mass of the system and a is its scale radius. Solving the Poisson equation allows for the evaluation of the gravitational potential associated with Dehnen density profiles, which takes the form:

$$\Phi(r) = \frac{GM}{a} \times \begin{cases} -\frac{1}{2-\gamma}\left[1 - \left(\frac{r}{r+a}\right)^{2-\gamma}\right] & \text{if } \gamma \neq 2 \\ \log\left(\frac{r}{r+a}\right) & \text{if } \gamma = 2, \end{cases} \tag{2.39}$$

where is assumed that $\Phi \to 0$ as $r \to \infty$.

Dehnen models with central super massive black hole

Just one year following the publication of the Dehnen models, Tremaine et al. (1994) proposed a characterization of the same family of models, also including a description of the model when hosting a central black hole. The addition of the black hole introduces another parameter μ in the model, which represents the SMBH mass as a fraction of the total mass of the system M.

This family of models is of particular interest for the first part of the present work (see ch. 3), since the host galaxy embedding the SMBHB is initially constructed using a Hernquist profile with a single central SMBH. The secondary SMBH is subsequently introduced in orbit around the primary one. The gravitational potential and density profile for this class of models are the following:

$$\Phi(r) = -\frac{G\mu M}{r} + \frac{GM}{a} \times \begin{cases} -\frac{1}{\eta-1}\left[1 - \left(\frac{r}{r+a}\right)^{\eta-1}\right] & \text{if } \eta \neq 1 \\ \log\left(\frac{r}{r+a}\right) & \text{if } \eta = 1, \end{cases} \tag{2.40}$$

$$\rho(r) = \frac{\eta}{4\pi} \frac{a}{r^{3-\eta}(r+a)^{1+\eta}}, \tag{2.41}$$

where the parameter η is the equivalent of γ in eqs 2.38 and 2.39, with $\eta = 3 - \gamma$ and $0 \leq \eta < 3$. Note that when $\mu = 0$, the above expressions for the potential and density equal eq. 2.39 and 2.38, respectively.

2.3.3 Generation of the initial conditions

To generate the initial conditions for the spherically symmetric models of galaxies we used the so-called *Monte-Carlo inverse transfor method* which, as suggested by the name, is based on the inversion of the *cumulative distribution function* (CDF) $F(X)$:

$$F(X) = \int_{-\infty}^{X} f(x)\mathrm{d}x, \tag{2.42}$$

where $f(x)$ is the probability distribution function (PDF). The CDF represents the probability that x takes on a value equal or lower than X and, by definition, is a monotonically increasing function of X. Moreover, since $f(x)$ is normalized such that $f(x) = \int_{-\infty}^{\infty} = 1$, $F(x)$ takes values on the range $[0, 1]$.

Given the PDF $f(x)$ of a random variable x and the associated CDF $F(X)$, it is possible to demonstrate that $Y = F(X)$ is itself a random variable, uniformly distributed in the range of values $[0, 1]$. Consequently, for any set of values Y uniformly distributed in $[0, 1]$, the univocally associated values x:

$$x = F^{-1}(Y) \tag{2.43}$$

are distributed following the original PDF.

In general, for spherically symmetric systems, the 3-dimensional PDF in polar coordinates can be expressed as the product of three 1-dimensional PDFs, each of which being a function of one of the three coordinates only:

$$f(r,\theta,\phi)r^2\mathrm{d}r\,\sin\theta\mathrm{d}\theta\mathrm{d}\phi = \mathrm{f_r}(r)\mathrm{d}r \cdot \mathrm{f}_\theta(\theta)\mathrm{d}\theta \cdot \mathrm{f}_\phi(\phi)\mathrm{d}\phi, \tag{2.44}$$

where:

$$\begin{aligned} f_r(r) &= f(r)r^2 \\ f_\theta(\theta) &= A\sin(\theta) \\ f_\phi &= B, \end{aligned} \tag{2.45}$$

here A and B are proper normalization constants.

In our framework, regarding the spatial distribution, the radial PDF $f(r)$ is:

$$f_r(r) = r^2 f(r) = 4\pi\rho(r)r^2, \tag{2.46}$$

where the term 4π comes from the normalization. Consequently, the associated CDF is nothing but the mass enclosed within r:

$$F_r = \int_0^r 4\pi\rho(r')r'^2\mathrm{d}r' \equiv \mathrm{M(r)}, \tag{2.47}$$

which holds for any spherical distribution. At this point, inverting $M(r)$, the particle radii can be assigned by simply extracting N random number Y from a uniform distribution within the range $[0,1]$, with N being the total number of particle of the galaxy, and for each computing $M^{-1}(Y)$.

An analogous procedure is adopter for generating the angular components of the particle positions and velocities, for which the CDF are:

$$F_\theta^{-1}(Y) = \arccos(1-2Y) \tag{2.48}$$

$$F_\phi^{-1}(Y) = 2\pi Y, \tag{2.49}$$

and for the amplitudes of the particle velocities. More specifically, in order to generate the particle velocities, the distribution function to be used is $f(\mathcal{E})$, which can be computed using the Eddington formula (see eq. 2.37). For a given $f(\mathcal{E})$ the associated CDF is:

$$F_v(r,\mathcal{E}) = \frac{1}{\rho(r)}\int_{-\frac{v^2}{2}+\Psi}^{\Psi} 4\pi\sqrt{2(\Psi-\mathcal{E})}f(\mathcal{E})\mathrm{d}\mathcal{E} \tag{2.50}$$

At this point the values of the velocities to be assigned to each particle has been computed as follows. We produce an equally spaced grid of energies

in range $[\Phi(ri), 0]$. The minimum energy corresponds to that of a stationary star, while $E_{\max} = 0$ since for $E > 0$ the star is unbound. We generate an array of $F_v(r_i, E)$ numerically integrating eq. 2.50 for each value of E in the grid with a fixed radius r_i. Then, we generate a random number Y uniformally distributed in the range $[0, F(r_i, \Phi(r_i))]$ and we interpolated it with the array of energies in the grid to obtain the energy E_i of the ith particle. Finally, we compute the particle velocity as: $v_i = \sqrt{2(\Phi(r_i) - E)}$.

2.3.4   Disc model

In my investigation on minor galaxy mergers, the primary galaxy was modelled as a multi-component system composed of a dark matter halo and a disc. As detailed in 4.1.3, in my simulations the halo is modelled as an analytical potential, thus the only "live" (i.e. modelled with collisionless particles) component of the primary galaxy is the disc. In this work, the disc component is modelled as an exponential disc, whose associated density profile is:

$$\rho_d(R, z) = \frac{M_d}{4\pi R_d^2 z_d} \mathrm{e}^{-\frac{R}{R_d}} \operatorname{sech}^2\left(\frac{z}{z_d}\right). \tag{2.51}$$

The initial condition in this case were performed using the publicly available code GALIC (Yurin & Springel, 2014). GALIC uses an iterative method to built N-body galactic models at equilibrium. A broad description of the procedure is described as follows. Consider a system of N collisionless particles, with initial positions $\mathbf{x}_i$, distributed according to a given $\rho_0(\mathbf{x})$, and initial velocities $\mathbf{v}_i$. The particle velocities has to be properly generated in order to obtain a stationary solution for the collisionless Boltzmann equation (see eq. 2.6).

Denoting as $\rho(\mathbf{x}, t, \mathbf{v}_1, ..., \mathbf{v}_N)$ the density field generated by the system while it evolves and with $\overline{\rho}(\mathbf{x}, \mathbf{v}_1, ..., \mathbf{v}_N) = \frac{1}{T} \lim_{T\to\infty} \int \rho(\mathbf{x}, t, \mathbf{v}_1, ..., \mathbf{v}_N) \, \mathrm{d}t$ the density response averaged in time for the initial velocity chosen, the best steady state of the system is determined by the minimum value of the difference between the initial density field and the time-averaged density. In other words, the initial particle velocities must be such that the function:

$$S(\mathbf{v}_1, ..., \mathbf{v}_N) = \int |\overline{\rho}(\mathbf{x}, \mathbf{v}_1, ..., \mathbf{v}_N) - \rho_0(\mathbf{x})| \, \mathrm{d}\mathbf{x} \tag{2.52}$$

is minimized.

However, in general, the velocity structure of an equilibrium model is not uniquely determined by its density structure, i.e. any given density structure can have more than one steady-state solution for the collisionless Boltzmann equation. Thus, additional constraints have to be imposed in order to reduce the space of possible solutions. For this reason, merit functions are introduced on the basis of symmetry assumptions concerning the velocity structure of the system. More specifically, three merit functions are defined Q_R, Q_z and Q_ϕ

which measure the deviation of the actual realized velocity dispersion (along the R, z, and ϕ directions respectively) from the expected values. The initial guess for the velocities is obtained randomly sampling from Gaussian distributions with appropriate local dispersions.

At this point the initial velocities $\mathbf{v}_i$ are recursively adjusted such that S, Q_R, Q_z and Q_ϕ are simultaneously minimized. It is possible to combine the quantities to be minimized in a single parameter S_{global}, defined as:

$$S_{\text{global}} = S + \chi(Q_R + Q_z + Q_\phi) \tag{2.53}$$

where χ is introduced to ensure that $\chi(Q_R + Q_z + Q_\phi)$ has the same unit as S. The minimization procedure is performed by considering one single particle randomly picked at a time, and then its velocity is optimized to reduce S_{global}. To achieve this, a new random velocity is assigned to the particle. The merit functions are re-evaluated for the new guessed particle velocity, and the new velocity value is only accepted if it improves the fit. Otherwise, the particle maintains the old velocity value, and the minimization process continues with a new particle. This procedure is repeated until the fit does not significantly improve further.

2.3.5 Semi analytical code - GALCODE

To investigate the tidal stripping of satellite galaxies in minor mergers, I employed GALCODE (Bonetti et al., 2021b), a semi-analytical code designed for orbit integration within generic galactic potentials. Specifically, I enhanced the functionality of GALCODE by integrating a novel semi-analytical model for evaluating the tidal radius of an extended massive perturber and tracking its mass evolution, as elaborated in ch. 4. The code leverages on the C++ implementation of the Bulirsch-Stoer (BS) method (Bulirsch & Stoer, 1966; Press et al., 2002) widely used to integrate ordinary differential equations (ODEs). The BS method is particularly suited for ODEs with widely varying timescales for different components of the system. The BS method progresses the solution of a system of ordinary differential equations through "macroscopic" steps. Such macroscopic steps are splitted in several sub-steps, each of which is integrated using the Modified Midpoint method. The result obtained with the sub-steps are finally extrapolated to infinitesimally small steps using the Richardson extrapolation technique, therefore ensuring a high accuracy.

GALCODE is designed to study the dynamics of massive perturbers (both point-like, as BHs, or extended, as satellite galaxies or stellar clusters) in their galactic potential. The semi-analytical framework features a comprehensive treatment of the dynamical friction specifically tailored to account for flattened and rotating systems (Bonetti et al., 2021b, 2020b) (see sec. 1.3.3). It is also equipped with a prescription for the interactions of massive perturbers with galactic substructures such as bars (Bortolas et al., 2022). The inexpensive computational cost makes the semi-analytical code a perfect tool when a large

exploration of the configuration space is needed. Furthermore, its modularity allows to implement new recipes to account for additional physics driving the evolution of massive perturbers in galaxies (see e.g. sec. 4.1.1).

3

Stellar hardening of massive black hole binaries: the impact of the host rotation

In this chapter, we investigate the impact of the rotation of the stellar bulge on the evolution of SMBHBs. The results presented in this chapter have been published in Varisco et al. (2021).

Indeed, apart from geometry (sphericity, axisymmetry, triaxiality), the net rotation has been recognized as a fundamental property of a stellar the bulge that can significantly influence the evolution of the hosted SMBHB. It is known that retrograde stars extract more efficiently angular momentum leading to eccentricity growth, whereas prograde stars promote circularization[1] (Sesana et al., 2011). Moreover, a SMBHB embedded in retrograde stellar systems secularly change its orbital plane to align its orbital angular momentum to that of the stars (Gualandris et al., 2012a). The importance of these findings stem from the fact that GW emission is much more efficient in eccentric binaries (Peters, 1964), thus significantly reducing SMBHB merger timescales. Moreover, LISA will have the capability of measuring the SMBHB eccentricity (Nishizawa et al., 2016), thus providing important information in the reconstruction of the dynamical processes driving the pairing and hardening phase.

The aforementioned early results have been subsequently more rigorously formalized in Rasskazov & Merritt (2017) and extensively investigated numerically in Holley-Bockelmann & Khan (2015); Mirza et al. (2017) and Khan et al. (2020). These latter works found that the center of mass (CoM) of a prograde binary within rotating systems does not stay put in the centre (except for the traditional Brownian motion that was already studied e.g. by Bortolas et al.

---

[1]Assuming a cartesian reference centered in the SMBHB center of mass, and the binary orbiting in the $x - y$ plane, a prograde (retrograde) star has the z component of its angular momentum aligned (antialigned) to the SMBHB angular momentum.

2016; Chatterjee et al. 2003; Merritt 2001a; Milosavljević & Merritt 2003a), but starts to move in approximately circular orbits around the CoM of the stellar system. Contextually, the binary is found to shrink more effectively. Since in those simulations the stellar system is also flattened by rotation, it is not clear whether those effects are purely induced by rotation, and their physical origin has not been investigated in depth.

We perform a detailed study of the wandering of the SMBHB CoM in a rotating stellar system. By means of controlled N-body experiments that keep the shape of the stellar distribution spherically symmetric while introducing net rotation, we isolate the role of rotation in the dynamical evolution of the SMBHB CoM and build a sound analytical model that describes the outcome of the simulations.

3.1   Simulations setup

In order study the effects of the system rotation on the evolution of SMBHBs, we chose to initialize the host system as a spherically symmetric distribution of stars. This allows us to isolate the effect of the system rotation from the impact of galaxy morphology, thus preventing the SMBHB evolution to be affected by the combined effect of both rotation and deviation from spherical symmetry. The host system is first initialized following an Hernquist (1990) density profile:

$$\rho(r) = \frac{M_{\text{tot}}}{2\pi} \frac{r_0}{r} \frac{1}{(r_0 + r)^3} \tag{3.1}$$

with total mass of stars M_{tot}, inner density slope $\gamma = 1$ and scale radius r_0. We set our model units (MU) such that $M_{\text{tot}} = G = r_0 = 1$, with G gravitational constant.

The stellar velocities are initialized at equilibrium in the potential well generated by the stellar distribution itself and by a primary SMBH of $M_\bullet = 0.005\,M_{\text{tot}}$, at rest in the origin of the system.

To introduce rotation into our model, we followed a procedure akin to that employed by Khan et al. (2020). Specifically, for co-rotating cases, we flipped the z-component of the angular momentum (L_z) for particles initially possessing negative L_z. This was realized by inverting the sign of all the velocity components of the selected stars. Analogously, for the counter-rotating case the particles with positive initial L_z were flipped to assume a negative L_z. It is important to note that the initial conditions employed do not correspond to any specific galaxy type. The spherically simmetric-rotating model used in our investigation is far from resembling early type slow rotators or classical dispersion-dominated elliptical galaxies due to its pronounced net rotation. Deviating from disk galaxies in terms of its structure, it bears some resemblance to rotating early-type galaxies. Indeed, in principle we could initialize a more realistic flattened system with a morphology directly linked to the degree of

Table 3.1: Parameters of the simulations presented in this work. The model names have been chosen as follows: the capital letter 'P' refers to prograde rotators while 'R' refers to the retrograde rotators, the number indicates number of particles of the simulation (1 for $N = 256$ k particles, 2 for $N = 512$ k particles and 3 for $N = 1$ M particles); finally, the letter 'e' refers to equal mass binaries ($q = 1$) while 'u' indicates unequal mass binaries ($q = 0.25$). See the text for more details.

Model	N	q	Rotation
P1e	256 k	1	co-rotating
P1u	256 k	0.25	co-rotating
P2e	512 k	1	co-rotating
P2u	512 k	0.25	co-rotating
P3e	1 M	1	co-rotating
P3u	1 M	0.25	co-rotating
R2e	512 k	1	counter-rotating
AP3e	1 M	1	co-rotating, anchored

rotation by sampling a distribution function of the form $f(E, L_z)$, as done, e.g., in Wang et al. (2014). We however decided to enforce the spherical symmetry of the stellar spatial distribution, to isolate the effect of rotation only, as clarified above.

A secondary SMBH is introduced in the system at an initial separation of r_0 with initial tangential velocity equal to 70% the circular velocity at r_0 and with null radial velocity. In all simulations, the angular momentum of the SMBH pair is initially perfectly aligned (or anti-aligned, for the counter-rotating case) with the system angular momentum.

We performed a suite of direct summation N-body simulations varying the mass resolution (i.e. the total number of particles N) and the binary mass ratio $q \leq 1$ ($q = 1, 0.25$). The simulations initializing parameters are summarized in Tab. 3.1. The labels of the runs are assigned so that the trailing capital letter refers to whether the (spherical) host system rotation is prograde ('P') or retrograde ('R') with respect to the SMBHB initial orbit; the subsequent number indicates the number of particles in the simulation (1 for $N = 256$ k, 2 for $N = 512$ k and 3 for $N = 1$ M); finally, the letter 'e' refers to equal mass SMBHs ($q = 1$) while 'u' indicates unequal mass SMBHs ($q = 0.25$). Note that the parameters of run P3e and P3u are similar to the runs $P_{1.00}$ and $P_{0.25}$ in Khan et al. (2020). In particular, the aforementioned runs present the same total number of particles ($N = 1$M) and the same SMBH mass ratios ($q = 1$ and $q = 0.25$, respectively). However, it is important to remember that the main difference of our work with respect to Khan et al. (2020) consists in the different geometry of the host system: while Khan et al. (2020) study the evolution of a SMBHB in a rotating flattened Dehnen profile (with $\gamma = 1$ and with a minor to major axis ratio of 0.8), we study how a SMBHB evolve in a spherical rotating stellar system. This is because we are interested in investigating the effect of the pure net system rotation on the SMBHB evolution and hardening, and the

introduction of a flattening would entangle the interpretation of our results.

We additionally performed a simulation with the same parameters as the P3e model (i.e. the highest resolution simulation with equal-mass binary co-rotating with the spherical stellar distribution) in which we forced the binary to stay anchored in the center of the system; we labelled this run as AP3e. More specifically, we took the snapshot at time $t = 30.375$ (shortly after the formation of the bound binary): at this time we restarted the run forcing the binary centre of mass to sit at the centre of the system. Every $\Delta t = 1.5625 \times 10^{-2}$ we recursively computed the centre of mass position and velocity of all particles (excluding the SMBHs) within $2.35 r_0$, which roughly coincides with the half mass radius of the system.[2] Then, we set the centre of mass position and velocity of the binary equal to the aforementioned one for the entire duration of the run. Note that the recentering significantly slowed down the integration: for this, AP3e was only evolved for $t \approx 45$ time units after the restart, while all other runs were evolved for at least 160 time units.

The initial conditions were evolved using the direct-summation N-body code HiGPUs, designed to run on GPU accelerators. HiGPUs features a very accurate, sixth order Hermite scheme with block time-steps (Capuzzo-Dolcetta et al., 2013). The computation of the timestep is performed by combining the fourth and sixth order Aarseth criterion (Aarseth, 2003; Nitadori & Makino, 2008), with the respective accuracy parameters equal to 0.01, 0.45. We set the softening parameter $\epsilon = 10^{-4}$ for star-star interactions, $\epsilon = 10^{-6}$ for SMBH-MBH interactions, while the softening for mixed stellar-MBH interactions is set equal to the geometric average of the two. For a typical run with 1M particles, evolved for ≈ 200 time units, the wall clock time needed is ≈ 110 hours, using one node equipped with two NVIDIA TeslaTM V100 GPUs, and four cpu cores.

3.2   Results

The evolution of the SMBHB with its host in the P1e model is illustrated in Fig. 3.1, where the color code indicates the projected density on the SMBHB orbital plane.

Since the two black holes are generated at an inital relatively small separation, the pairing phase ($t \lesssim 12$), during which the binary shrinking is dominated by dynamical friction, is short and soon ends with the binary formation.

Figure 3.2 displays the relative separation of the SMBHs as a function of time. It is evident that for equal-mass binaries ($q = 1$), the binary formation time $t_{\rm bf}$ (dashed vertical line in the figure) is shorter compared to the corresponding case with a smaller mass ratio, $q = 1/4$. This result is easily explained by dynamical friction considerations: the more massive the perturbing

---

[2]The recentering is performed 5 times per step, with the binary centre of mass as the initial guess.
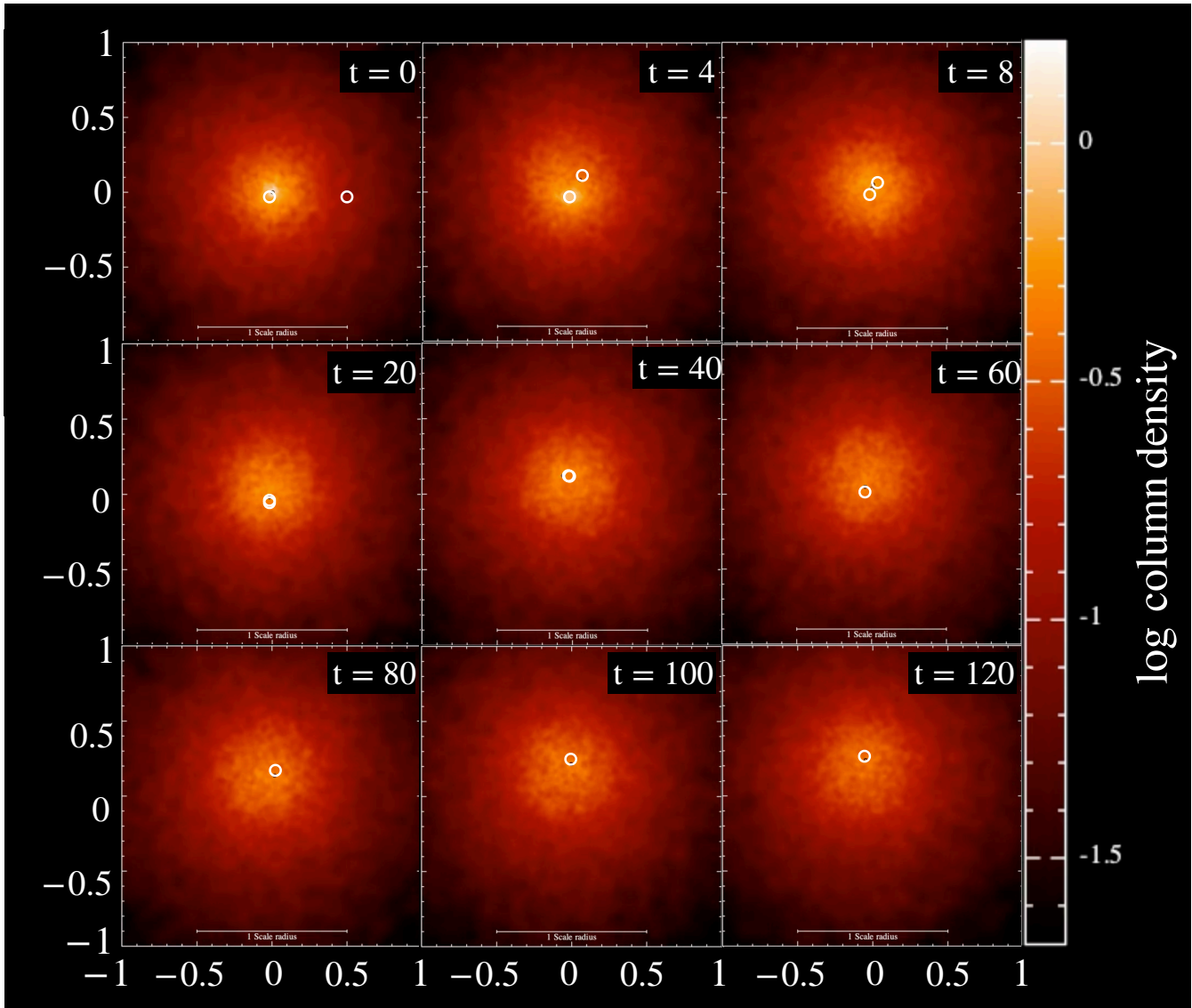
Figure 3.1: Evolution of the stellar density surface for the model P1e at different times. The time of the snapshot is reported on the top right of each panel. The two white empty circles represents the position of the two massive black holes. The color scaling is the same for all the panels.
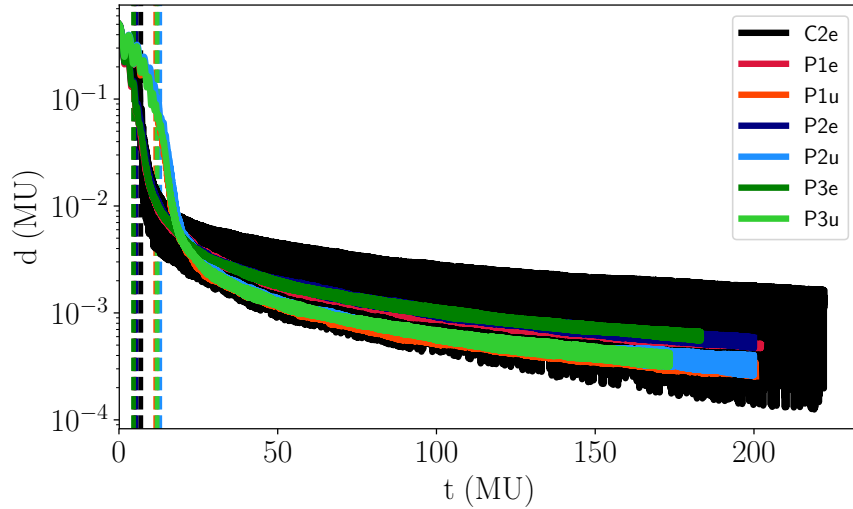
Figure 3.2: Evolution of the relative SMBH distance in time. The dashed vertical lines show the binary formation time for each simulation.

object, the more efficient the dynamical friction brake, leading to faster initial binary shrinking. Another trend with the mass ratio becomes evident: lower mass-ratio binaries reach smaller relative separations at later times.

Figure 3.2 illustrates two phases of the binary evolution described in sec. 1.4.1. Once the binary has formed, the SMBHB undergoes a phase of rapid shrinking due to the combined effects of dynamical friction and slingshot ejection of stars. This phase is evident in figure 3.2 as the rapid decrease in relative distance soon after binary formation. Subsequently, when the binary separation becomes comparable to the binary influence radius, dynamical friction becomes inefficient, and further shrinking of the binary slows down, proceeding via the slingshot ejection mechanism. This is reflected in the figure by the decrease in the slope of the relative distance.

3.2.1   Evolution of the orbital parameters

Fig. 3.3 shows the evolution of the SMBHB properties as a function of time, and specifically the binary eccentricity e and the inverse of its semi-major axis, $1/a$. The dashed vertical lines indicate the binary formation time $t_{\rm bf}$, chosen as the instant at which a bound Keplerian binary forms. Note that the eccentricity and semimajor axis are computed as the standard Keplerian parameters from the binary formation time. Prior to that, these quantities are evaluated as:

$$
\begin{aligned}
a_{\rm unbound} &= \frac{r_a + r_p}{2} \\
e_{\rm unbound} &= \frac{r_a - r_p}{r_a + r_p}
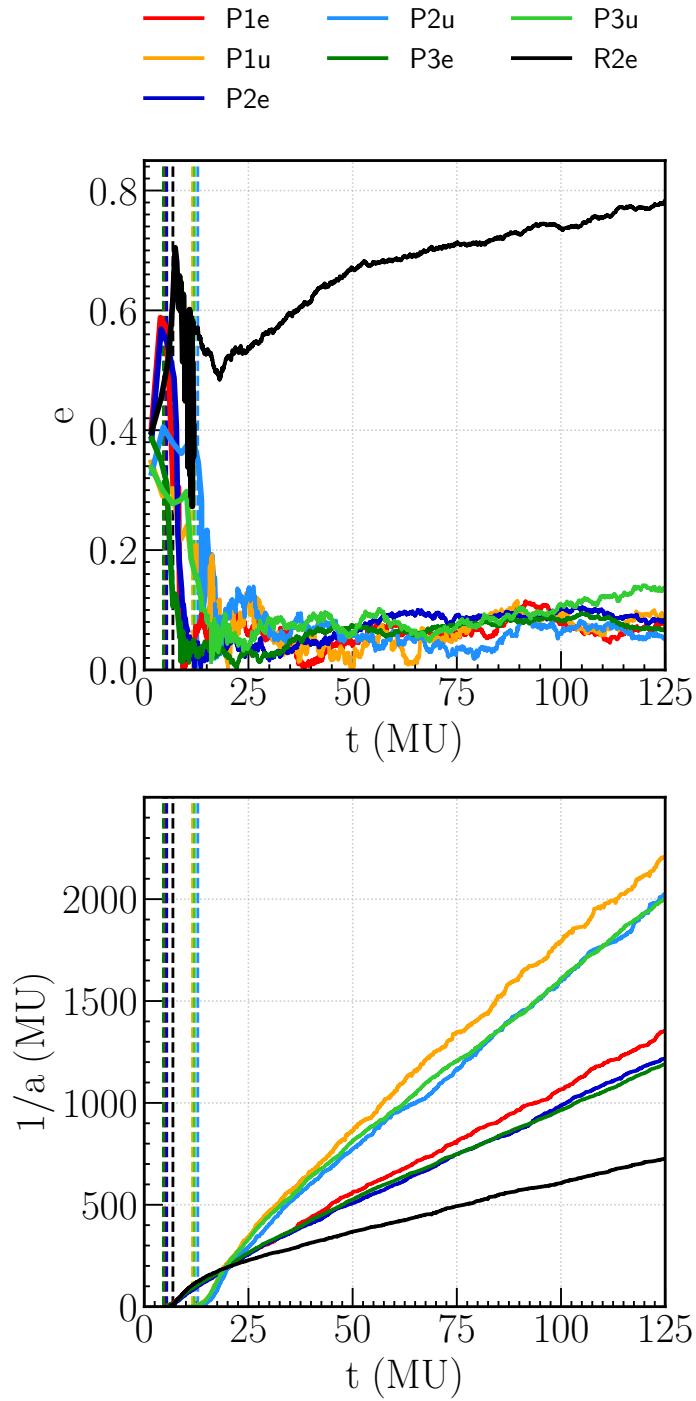\end{aligned}
\tag{3.2}
$$

Figure 3.3: Time evolution of eccentricity (upper panel) and inverse semi-major axis (bottom panel) for each simulation. Note that prior to the binary formation time (indicated with a vertical dashed line) the binary orbital parameters are computed via Eq. 3.2, while the standard Keplerian parameters are shown after the binary formation time.

Table 3.2: For each run, the binary CoM radius is averaged over the time interval from $t = 75$, where all models have settled around a nearly constant value, to $t = 175$. The binary influence radius is computed using the definition in Eq. 3.3 and averaged over the same time interval of R_b, while the Brownian radius is computed via Eq. 3.5, as better detailed in the text.

Model	Binary CoM final radius (MU)	Binary influence radius (MU)	Binary Brownian radius (MU)
P1e	0.047	0.22	0.011
P1u	0.020	0.16	0.014
P2e	0.058	0.22	0.008
P2u	0.012	0.16	0.010
P3e	0.065	0.22	0.006
P3u	0.026	0.15	0.007
R2e	0.010	0.20	0.008

where r_p and r_a respectively represent the pericentre and apocentre separations, computed once for each complete radial oscillation.

Fig. 3.3 shows the different stages characterizing the SMBHs orbital evolution. Initially, the SMBHs mutual separation is reduced via dynamical friction (Chandrasekhar, 1943b). In our models, the two SMBHs are initially placed at a relatively small separation, thus this phase is very short, and it ends roughly with the formation of a bound binary. When the binary reaches a separation comparable to the SMBHB influence radius, defined as the radius of a sphere containing twice the SMBHB mass in stars:

$$M_*(r < r_{\text{inf}}) = 2M_b \tag{3.3}$$

three body scatterings with stars start to efficiently extract energy and angular momentum from the binary, adding up to the effect of dynamical friction and excavating a core in the stellar density profile (e.g. Milosavljević & Merritt, 2003a; Sesana et al., 2008); the scouring of the density profile in time is shown in Fig. 3.4 for model P3e. The SMBHB eventually reaches the hard binary separation a_h, i.e. the separation at which the binary binding energy exceeds the kinetic energy of the field stars:

$$a_h = \frac{GM_2}{4\sigma_*^2} \tag{3.4}$$

where M_2 is the mass of the secondary SMBH and σ_* is the velocity dispersion of field stars. At this stage, the binary hardening occurs by stellar interactions only, and the binary hardens at a slower pace, until it reaches the separation at which GWs start to dominate its evolution.[3]

Fig. 3.3 shows that the dynamical friction (DF) driven inspiral is more efficient for equal mass binaries, as the intruding SMBH has a larger mass.

---

[3]Note that the integrator implements a purely Newtonian approach and the GW phase cannot be followed in the current setup.

After the binary formation, the binary tends to circularize in all the prograde models. In the retrograde rotators instead the binary eccentricity follows a significantly different trend: after a short phase of slow decrease, e starts rising and it reaches $e \simeq 0.8$ by the end of the run. This result is aligned with what found in previous studies addressing the binary eccentricity evolution in rotationally supported systems (e.g. Gualandris et al., 2012a) in which the perturber interacts with stars with a net tangential (prograde or retrograde) motion. The evolution of the inverse semi-major axis, showed in the lower panel of Fig. 3.3, is an important measure of the binary energy change as a function of time. All the simulated models follow a similar qualitative evolution: once the binary forms, the inverse semi-major axis undergoes a short phase of fast increase after which it increases almost linearly with time. As expected, the models with lower mass-ratio show a faster binary shrinking compared to the corresponding equal mass case (Sesana et al., 2006).

In all runs, the slight dependence of the shrinking efficiency on the total number of particles may be at least partially ascribed to two-body relaxation, which refills the binary loss cone more efficiently for the less resolved runs. We would like to stress once more that, in our runs, the idealized assumption of spherical symmetry in the mass distribution is made in order to isolate the impact of the system rotation on the binary shrinking rate; deviations from sphericity would tangle the interpretation of our results, as global gravitational torques induced by a non-spherical morphology would non-trivially impact the evolution of the binary hardening; the impact of rotation and axisymmetry combined have been investigated in Holley-Bockelmann & Khan (2015); Khan et al. (2020); Mirza et al. (2017). It is important to note that the counter-rotating case shows a significantly lower binary hardening compared to all the co-rotating models. This aspect is better dissected in the sections below.

3.2.2   Center of mass evolution

In line with previous literature on the topic (Holley-Bockelmann & Khan, 2015; Khan et al., 2020; Mirza et al., 2017), we found that the binary CoM in the prograde runs starts moving on a nearly circular orbit about the centre of the system shortly after the binary formation time. In this section, we investigate such behaviour in detail. In order to characterize the binary CoM motion we first need to define a reference centre of the host stellar system. To define the system centre we proceed as follows. As a first guess we set the system CoM to coincide with the binary CoM. We proceed computing the CoM of the stars contained within a radius of $2.35\,r_0$ and then re-centering the whole system at that position. The iteration is repeated five times per snapshot.

All our results are presented in a reference frame centered in the above defined position.[4]

---

[4]Note that the strategy described here to find the centre of the stellar distribution is the same used for anchoring the binary at runtime for run AP3e. In addition, we explored
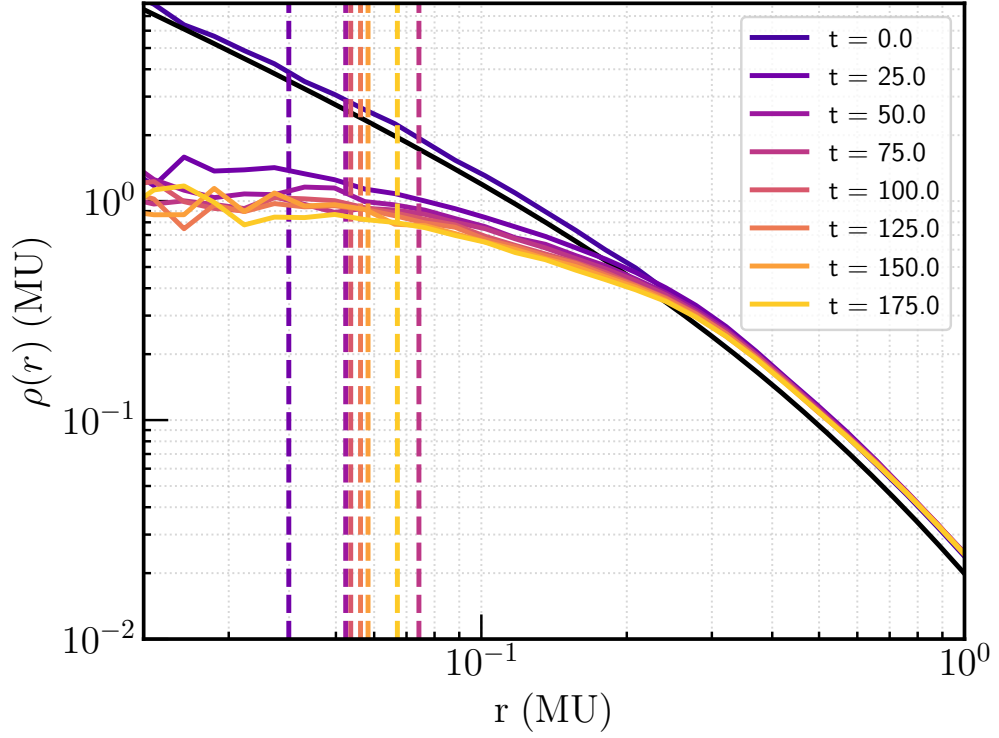
Figure 3.4: Evolution of the stellar density profile at different simulated times for model
P3e. Density profiles are drawn at six different times: from the dark purple
line at $t = 0$ to the yellow line at $t = 150$. Each profile was obtained averaging
over five subsequent time-steps. The black solid line is the initialized theoretical
Hernquist profile. The vertical dashed lines, with the same color code of the
density profiles, indicate the binary CoM radius at the corresponding time. The
position of the binary CoM is not shown for $t = 0$ since a bound binary has not
formed yet. It is evident that, even though at larger radii all the profiles are
consistent with the model, the central density is progressively reduced with time
as an effect of slingshot interactions; the binary CoM always remains within the
carved, almost constant density inner region.

Fig. 3.5 shows the 3-dimensional trajectory of the SMBHB CoM for all the simulated models. The top panel in Fig. 3.6 reports the temporal evolution of the distance between the SMBHB CoM and the host centre (R_b) after the binary formation time. For co-rotating models, soon after the binary formation time t_{bf}, the SMBHB CoM starts orbiting the host centre with a rapidly increasing R_b. After just few tens of time units the CoM settles on a nearly stable orbit. In particular, equal mass binaries show a faster rise of the CoM radius compared to the lower mass ratio cases. Moreover, the higher the binary mass ratio, the larger the final orbital radius: the two differ by nearly a factor 2. The retrograde run does not show the same behaviour, and the binary CoM remains very close to the centre, only experiencing the traditional Brownian wandering (as detailed below). Table 3.2 reports the mean value of the final CoM radius for each model, computed averaging R_b over the time interval from $t = 75$, where all models have settled around a nearly constant value, to $t = 175$, along with the binary influence radius, R_{inf}, averaged over the same time interval. Bottom panels of Fig 3.6 show the time evolution of the binary CoM orbit in the x and y-coordinate (left and right panel, respectively) for the run 3Pe, thus pointing out the quasi-periodicity of the binary CoM orbit. In co-rotating runs hosting equal-mass binaries the influence radius is $R_{inf} = 0.22$ while for co-rotating unequal-mass binaries is $R_{inf} \simeq 0.16$. This difference is, at least partially, due to the different total mass of the SMBHB ($M_b = 0.01$ if $q = 1$, $M_b = 0.00625$ for $q = 1/4$). The binary CoM oscillation in the prograde runs is much larger than the binary separation (see e.g. the values of $1/a$ in Fig. 3.3), but smaller than the SMBHB influence radius by a factor $3 - 5$ for the equal mass and by a factor $6 - 13$ for the unequal mass cases.

Note that the binary CoM oscillation found in the prograde runs is different than the traditional SMBHB Brownian motion (see e.g. Bortolas et al. 2016; Chatterjee et al. 2003; Merritt 2001a; Milosavljević & Merritt 2003a). The latter is caused by the fact that slingshot ejections of stars with isotropic velocities w.r.t. the binary CoM induce a recoil in the binary CoM in random directions. The associated displacement is contrasted by the effect of dynamical friction onto the binary as a whole: These two phenomena balance each other and result in a small and non-coherent wandering of the binary CoM, which however does not exhibit, on average, any net angular momentum. The typical scale of the traditional Brownian wandering is smaller than the oscillation radius we find in prograde runs. In fact, the Brownian wandering radius scales as

$$r_{Brown} \propto (m_\star / M_b)^{1/2} \tag{3.5}$$

where $m_\star$ is the typical particle mass in the run and M_b is the binary total

---

another possibility for computing the centre of the system: we recursively computed the CoM of particles in a shrinking sphere whose maximum (minimum) radius was set to $100r_0$ ($1.5r_0$); the radius was halved at each iteration. We found a very good match between the two described centering strategies, with mismatches much smaller that the wandering radius R_b.

mass (Merritt, 2001a). Bortolas et al. (2016) report a value of $r_{\mathrm{Brown}} \approx 0.008$ for $m_{\star}/M_{\mathrm{b}} \approx 2 \times 10^{-4}$ in a system whose initializing properties are analogue to the ones considered in the present work (i.e. an initial Hernquist profile with unitary scale radius and total mass). By rescaling this value via Eq. 3.5 we can infer the magnitude of the Brownian wandering in our runs: the computed values are shown in the left-hand column of Tab. 3.2, and as error-bars in the upper-right panel of Fig. 3.6. The Brownian radius is significantly smaller than the oscillation radius for prograde runs with the best adopted resolution, especially for the equal mass cases. The binary CoM displacement found in the retrograde case is instead compatible with being caused by the traditional Brownian motion. It is reasonable to interpret the trends shown in the upper panel of Fig. 3.6 for prograde runs as the combination of the net rotation of the binary CoM, induced by the system rotation, and the traditional Brownian motion, that is likely responsible for at least part of the noise in the plotted curves. This idea is supported by the fact that the runs featuring a larger N are less noisy than the lower resolution ones, as expected from Eq. 3.5; part of the oscillations in the trend of the CoM radius (especially at early times, and in the low-resolution cases) is due to the fact that the CoM orbital motion does not span a perfectly circular orbit, but exhibits some residual eccentricity. It is also important to notice that the final radius at which the SMBHB CoM settles does not depend on the number of particles adopted in the run, supporting the fact that the CoM oscillations are not an effect of limited resolution (which instead plays a significant role in the traditional Brownian motion, Eq. 3.5).

3.2.3 Effect of the SMBHB center of mass motion on binary hardening

In this section we explore the impact of the CoM oscillation on the SMBHB hardening rate. This aspect is relevant as the SMBHB CoM wandering allows it to explore a region of space where it can interact with stars which otherwise would not be able to approach the binary. In this way, the binary loss cone can be considered to be always full: the CoM oscillation may thus enhance the binary shrinking efficiency even for spherical systems in the collisionless limit.

To quantify the efficiency at which the binary shrinks, it is customary to define the binary hardening rate s as the time derivative of the inverse semi-major axis:

$$s = \frac{\mathrm{d}}{\mathrm{d}t}\left(\frac{1}{a}\right). \tag{3.6}$$

This quantity is a measure of the binary energy loss as a function of time. Fig 3.7 shows the time evolution of the hardening rate for the presented runs, and it is computed by fitting the slope of the inverse semi-major axis over short time intervals ($\Delta t = 1.25$). The hardening rate evolution for the prograde runs does not show a substantial dependence on the number of particles for

each fixed mass ratio, and it stabilizes to $s \approx 10$ ($s \approx 15$) for equal (unequal) mass binaries. On the other hand, the retrograde run (R2e) features a significantly smaller hardening rate (nearly a factor 2 smaller) compared to the prograde equal mass runs. The fact that the retrograde run does not feature any oscillation about the centre apart from the traditional Brownian wandering, contrarily to the prograde cases, is an indication of the fact that the binary coherent oscillations ensure a more efficient loss cone refilling.

In order to have a deeper insight on the role of the binary oscillation on the loss-cone refilling, we performed a run forcing the co-rotating binary in the P3e model to stay anchored to the system's center (A3Pe model), as detailed in Sec. 3.1. In Fig. 3.8 the hardening rate of the anchored binary in AP3e is compared to that of the free co-rotating binary in the same resolution run, P3e, and of the counter rotating run, R2e. What emerges is that once the binary CoM orbital motion is inhibited, the binary hardening rate is nearly equal to that of the counter-rotating case. This is a very strong indication of the fact that the loss cone refilling within rotating systems hosting a prograde binary is induced by the SMBHB CoM oscillation.

3.2.4   CoM evolution for a single SMBH

In order to better understand the nature of the SMBHB wandering, and especially if slingshot interactions with passing stars are the responsible for the non-Brownian oscillation of prograde binaries, we perform an additional run in which we manually merge the SMBHB in model P2e into a single SMBH at time $t = 70$. From this moment on, we track the displacement of the single SMBH from the centre of the stellar distribution as a function of time. Fig. 3.9 shows that, after the forced binary coalescence the SMBH gradually sinks back towards the center of the stellar distribution, and it stabilizes its oscillation radius to ≈ 0.01 by $t \approx 100$; the final radius nearly coincides with its expected Brownian wandering radius (see Eq. 3.5 and Tab. 3.2).[5] This behavior is a strong indication of the fact that slingshot interactions with the binary sustain its CoM displacement and oscillation about the centre; once the binary has merged, the single SMBH can sink back near the origin of the distribution as a result of dynamical friction. This proves that single SMBHs only experience the traditional Brownian wandering, regardless of the system rotation.

3.3   Modelling of the CoM evolution

To explain the behavior of the SMBHB CoM in spherical rotating models, it is important to consider that, in the prograde scenario, virtually all stars approach the binary with a z component of their angular momentum aligned

---

[5]Note that the Brownian wandering radius of a single SMBH is expected to be nearly equal to the one of a binary with the same mass (Eq. 3.5, Merritt 2001a).
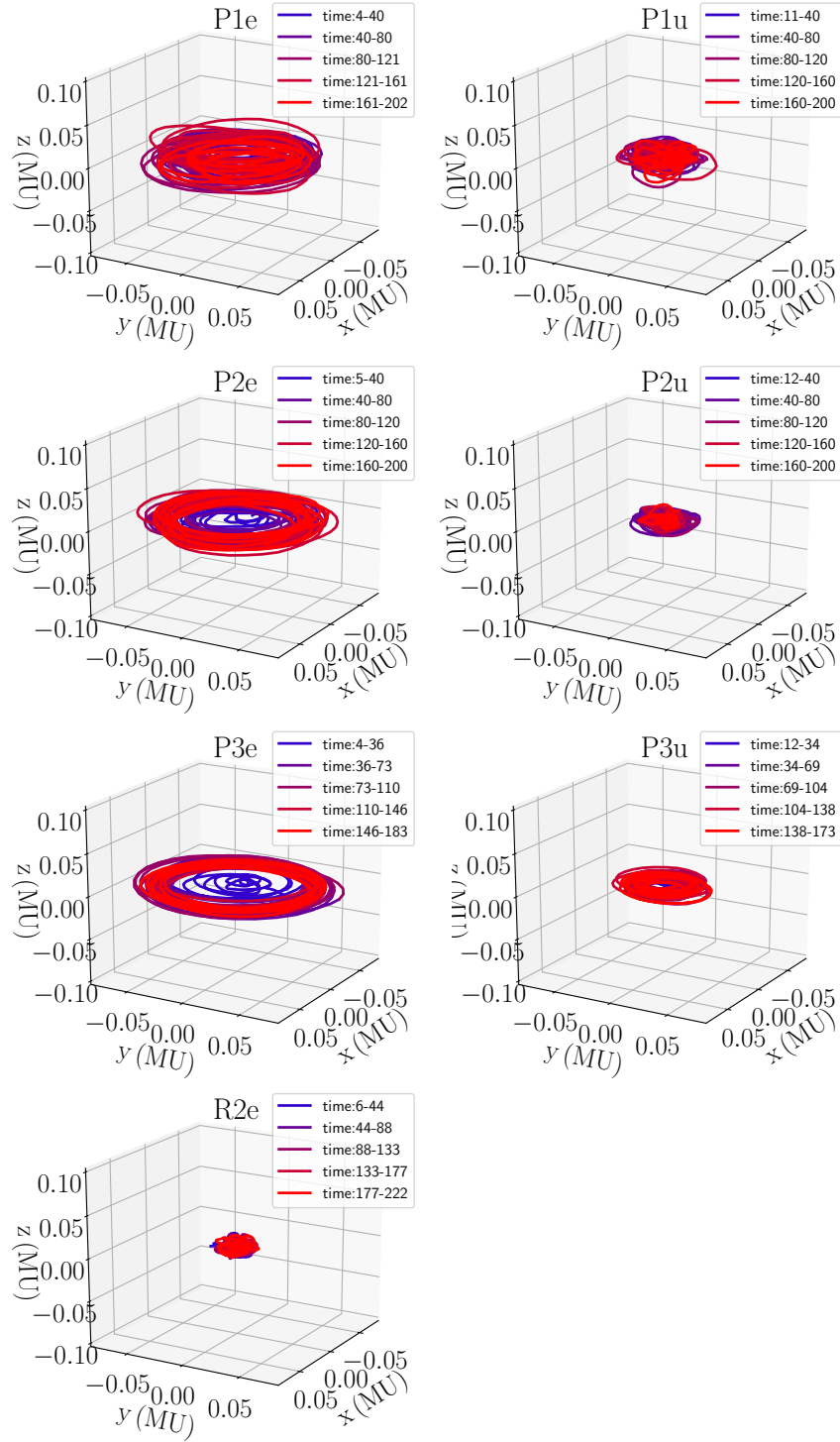
Figure 3.5: The figures show the three dimensional evolution of the SMBHB CoM trajectory for each of the runs presented in the current study. In each panel, the color code maps different time intervals in the orbital evolution, as shown in the legend. The initial time corresponds to the instant at which a bound Keplerian binary forms.
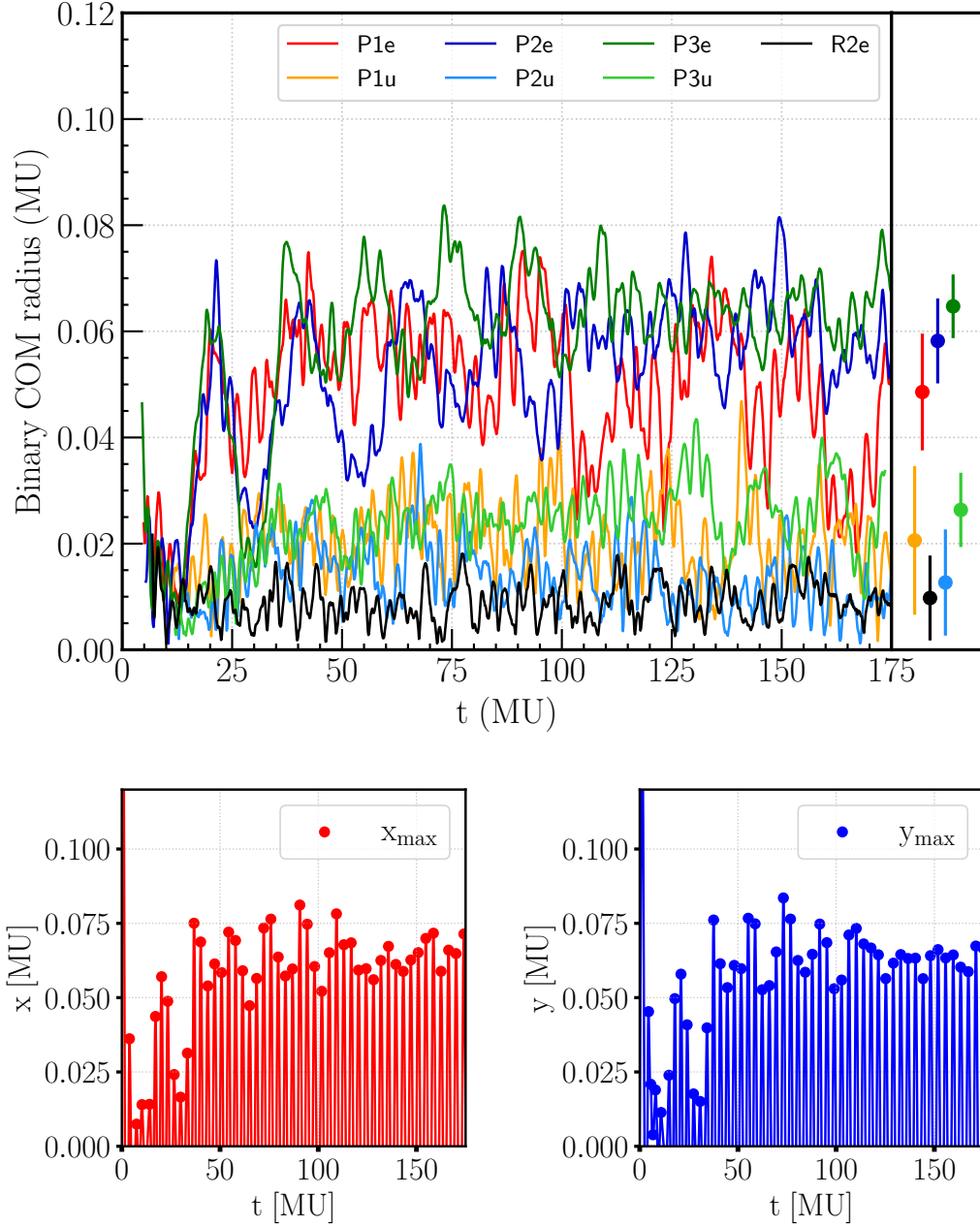
Figure 3.6: *Upper panel*: on the left is shown time evolution of the SMBHB CoM radius R_b for the different runs presented in the paper; on the right, the dots indicate, for each run, the value of the binary CoM radius averaged between $t = 75$ and $t = 175$, while the error bars show the amplitude of the Brownian wandering radius (see Tab. 3.2). *Bottom panels*: on the left is shown the time evolution of the binary CoM orbit in the x-coordinate for run P3e, the dots indicating the local maxima. The analogus is shown on the right panel for the orbit in the y-coordinate.
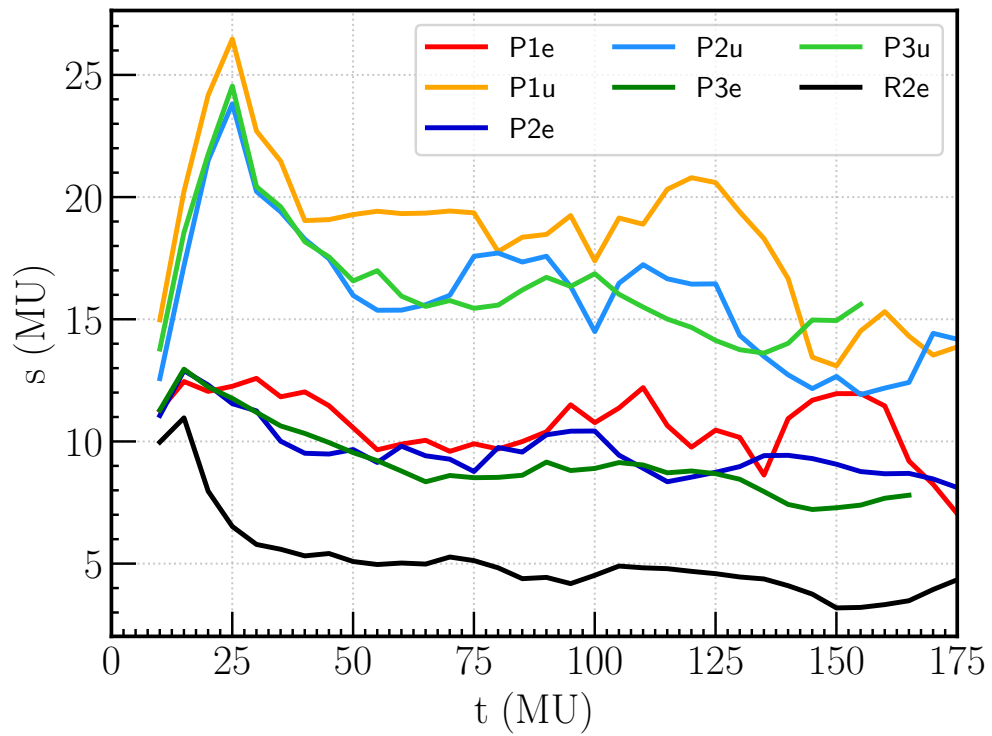
Figure 3.7: Time evolution of the hardening rates (Eq. 3.6) for the different runs presented in the paper.

Figure 3.8: Time evolution of the hardening rates (Eq. 3.6) for the prograde equal mass
run P3e, the retrograde equal mass run R2e and the model AP3e, in which the
CoM of the equal mass, prograde binary is fixed at the centre of the stellar
distribution. If the binary is anchored in the centre, its hardening rate gets very
similar to that of the retrograde run.

Figure 3.9: Displacement from the centre of the stellar distribution of a single SMBH initial-ized by manually merging the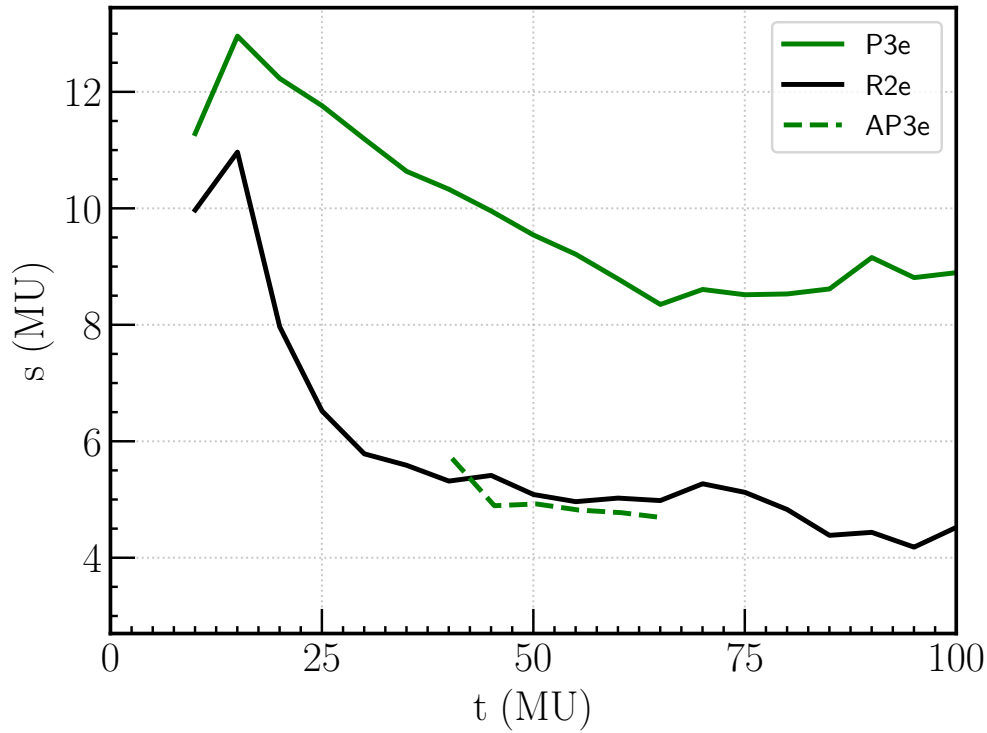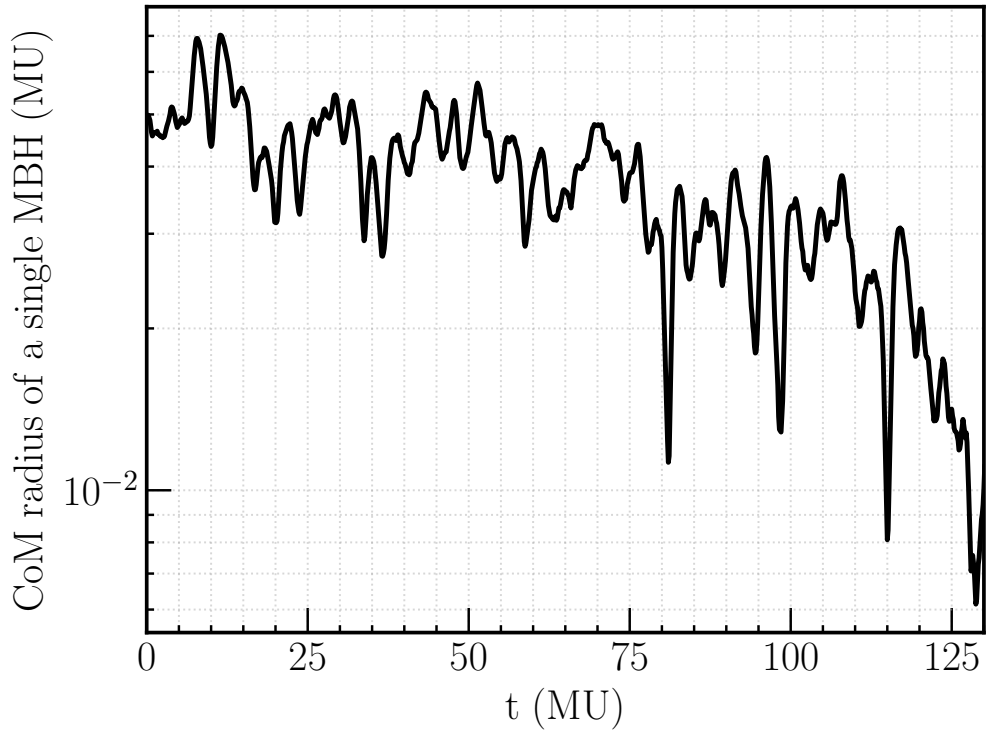 binary in run P2e. Time $t = 0$ corresponds to the instant at which the SMBHs in the progenitor binary are merged. The SMBH gradually inspirals towards the centre of the system in response to dynamical friction, and it does no longer exhibit coherent oscillations about the system centre.
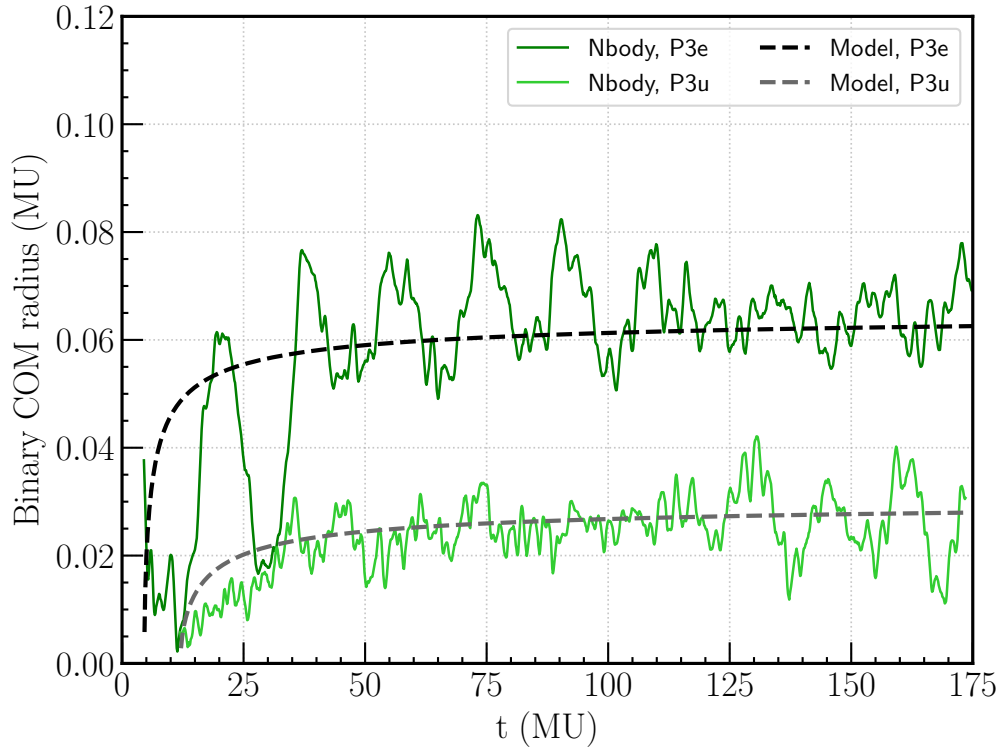
Figure 3.10: Time evolution of the binary CoM displacement from the centre of the system, R_b, as obtained from the simulations (solid lines) and from our theoretical modelling (Eq. 3.11). For model P3e we solved Eq. (3.11) assuming $\rho = 0.8$, $\sigma = 0.7$, $a_0 = 0.05$, $s = 10$ and we initialize $R_b = 0$ at $t = 7.5$; for model P3u we set $\rho = 2$, $\sigma = 0.75$ $a_0 = 0.01$, $s = 15$ and we initialize $R_b = 0$ at $t = 12$. These are characteristic values we extracted from the simulation. The most uncertaity is associated to the choice of a_0, as better detailed in the text and in footnote 8.

with the binary angular momentum and typically larger than that of the binary, at least for the stages just after the binary formation, during which the binary external angular momentum experiences a significant growth. In addition, in the prograde runs, the binary eccentricity remains always very close to 0, or in other words, the SMBHB has nearly the maximum angular momentum allowed for that given semi-major axis. At each prograde interaction, each star is thus likely to enhance the binary angular momentum. This enhancement can result in (i) an enlargement of the binary semi-major axis, but this almost never happens, as the interactions are typically found to shrink the binary (Fig. 3.3); (ii) a reduction of the binary eccentricity, which is however already near its minimum, and it cannot decrease further; (iii) an enhancement of the external angular momentum of the binary, which is then the only viable option. In this situation, the time variation of the external binary angular momentum[6] $L_{\text{ext}} = M_b R_b v_b$, with R_b, v_b radius and velocity of the binary CoM, should be equal to the rate at which the binary encounters stars times the typical angular momentum gained by the binary for each encounter. The stellar encounter rate can be written as $dN/dt = 2\pi G M_b a n_\star / \sigma$, where a is the binary semimajor axis, while $n_\star$ and σ respectively represent the stellar number density and velocity dispersion about the binary; the typical angular momentum exchange per stellar interaction is $\Delta L_\star \approx (m_\star / M_b) L_{\text{int}}$, where $L_{\text{int}} = \mu \sqrt{GM_b a}$ is its internal angular momentum (in the – verified – assumption of a circular binary), and μ is the reduced mass of the binary. It follows that

$$\frac{dL_{\text{ext}}}{dt} = \frac{2\pi G \rho}{\sigma} \mu \sqrt{GM_b a^3}, \tag{3.7}$$

where $\rho = m_\star n_\star$. The CoM velocity v_b is the circular velocity at the radius of the binary CoM; since the density profile remains nearly flat in the central region after the initial scouring, we can write

$$v_b = \sqrt{\frac{4\pi G \rho}{3}} R_b, \tag{3.8}$$

i.e. the expected circular velocity at R_b; we checked the validity of this expression, and we found a very good match in our runs. On the right-hand side of Eq. 3.7, a exhibits the strongest dependence on time (see e.g. $1/a$ in Fig. 3.3): from Eq. 3.6 we can write

$$a(t) = \frac{a_0}{1 + a_0 s t}, \tag{3.9}$$

with $a_0 = a(t = 0)$.[7] In this model we neglect the much milder time dependence of σ (whose value within a radius of $\approx R_b$ only varies by nearly 10 per cent

---

[6]Here we assume that the external binary angular momentum is aligned with the system rotation, as we find in our runs, and that the binary CoM orbital motion remains perfectly circular.

[7]Note that, in principle, this expression is valid only when the binary is hard, but for simplicity we assume it to be valid from the moment R_b starts increasing; this is an approximation, but it is supported by the relatively limited variation of $s(t)$ in Fig. 3.7.

in our models) and ρ (which nearly halves its value at $\approx R_b$ by the end of the integrations). Combining Equations (3.7, 3.8, 3.9) we obtain

$$\frac{d}{dt}R_b^2 = \sqrt{\frac{3\pi G^2 \rho}{\sigma^2}\frac{\mu^2}{M_b}a^3(t)}, \tag{3.10}$$

whose solution reads, setting $R_b^2 = 0$ at $t = t_0$;

$$R_b = \sqrt{\frac{2A}{B}\left(1 - \frac{1}{\sqrt{1 + B(t - t_0)}}\right)}$$

$$A = \sqrt{\frac{3\pi G^2 \rho}{\sigma^2}\frac{\mu^2}{M_b}a_0^3} \qquad B = a_0 s; \tag{3.11}$$

it is obviously valid only for $t \geq t_0$.

Fig. 3.10 compares the evolution of R_b in the simulations to what obtained from the above equation, for models P3e and P3u: our model seems to well reproduce the data. It is worth noting that the normalization of the curve in the plots (i.e., the value of $\sqrt{2A/B}$) is somewhat arbitrary, depending on the value one picks for the SMBHB semimajor-axis a_0 at which R_b starts growing.[8] This is due to the fact that the angular momentum exchange is proportional to the internal binary angular momentum, which is much larger near the binary formation time and strongly declines later. This also means that the interactions effectively displacing the binary from the centre are those occurring shortly after the binary formation time, while the ones occurring later impact less and less the external binary angular momentum evolution.

It is also worth accounting for the fact that dynamical friction should be acting on the binary CoM to bring it back to the centre, as it happens for the single SMBH (Fig. 3.9). While in the beginning of the evolution the simulations clearly show that dynamical friction is subdominant compared to stellar interactions in inducing the evolution of R_b, this could be no longer true at later times. In order to check the relative importance of the two effects, we can compare the torque on the binary CoM on the right-hand side of Eq. 3.7 to the torque we expect from dynamical friction.

However, the magnitude of dynamical friction in the present configuration cannot be trivially estimated, owing to the fact that the binary moves very close to the centre of a cored stellar distribution, in which fast moving stars may have an important contribution, and in which the estimate of the minimum and maximum impact parameter can be somewhat arbitrary. For this, we estimated the DF empirically, only focussing on the equal mass prograde runs.

---

[8] Shortly after the binary formation (and in coincidence with the onset of the growth of R_b) the binary shrinks very quickly. Given the dependence of $R_b \propto a_0^{3/4}$, by picking different values of a_0 we obtain curves whose value gets larger or smaller by a factor of a few; we believe this uncertainty is intrinsic in our simple treatment and we still believe our modelling can capture the evolution of R_b to a decent degree.

We start considering the time over which the single SMBH of run P2u shown in Fig. 3.9 is dragged back into the centre, given its initial angular momentum $L_{\rm ext} = M_b R_b v_b(R_b) \approx 6 \times 10^{-5}$ (Tab. 3.2 and Eq. 3.8), to write the associated dynamical friction torque as $dL_{\rm DF}/dt \approx \Delta L_{\rm ext}/\Delta t \approx 5 \times 10^{-7}$. This should be compared to the right hand side of Eq. 3.7, which can be rewritten, for the equal mass prograde cases, as $dL_{\rm ext}/dt \approx 1.8 \times 10^{-3} a^{3/2}$; this implies the two contributions to the evolution of the binary external angular momentum to be equal for $a \approx 4.3 \times 10^{-3}$, and dynamical friction to be a factor 10 more efficient than stellar interactions at $a \approx 9.2 \times 10^{-4}$. As a consequence, we expect that the binary should sink back towards the centre less than a hundred time units after the end of our prograde runs at $t \approx 180$.

The model presented so far also allows to understand why the CoM does not undergo analogous oscillations in the retrograde scenario: in that case, stars can only deposit angular momentum that has opposite sign compared to the binary one, thus they reduce the binary internal angular momentum instead of inducing a net oscillation in its CoM: this is supported by the fact that the eccentricity undergoes a continuous growth in the counter-rotating run (Fig. 3.3). In principle, over sufficiently long timescales, the counter-rotating binary is expected to eventually flip the sign of its angular momentum and finally circularize (Gualandris et al., 2012a; Sesana et al., 2011). However, since the external angular momentum growth occurs about the binary binding, and it is much less efficient at later times, we expect counter-rotating binaries to always remain close to the centre, even once they become prograde.

3.4 Conclusion

We investigated the impact of spherical rotating stellar systems on the hardening of SMBHBs through N-body simulations.

We found that the CoM of prograde binaries starts moving on quasi-circular orbits around the centre of the host galaxy. Such motion is considerably larger than the typical Brownian wandering experienced by SMBHBs evolving in isotropic backgrounds, and introduces a time-dependence in the loss-cone of the binaries, that remains full during their whole shrinking. We demonstrated through dedicated numerical experiments that such results (the enhanced binary CoM wandering and the fast hardening rate) are not valid for retrograde binaries nor for single SMBHs.

A key distinction in our study from previous research (Holley-Bockelmann & Khan, 2015; Khan et al., 2020; Mirza et al., 2017) resides in the fact that we model the host galaxy with a spherical distribution. In this way, by avoiding effects induced by deviations from spherical symmetry, we showed that rotation alone can drive both SMBHB circling and increased hardening.

Complementing our numerical findings, we present a phenomenological analytical model supporting the observed binary CoM evolution in prograde runs.

An important departure from Holley-Bockelmann & Khan (2015) lies in our discovery regarding the hardening rates of retrograde binaries. In the rotating-spherical scenario, retrograde binaries exhibit slower shrinkage compared to their prograde counterparts, a discrepancy not observed in the rotating-flattened scenario. Our analytical model attributes this difference to the absence of significant CoM motion in retrograde binaries, hindering collisionless loss-cone refilling.

Both from our semianalytical model and in the numerical simualtions emerges that SMBHBs experience substantial external angular momentum growth immediately after formation, especially at large semi-major axes. This implies that binaries with internal angular momentum significantly differing from their surroundings would not undergo CoM circling and consequent enhanced hardening.

<div align="right">4</div>

An effective model for the tidal disruption of satellite galaxies in minor mergers

Minor mergers are recurring events throughout galaxy lifetimes. In these scenarios, secondary galaxies act as massive perturbers to the primary galaxy potential, which make this systems particularly suitable for semi-analytical modelling, facilitating investigations with low computational demands. Of particular interest within the context of galactic mergers are the MBHs residing in the progenitor nuclei. Indeed, galaxy mergers can bring multiple MBHs into a single host, potentially forming MBHBs. These systems are prime targets for space based GW experiments, including PTA (Agazie et al., 2023; Antoniadis et al., 2023) and LISA (Amaro-Seoane et al., 2017). Before MBHs form bound systems in galactic nuclei, they must migrate towards the central regions of the newly formed host galaxy, primarily driven by dynamical friction (Chandrasekhar, 1943b). During this phase, MBHs are often surrounded by remnants of their progenitors' cores, enhancing their effective sinking mass and promoting dynamical friction. However, the surrounding material is gradually stripped by the host galaxy's tidal field (Binney & Tremaine, 2008). This mass loss significantly influences the dynamics of MBH inspiral and the efficiency of dynamical friction. Quantifying the stripping of material from infalling satellite galaxies necessitates estimating the tidal radius, which defines the boundary between bound and unbound mass. Initially proposed by von Hoerner (1957) the tidal radius was theoretically defined for satellites orbiting in circular orbits, where coincides with the L1/L2 Lagrange points (Binney & Tremaine, 2008). King (1962) attempted to extend this definition to eccentric orbits, suggesting that during pericenter passages, satellites are truncated to the size indicated by the pericentric tidal radius. Later, Henon (1970) and Keenan & Innanen (1975) observed that retrograde orbits in the context of the restricted three-body problem are stable over greater distances compared to prograde orbits, further out the tidal radius defined by King (1962). In a more recent

study, Read et al. (2006) derived an expression for the tidal radius taking into different orbit types: prograde, radial, and retrograde. Interestingly, the analysis revealed that the tidal radius for retrograde orbits exceeds that of radial orbits, which, in turn, is larger than the tidal radius for prograde orbits. To date, the vast majority of attempts to estimate the tidal radius focused on spherically symmetric host galaxies (see however Gajda & Łokas, 2016). Real galaxies show quite diverse morphologies, that can strongly deviate from spherical symmetry, calling for a dedicated investigation. In this study, I aimed to establish a general description of the tidal radius when axisymmetric systems are involved. Such systems, representative of, for example, spiral galaxies, are quite common, and many minor mergers occur in such galaxies. As additional elements of novelty, the proposed model allows for close encounters of the satellite with the host center along eccentric orbits, and it also accounts for non-instantaneous satellite mass loss. Ultimately, this new prescription for the tidal-stripping-driven mass loss of satellite galaxies enhances the accuracy of semi-analytical models in predicting the mass evolution of satellite galaxies and their pace of dynamical friction-driven inspiral within host galaxies of varying morphologies.

4.1 Methods

The mass loss caused by tidal effects can significantly impact the orbital decay of the satellite, as it reduces the efficiency at which dynamical friction drags the satellite galaxy towards the center of its host, thus increasing its orbital decay time.

4.1.1 Tidal Radius

To characterize the mass loss of satellite galaxies due to tidal stripping in minor mergers, the first step consists of defining the tidal radius. The standard approach in literature considers two spherically symmetric systems, with mass profiles $m(r)$ for the satellite, and $M(r)$ for the host galaxy, whose centres are separated by a distance R. The satellite tidal radius R_t is defined as the distance from the center of the satellite at which the acceleration of a test particle along the direction connecting the center of the two systems vanishes. In a minor merger scenario where $m \ll M$, under the assumptions that $R_t \ll R$ at any time, and that the test particle has null velocity in the satellite's reference frame, R_t is given by:

$$R_t = R \left[\frac{Gm(R_t)}{\Omega^2 - \frac{\mathrm{d}^2 \Phi_h}{\mathrm{d}r^2}} \right]^{\frac{1}{3}}. \tag{4.1}$$

This expression was first derived in King (1962) [1], where r and Ω are the radial coordinate and the angular velocity of the satellite in the reference frame of the host galaxy, and $\Phi_h(r)$ is its gravitational potential. It is worth noting that this formula is strictly valid for circular orbits, but can be easily extended to eccentric orbits if one considers instantaneous values for Ω and R. Additionally, it is important to emphasize that Eq. (4.1) holds only under the simplistic assumption of a spherical host.

In this study, we aim to present a novel prescription for R_t that is adaptable to various host geometries. For this purpose, we consider a spherically symmetric satellite galaxy embedded in the generic potential of its host. We define the galactic inertial frame with the origin in the galactic center denoted as S and the non-inertial frame of the satellite as S'. In this work, all the quantities evaluated in the non-inertial frame of the satellite are primed, while the unprimed are relative to the inertial frame of the host galaxy. Considering a test satellite star, its position is identified by the radius vector $\mathbf{r}_*$. The acceleration of the test star in the reference frame of the satellite is:

$$\mathbf{a}' = \mathbf{a} - \mathbf{A} - \frac{d\mathbf{\Omega}}{dt} \times \mathbf{r}'_* - \mathbf{\Omega} \times (\mathbf{\Omega} \times \mathbf{r}'_*) - 2\mathbf{\Omega} \times \mathbf{v}'. \tag{4.2}$$

Here, Ω is the angular velocity of the satellite centre of mass (CoM), $\mathbf{a}$ represents the acceleration of the test star in the S frame:

$$\mathbf{a} = -\frac{GM_s(r'_*)}{r'^3_*}\mathbf{r}'_* - \nabla\phi_h(r_*), \tag{4.3}$$

and $\mathbf{A}$ is the acceleration of the S' frame in S, which can be expressed as:

$$\mathbf{A} = -\nabla\phi_h(r_S), \tag{4.4}$$

where r_S indicates the distance of the satellite CoM from the host's center. The term $\mathbf{\Omega} \times (\mathbf{\Omega} \times \mathbf{r}'_*)$ can be rewritten as $\Omega^2 r'_*(\cos\alpha - 1)$, with α being the angle between $\mathbf{\Omega}$ and $\mathbf{r}'_*$. Choosing a random direction $\hat{\mathbf{e}}_{\mathbf{r}'*}$ from the center of the satellite, we can approximate the tidal radius as the distance along the fixed direction $\hat{\mathbf{e}}_{\mathbf{r}'*}$ from the satellite centre at which a test star with $v' = 0$ experiences a vanishing $\mathbf{a}'$.

$$a'_{\hat{\mathbf{e}}_{\mathbf{r}'_*}} = 0 = -\frac{GM_s(r'_*)}{r'^2_*} - \nabla\phi_h(\mathbf{r}_*)\cdot\hat{\mathbf{e}}_{\mathbf{r}'*} + \nabla\phi_h(\mathbf{r_S})\cdot\hat{\mathbf{e}}_{\mathbf{r}'*} - \Omega^2 r'_*(\cos\alpha - 1), \tag{4.5}$$

where we omitted the term $d\Omega/dt \times \mathbf{r}'_*$ which is directed perpendicularly to $\hat{\mathbf{e}}_{\mathbf{r}'*}$, thus not contributing to the acceleration along the reference direction we fixed. It is important to note that, unlike the derivation in King (1962), we relax the assumption $R_t \ll R$, therefore allowing the satellite to undergo close encounters with the host center. Eq. (4.5) thus provides an implicit definition for R_t along a specific direction from the center of the satellite. As mentioned

---

[1]See sec. 1.3.2 for the derivation.

above, if the host system is spherically symmetric, the reference direction along which the R_t is evaluated is the one connecting the center of the two galaxies, since it is the direction that maximizes the tidal force. However, in a generic galactic field it is not possible a priori to define the direction that maximizes the tidal force exerted on the satellite by the host, which instead will depend on the morphological parameters of the two systems and on the instantaneous location of the satellite within the host potential. For this reason, during the satellite evolution we numerically solve Eq. (4.5) along 1000 random directions and we select R_t as the minimum of all the tidal radii evaluated, that we denote as R_{T1}. However, the mass of the satellite is not instantaneously stripped and it is not possible a priori to define at which rate the material is removed through Eq. (4.5). For this reason, at any time we introduce a modified definition of the tidal radius, i.e.

$$R_{T2}(t) = R_T(t_{\text{old}})\, e^{-\alpha \frac{t-t_{\text{old}}}{r_p/v_p}}. \tag{4.6}$$

In Eq. (4.6), $R_T(t_{\text{old}})$ is the tidal radius evaluated at a prior time t_{old}, r_p and v_p are the distance and velocity of the satellite with respect to the host centre both evaluated at the pericenter, while α is a tunable dimensionless parameter that regulates the rate at which the mass is removed from the satellite: the higher the value of α, the faster the mass is stripped. Thus, comparing R_{T1} and R_{T2} we define R_T to be:

$$R_T(t) = \max(R_{T1}(t), R_{T2}(t)). \tag{4.7}$$

Finally, we require the tidal radius to be a decreasing function of time. This condition implies that the removed material is irrevocably detached from the satellite, precluding any subsequent reattachment in later times, effectively assuming that tidal stripping is irreversible.

4.1.2 Satellite galaxy

In this study, we characterize the satellite galaxy employing the spherical and isotropic Hernquist model (Hernquist, 1990), whose potential and the associated mass density profile are given by:

$$\Phi_s(r) = -\frac{GM_s}{r + a_s}, \tag{4.8}$$

$$\rho_s(r) = \frac{M_s}{2\pi} \frac{a_s}{r(r + a_s)^3}, \tag{4.9}$$

where M_s and a_s are the total mass and scale radius of the satellite. The corresponding mass profile is $m_s(r) = M_s[r/(r+a_s)]^2$ We integrate the satellite orbit with the semi-analytical code GALCODE described in Bonetti et al.

(2020b), in which we incorporated the evolution of the tidal radius as detailed in Section 4.1.1. We truncate the satellite mass profile integrating $m_s(r)$ up to R_t. The semi-analytical framework features a comprehensive treatment of the dynamical friction specifically tailored to account for flattened and rotating systems (Bonetti et al., 2021b, 2020b). It is also equipped with a prescription for the interactions of massive perturbers with galactic substructures such as bars (Bortolas et al., 2022).

4.1.3 Host galaxy

In the present work, we explore two different models for the host galaxy: a single-component and a double-component host galaxy. In the first scenario, the primary galaxy is characterized by an isolated exponential disc, defined by the density profile:

$$\rho_d(R, z) = \frac{M_d}{4\pi R_d^2 z_d} e^{-\frac{R}{R_d}} \operatorname{sech}^2\left(\frac{z}{z_d}\right). \tag{4.10}$$

Here M_d is the total mass of the disc, R_d and z_d are the scale radius and height of the disc, respectively. An analytical approximate expression for the potential of such a model exists only within the galactic plane. Consequently, accelerations caused by the disc potential outside the galactic plane are determined through numerical interpolation of tabulated values, which are computed over an adaptive grid, see Bonetti et al. (2021b, 2020b) for details. Single-component host galaxy models were employed to test simple systems, in which we neglect dynamical friction to focus on the tidal effects regulating the evolution of the satellite mass.

In the case of a composite host galaxy, the disc is embedded within a spherical dark matter halo. The potential of this halo follows the Hernquist profile, characterized by a total mass M_h and a scale radius a_h:

$$\Phi_h(r) = -\frac{GM_h}{r + a_h}. \tag{4.11}$$

4.1.4 N-body simulations

Our investigation was complemented by a comparative analysis, where we accompanied the proposed semi-analytical prescription regulating the tidal-stripping-driven mass evolution of satellite galaxies with N-body simulations. This approach enables us to evaluate the ability of our model to accurately encompass all the relevant physical processes involved and identify potential missing effects. N-body simulations were performed employing the publicly available code GADGET4 (Springel et al., 2021)

In all the tested systems, the satellite galaxy is modelled with 10^5 stellar particles. The particle positions are initialized to follow the mass distribution in Eq. (4.9), while the velocities are generated at equilibrium in the potential

generated by the stellar distribution. The initial satellite mass is fixed to be equal across all models, with $M_s = 10^8 M_\odot$. We considered three different values for the satellite scale radius , i.e. $a_s = 0.1, 0.5, 1$ kpc, thus testing different mass concentrations.

Table 4.1: Parameters of the host galaxy for both single and the double component scenarios.

Component	Profile	M	scale radius	scale height	N_{part}	ϵ
Single-component						
Disc - analytical	exponential	$4.4 \times 10^{10}\,\mathrm{M_\odot}$	4.25 kpc	$0.85\,\mathrm{kpc}$	-	-
Double-component						
Disc	exponential	$4.4 \times 10^{10}\,\mathrm{M_\odot}$	$4.25\,\mathrm{kpc}$	$0.85\,\mathrm{kpc}$	4.4×10^7	$5\,\mathrm{pc}$
Halo - analytical	Hernquist	$1.1 \times 10^{12}\,\mathrm{M_\odot}$	$37\,\mathrm{kpc}$	-	-	-

The satellite is then embedded within the primary galaxy at a distance of $R_i = 10$ kpc from its center and with a specific initial velocity, which is added to the stars as a bulk velocity. We explore the orbital parameter space by changing both the initial velocity of the satellite CoM ($v_i/v_c = 0.75, 0.50, 0.25$, where v_c is the circular velocity at R_i), and different initial inclinations of the satellite orbit with respect to the galactic plane ($\theta = 0°, 30°, 60°, 90°$). We set the softening parameter $\epsilon = 1$ pc for the satellite particles, while we fix $\epsilon = 5$ pc for the stellar particle of the disc component in multi-component galaxy models. To isolate the impact of tidal forces on the evolution of the satellite mass from other possible influencing processes, we first performed a set of simulations excluding the effect of dynamical friction. To achieve this, the host galaxy is included in N-body simulations as a stationary semi-analytical potential, instead of being modelled using collisionless particles. To do so, we add to the acceleration of satellite particles the acceleration induced by the presence of the host potential. As mentioned in the previous section, all the models in which we omit dynamical friction host a primary galaxy modelled with a single exponential disc.

The method we implemented in GADGET4 to compute the accelerations generated by the exponential-disc potential is analogous to the one we use in the semi-analytical code and described in sec. 4.1.3. This set up prevents gravitational interactions between satellite and field stars, thereby avoiding dynamical friction to take place.

We then consider more complex systems composed by a satellite orbiting in a double-component host galaxy, also including effects from dynamical friction. In these systems, the primary galaxy consists of an analytical dark matter halo, whose potential is given by Eq. 4.11, and an exponential-disc, modelled with 4.4×10^7 stellar particles, whose mass density is given by Eq. (4.10). The initial conditions for the disc were performed using the public code GALIC (Yurin & Springel, 2014) which is based on an iterative approach to build N-body galaxy models at equilibrium. Similarly to the case of the analytic disc, the dark matter halo contributes solely through the acceleration its potential

imprints on the stellar particles - that we compute and add to the satellite particles in the simulation -, thus giving null contribution to the dynamical friction.

The host galaxy parameters are summarized in Table 4.1.

4.1.5 Satellite CoM and bound particles

The upper panels in Fig. 4.1 show satellite particles in one of the tested models (specifically the system composed by a satellite with $a_s = 0.5$ kpc, orbiting in the galactic plane of an exponential disc host, with initial velocity $v_i = 0.5\,v_c$) at the first, middle and final snapshot of the simulation. The plots' origin coincides with the center of the host galaxy potential. Orange particles are bound to the satellite, while gray particles indicate those that have been stripped. The shaded thin red line shows the trajectory predicted by the semi-analytical model, while the thick solid red and blue lines track the satellite CoM, in the semi-analytical model and in the N-boy simulation, respectively. In each snapshot of the simulation the bound particles are identified through an iterative approach. The first step consists of identifying the position and velocity of the satellite CoM. We initialize the satellite CoM location as the point corresponding to the highest density. For each of the satellite particles we compute the binding energy as:

$$E_* = \frac{1}{2}|\mathbf{v}_* - \mathbf{v}_{\mathrm{CoM}}|^2 - \Phi_{\mathrm{Trunc\,Hern}}(r_*). \tag{4.12}$$

Here v_* is the velocity of the star, v_{CoM} is the velocity of the satellite CoM, and $\Phi_{\mathrm{Trunc\,Hern}}(r_*)$ is the potential generated by an Hernquist model, truncated at a certain radius r_{max}, which is given by:

$$\Phi_{\mathrm{Trunc\,Hern}}(r_*) = \begin{cases} GM_s\left(\frac{1}{r_{\mathrm{max}}+a_s} - \frac{1}{r_{\mathrm{max}}} - \frac{1}{r_*+a_s}\right) & \text{if } r_* < r_{\mathrm{max}} \\ -\frac{GM_s}{r_*} & \text{if } r_* \geq r_{\mathrm{max}} \end{cases}, \tag{4.13}$$

where r_* is the distance of the selected star from the satellite center. To set the truncation radius r_{max}, at each snapshot we start from an initial guess of $r_{\mathrm{max}} = 10a_s$, then, we consider enlarging spherical shells centered in the satellite CoM, with a fixed width $\delta_r = 0.25a_s$. The value of r_{max} is then chosen to correspond to the median radius of the smallest shell containing a number of unbound stars exceeding twice the number of the bound ones (i.e. such that $N_{\mathrm{unbound}} \geq 2N_{\mathrm{bound}}$). Finally, we update the CoM location and velocity with the values computed using the stars with $E_* < 0$. The procedure is iteratively repeated until the CoM position converges to a constant point, with a relative error on the position of the CoM lower than 10^{-3}.

The lower panels in Fig. 4.1 show the satellite cumulative mass profile at the same snapshots and for the same system as in the upper panels. The black solid curve displays the theoretical cumulative mass profile from the Hernquist model. The other two profiles are constructed using the bound particles only,

in orange, and all the particles that were part of the satellite at the initial time, in gray. The vertical blue line shows the value of the tidal radius computed with our semi-analytical prescription at the same time of the simulation. Thus, the satellite mass resulting from the simulation, given by the value at which the orange curve saturates, can be compared to the value predicted by our semi-analytical model, i.e. the value at which the theoretical profile is truncated by the tidal radius.

4.1.6 Mass evolution and choice of the optimal α parameter

We compare outcomes of N-body simulations with the results of our semi-analytical prescription, testing different values of the α parameter, which controls the mass-stripping rate. A higher α corresponds to a faster mass removal. The panels in Fig. 4.2 illustrate the temporal evolution of the satellite mass of a satellite with $a_s = 0.5$ kpc orbiting within the host galactic plane, for three different initial velocities: $v_i/v_c = 0.75\,,0.5\,,0.25$. The black line shows the evolution of the mass resulting from N-body simulations. The colored solid lines display the mass evolution predicted by the semi-analytical model for different values of α, spanning from 0.05 up to 5. The minimum tidal radius computed at each time is indicated with a gray dashed line, which indicates the value of the satellite mass one would predict if the stripping were considered instantaneous and reversible. It is important to notice that the initial configuration of the simulated systems is not at the equilibrium. This is because the satellite is generated in isolation and then artificially placed within the primary galaxy potential, instead of following the merger from its initial phases. Therefore, we use the position and velocity of the satellite CoM in the N-body simulation at the first apocenter as the initial condition for the semi-analytical model calculations. In Fig. 4.2, the orbit from the beginning of the N-body simulation to the first apocenter is indicated by the grey shaded region. Finally, using a least square method on the mass evolution, we determine the optimal value of α corresponding to the semi-analytical model that most accurately reproduces the N-body simulations.

In the next section, we will discuss the results of our model, focusing in particular on the model ability to reproduce the evolution of the satellite mass.

4.2 Results

4.2.1 Models without dynamical friction

We started our study examining simple systems composed of a satellite orbiting within the analytical potential of its host. This configuration enables us to exclude dynamical friction, thereby isolating the effects solely determined by
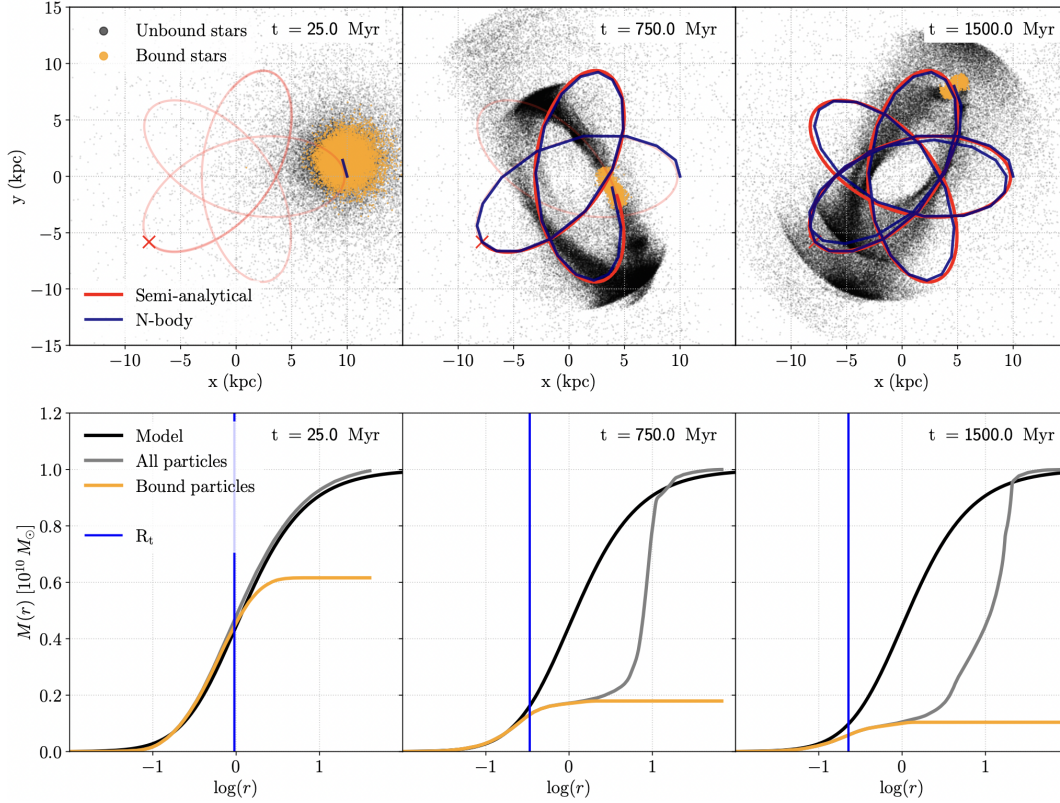
Figure 4.1: *Upper panels*: satellite particles of an example run featuring a satellite with $a_s = 0.5$ kpc, orbiting in the galactic plane of an exponential disc host, with initial velocity $v_i = 0.5\,v_c$. From left to right, the three panels correspond to the first, middle and final snapshot of the simulation. The origin coincides with the center of the host galaxy potential. The colors indicate which particles are bound to the satellite (orange) or unbound (gray). The shaded red line shows the trajectory predicted by the semi-analytical model, while the solid red and blue lines track the satellite CoM, in the semi-analytical model and in the N-boy simulation, respectively. Finally, the red cross indicates the initial point for the semi-analytical orbital integration, corresponding to the first apocenter. *Lower panels*: satellite cumulative mass profiles at the same snapshots and for the same system as in the upper panels. The black solid curve displays the theoretical cumulative mass profile from the Hernquist model. The other two profiles are constructed using the bound particles only, in orange, and all the particles that were part of the satellite at the initial time, in gray. The vertical blue line shows the value of the tidal radius computed with our semi-analytical prescription.
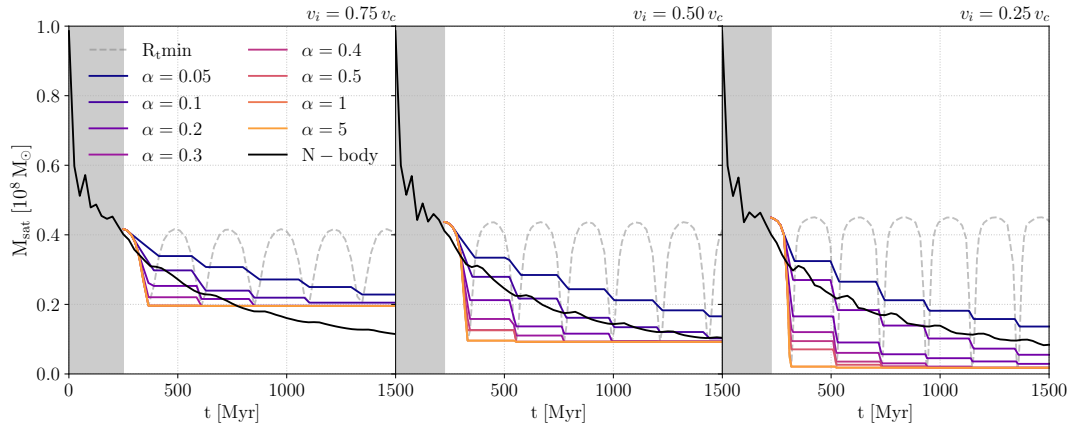
Figure 4.2: Evolution of the satellite mass as a function of time for three cases with $a_s =$ 0.5 kpc, orbiting within the host galactic plane and featuring different initial velocities ($v_i/v_c = 0.75, 0.5, 0.25$, from left to right). The black line shows the evolution of the mass according to the N-body simulations. The colored solid lines correspond to the mass evolution predicted by the semi-analytical model with different values for α, spanning the range $[0.05 - 5]$. The gray dashed line represents the minimum tidal radius computed at each time, whereas the gray region represents the time from the beginning of the N-body simulation to the first apocenter, which is the starting point for the semi-analytical models.

tidal forces. In this scenario, the primary galaxy is characterized by an isolated exponential disc, defined by the density profile in Eq. (4.10).

Fig. 4.3 displays the optimal values of the α parameter for each model, evaluated as detailed in sec. 4.1.6. More in detail, the three panels show how the $\alpha_{\rm best}$ parameter changes with the initial orbital velocity (or initial eccentricity) in models sharing the same satellite scale radius a_s, each panel referring to a different value of a_s, and the same orbital inclination, reported with different line styles and colors. In general, most systems exhibit a slight increase in the α parameter as the initial velocity approaches the circular velocity, while no evident trends in the values of α can be outlined when varying the scale radius and the orbital inclination. As expected, a lower α is associated to systems with initial higher eccentricity (or lower initial velocity). This is attributed to the abrupt decrease in the tidal radius at pericenter passages, as predicted by Eq. (4.5), leading to a significant and instantaneous mass loss. However, the actual timescale to strip material from the satellite, as predicted by N-body simulations, is longer than the fast pericenter passages. For this reason, in the vicinity of the pericenter, the tidal radius decrease is delayed using Eq. 4.6, with α regulating the rapidity of the mass removal. Since this effect is much more relevant along eccentric orbits, the α parameter needs to be small enough to slow down the satellite mass loss, which otherwise would be extreme, and is expected to be smaller compared to systems with low eccentric orbits. If not explicitly specified, all the results presented in this section refer to the specific semi-analytical model characterized by the optimal value of α for each system considered.
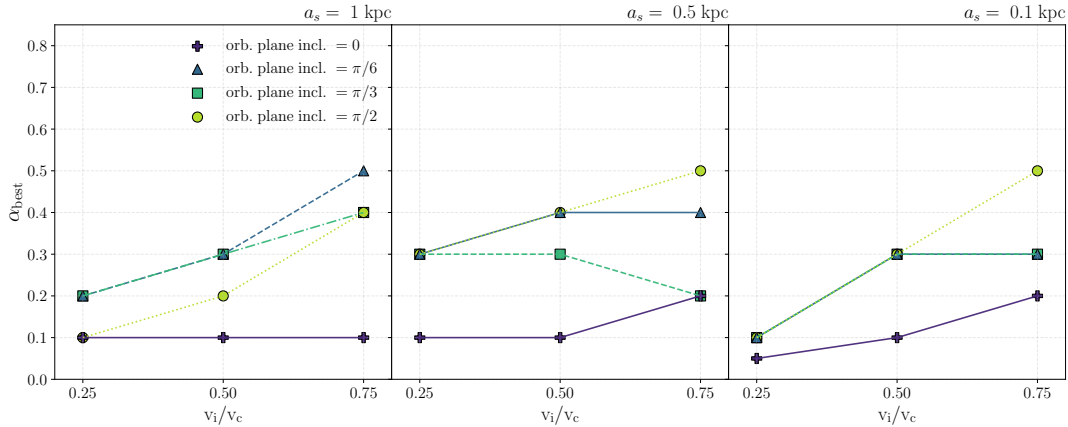
Figure 4.3: Optimal values of the α parameter for each model without dynamical friction as a function of the initial orbital velocity (or initial eccentricity). Each panel considers a system with fixed satellite scale radius a_s, decreasing from left to right, with varying linestyles and color codes indicating different orbital inclinations.
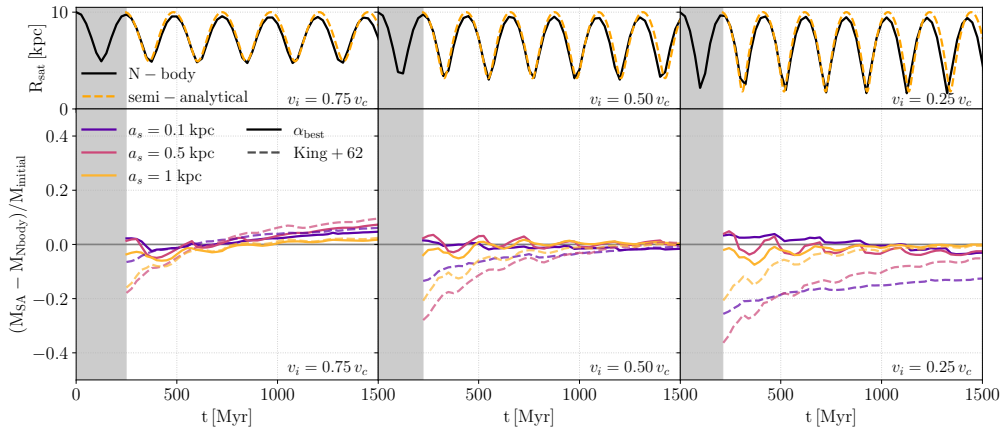

Figure 4.4: Results obtained for systems hosing satellites orbiting within the galactic plane without dynamical friction. The three panels refers to different initial velocities for the satellite CoM, $v_i = 0.75v_c$, $v_i = 0.5v_c$ and $v_i = 0.25v_c$ form left to right. *Upper panels*: separation of the satellite CoM from the primary galaxy center as a function of time. The orange dashed line refers to the semi-analytical model, while the black solid line shows the result of the N-body simulations. *Bottom panels*: time-evolution of the difference between the satellite mass predicted by the semi-analytical model and the mass resulting from N-body simulations, normalized to the initial satellite mass. The line colors indicate different satellite scale radii. The solid lines refer to our new semi-analytical prescription for the evolution of the satellite mass, whereas the dashed lines represent the results we obtain using King's formula for the tidal radius. In both panels, the gray area indicates the time interval leading to the first apocenter.

In Fig. 4.4, we present the results of the comparison between our semi-analytical prescription and N-body simulations for models with the satellite moving within the galactic plane. The upper panels depict the evolution of the separation of the satellite CoM from the primary galaxy center. The semi-analytical model's predictions are shown in orange, while the N-body simulation results are represented by a black solid line. The bottom panels show the time evolution of the difference between the satellite mass (normalized to the initial satellite mass) predicted by the semi-analytical model and the mass resulting from N-body simulations. The three panels correspond to different initial velocities of the satellite, with line colors indicating the satellite scale radius. Our semi-analytical prescription well reproduces both the orbital and the mass evolution of the satellite.

As an additional test, we compare our semi-analytical prescription for the tidal radius and mass evolution (solid lines) with results obtained using King's formula (dashed lines), see Eq. (4.1). We observe an overall better agreement with N-body simulations using our new semi-analytical prescription compared to the King prescription. This result is due to multiple factors. First, King's formula, when applied without any delay for mass removal, implies instantaneous mass stripping. This leads to a general underestimation of the satellite mass, especially in the initial phases of the evolution. Moreover, one of the main assumptions in King's prescription is that the tidal radius should be much lower than the separation between the centers of the two galaxies, thereby excluding close encounters. This assumption is generally valid along quasi-circular orbits, but it breaks when considering highly eccentric orbits where the pericenter can be at a close distance from the host center. The combined effect of the instantaneous mass stripping, which can be severe in eccentric orbits during the close pericenter passages, and the assumption of distant interactions, implies an increasing inability of King's prescription at reproducing the results of N-body simulations (see bottom right panel in Fig. 4.4) as the orbital eccentricity increases.

It is important to note that a comparison with King's prescription is meaningful only for systems in which the satellite is orbiting within the galactic plane, as far from the galactic plane King's definition of the tidal radius becomes ill-defined. In the coplanar case, indeed, the gradient of the host potential at the position of each satellite's star points approximately toward the host centre, making the comparison between our and King's prescriptions meaningful. Nonetheless, we stress that, even in this case, the acceleration of stars that during their orbits around the satellite centre lie above or below the plane of the host disc are not radial, and are, therefore, implicitly approximated in the treatment by King (1962).

Finally, we investigated systems where the satellite orbits outside the galactic plane, exploring various inclination angles. We show the evolution of the error in estimating the satellite mass for these systems in Fig. 4.5. The columns represent different initial velocities of the satellite CoM, decreasing from left to
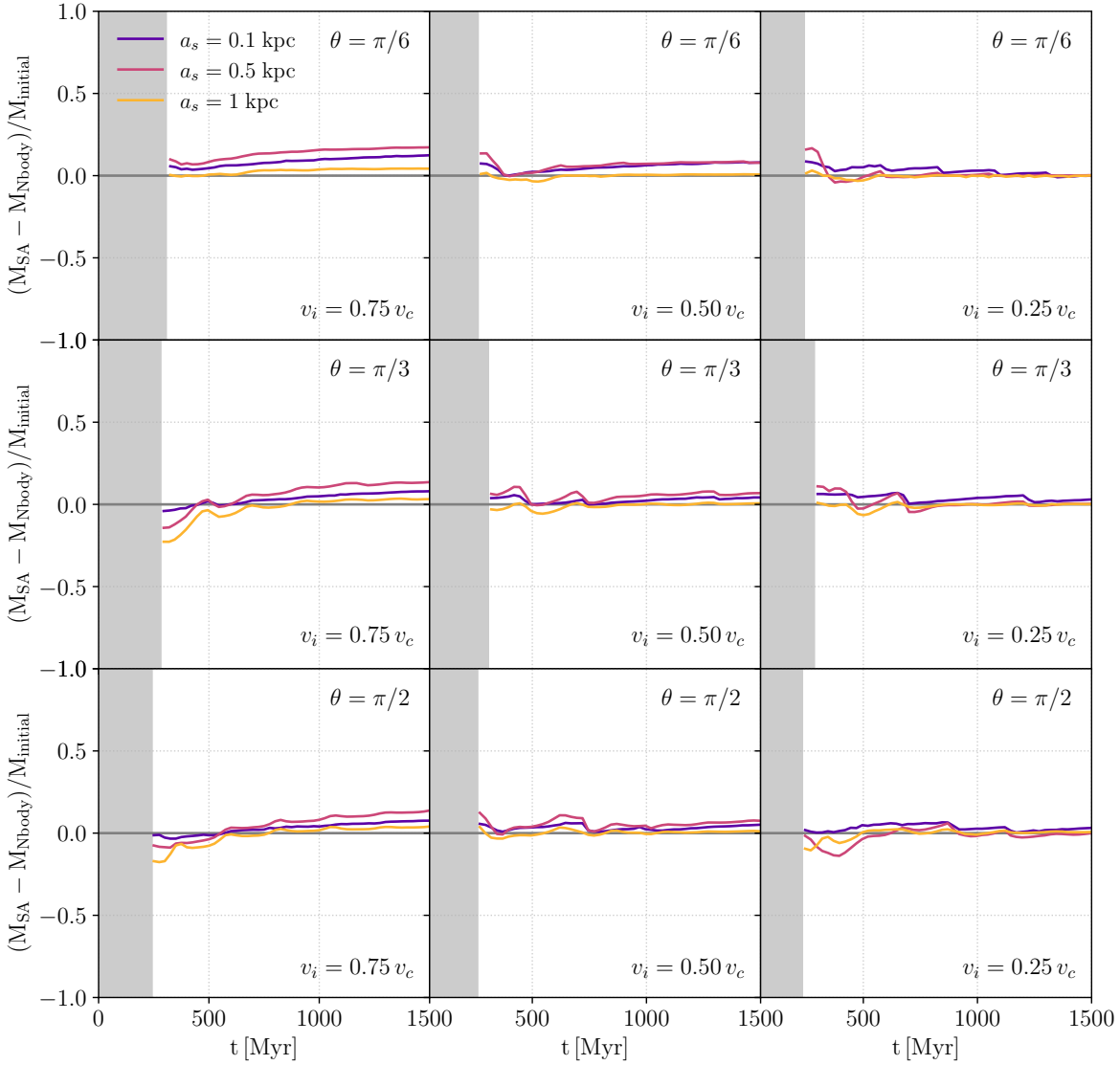
Figure 4.5: Error in estimating the satellite mass for systems on inclined orbits with respect to the galactic plane and without dynamical friction. The line colors indicate different satellite scale radii. The columns represent different initial velocities of the satellite CoM, decreasing from left to right, while the rows illustrate varying orbital inclinations, increasing in angle from top to bottom.

right, while the rows illustrate varying orbital inclinations, increasing in angle from top to bottom.

Our semi-analytical prescription effectively reproduces the evolution of the satellite mass along the orbit, particularly in systems with eccentric orbits, across all orbital inclinations. However, in systems hosting satellites with low-eccentricity orbits, our semi-analytical model tends to overestimate the satellite mass, as observed in the left panels of Fig.s 4.2, 4.4 and 4.5. We will delve into this behavior extensively in Section 4.2.3.

Validation of the model in the scenario of a spherically simmetric host

To further test the validity of the proposed model and explicitly compare its effectiveness to the King model, we conducted an additional set of simulations where the main galaxy exhibits spherical symmetry. To perform this simulations, we considered a system composed of a spherical satellite, analogous to those used in the prevously presented case of a disk-like host, with a Hernquist mass density profile having a total mass of $M_s = 10^8 M_\odot$ and a variable scale radius $a_s = 0.1, 0.5, 1$ kpc, sampled with 10^5 particles and softening parameter $\epsilon = 1$ pc. The host galaxy in this scenario is modeled using a Hernquist profile with $M_h = 4.4 \times 10^{10} M_\odot$ and a scale radius of 7.5 kpc. Analogously as in the other systems presented so far, the primary galaxy is introduced in the simulations as an analytical external potential. The results of these simulations are presented in fig. 4.6.
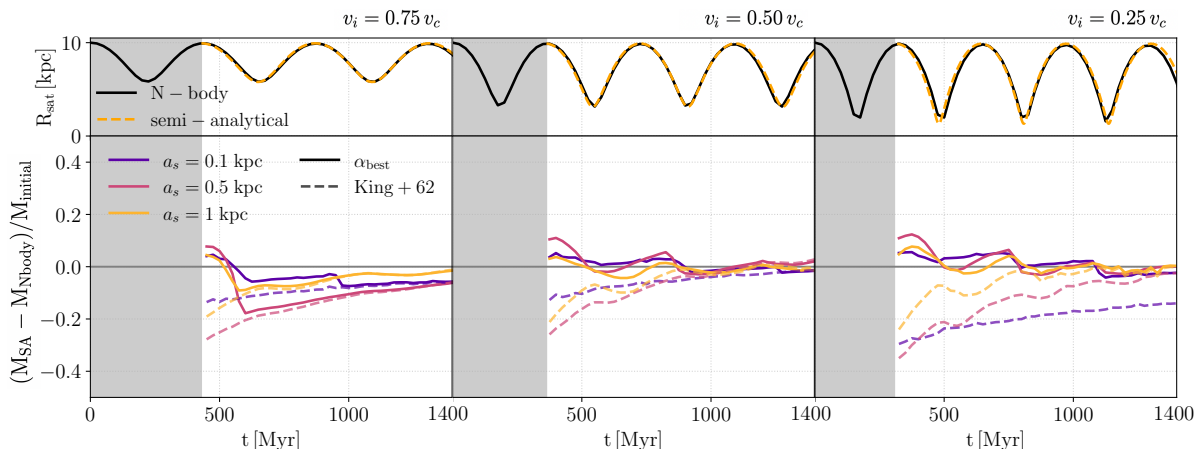

Figure 4.6: Results obtained for systems hosing satellites orbiting within a spherically symmetric host. The three panels refers to different initial velocities for the satellite CoM, $v_i = 0.75 v_c$, $v_i = 0.5 v_c$ and $v_i = 0.25 v_c$ form left to right. *Upper panels*: separation of the satellite CoM from the primary galaxy center as a function of time. The orange dashed line refers to the semi-analytical model, while the black solid line shows the result of the N-body simulations. *Bottom panels*: time-evolution of the difference between the satellite mass predicted by the semi-analytical model and the mass resulting from N-body simulations, normalized to the initial satellite mass. The line colors indicate different satellite scale radii. The solid lines refer to our new semi-analytical prescription for the evolution of the satellite mass, whereas the dashed lines represent the results we obtain using King's formula for the tidal radius. The gray area in the panels indicates the time interval leading to the first apocenter.

The different columns correspond to the three different initial satellite orbital velocities, decreasing from left to right. The upper panels show the comparison between the time-evolution of the radial separation of the centers of the two galaxies predicted by our semi-analytical model (orange dashed line) and the results from N-body simulations (solid black line).

Table 4.2: Values of the α parameter for the models with spherical host galaxy.

v_i/v_c	a_s		
	0.1 kpc	0.5 kpc	1 kpc
0.75	0.05	0.2	0.3
0.50	0.02	0.04	0.04
0.25	0.01	0.02	0.02

The bottom panels display the error in predicting the satellite mass by the semi-analytical model compared to the mass resulting from the simulations. The line colors correspond to varying satellite scale radii. Analogous to Fig. 4.4, solid lines depict the outcomes of our semi-analytical model characterized by its optimized α parameter, while dashed lines (with the same color scheme) represent the satellite mass predictions obtained using the instantaneous mass truncation defined by King's formula (Eq. 4.1). Our model appears to better reproduce the satellite mass evolution, even within spherically symmetric host systems. Notably, our model increasingly converges with the results of King's prescription as the initial satellite velocity approaches circularity. This alignment is expected and provides further validation of our model's robustness. Indeed, the scenario of a satellite galaxy orbiting within a spherical host with a velocity akin to v_c best matches the assumptions underlying King's formula, namely the distant tide approximation and the assumption of the satellite's motion along circular orbits.

the values of the best α parameter for the systems with a spherically symmetric host are listed in tab 4.2.

4.2.2   Models with dynamical friction

After assessing the capability of our model to replicate the effects of tidal stripping in a fixed analytical potential, we extend our analysis to include models where dynamical friction is considered. In this context, our study involves satellite galaxies orbiting within a multi-component host galaxy. As detailed in Table 4.1, the host galaxy in these models comprises a spherically symmetric dark matter halo, incorporated as an analytical potential in N-body simulations, and an exponential disk containing 4.4×10^7 stellar particles. Consequently, the dynamical friction experienced by the satellite stars is solely attributed to the disk component of the host galaxy. In contrast to the models examined thus far, the introduction of dynamical friction, as described in detail in the introduction, significantly influences the satellite's orbital evolution, which, in turn, plays a crucial role in shaping the tidal radius and consequently determining the extent of mass removal.

The combined effect of dynamical friction and mass loss is illustrated in Figure 4.7, where we report the result for one of the systems we tested (i.e. a satellite orbiting within the galactic plane with initial velocity of $v_i = 0.25v_c$
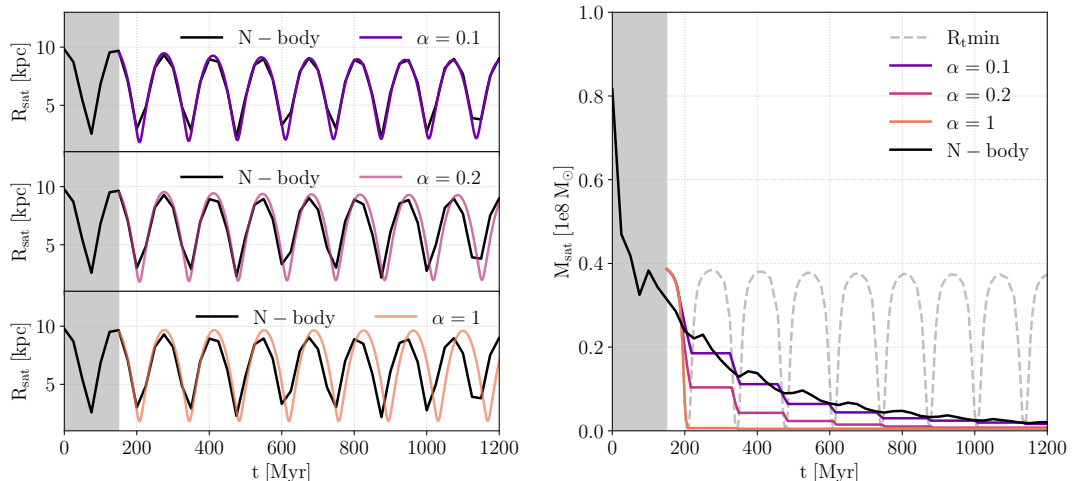
Figure 4.7: *Left panels*: time-evolution of the satellite's distance from the center of the host in the N-body simulation (black lines) compared to our semi-analytical model's predictions (colored solid lines). From top to bottom, each panel refers to different values of α: 0.1, 0.2, and 1, respectively. *Right panel*: mass evolution of the satellite in both N-body simulations and semi-analytical models, maintaining the same color code as in the left panels. The gray dashed lines indicate the minimum tidal radius among those evaluated along the 1000 different directions.

and $a_s = 0.5$ kpc). The left panels compare the satellite's distance evolution from the center of the host in the N-body simulation (depicted by the black line) with our semi-analytical model's predictions for three distinct α values (each represented by a colored solid line in a separate panel). Correspondingly, the right panel shows the satellite's mass evolution in both N-body simulations and semi-analytical models, maintaining the same color code as in the left panels.

Among the models investigated, the one corresponding to $\alpha = 0.1$ exhibits the best agreement with both the satellite's mass and orbital evolution. Conversely, models associated with higher values of α, corresponding to faster mass loss, demonstrate an increasing deviation from simulations results. This discrepancy arises from the rapid reduction in the satellite mass, which leads to a weakening of the dynamical friction drag, consequently slowing down the satellite's decay towards the host center.

The best values of the α parameter for all the investigated systems featuring a disc component in the host galaxy are summarized in Table 4.3. As highlighted in the previous section, models devoid of dynamical friction exhibit a consistent agreement between our semi-analytical model and N-body simulations, independently of the scale radius and orbital inclination, with a mild dependence on the initial orbital eccentricity only. Given this result, and the fact that simulations involving a host disk composed of $\gtrsim 10^7$ particles represent a quite high computational burden compared to simulations with entirely analytical hosts, we opt to focus our investigation on systems featuring a satellite with a fixed scale radius, $a_s = 0.5$ kpc, orbiting within the galactic
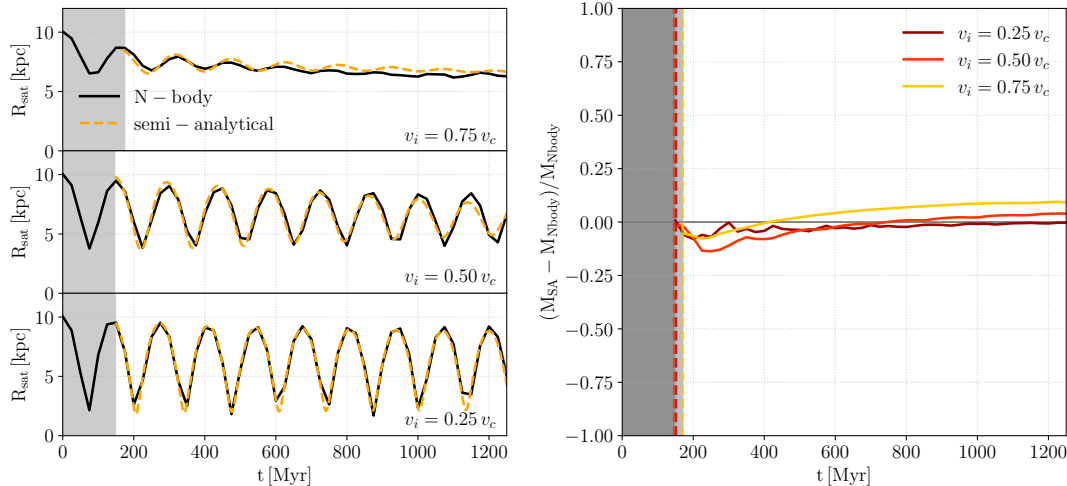
Figure 4.8: *Left panels*: comparison between the evolution of the satellite's CoM in both N-body simulations and semi-analytical models, each using the best value for α. The different panels correspond to the three different initial satellite's velocities, $v_i = 0.75v_c$, $v_i = 0.50v_c$ and $v_i = 0.25v_c$ from top to bottom. *Right panel*: relative error in the evaluation of the satellite mass for the same values of the initial velocities as a function of time. Different line colors indicate different initial satellite velocities. The dashed vertical lines represent the initial time of the semi-analytical models, which corresponds to the first apocenter, and are colored using the same color code employed for the solid lines.

plane. The primary parameter under consideration is therefore the variation in the satellite's initial velocity.

The results are shown in Fig. 4.8. The left panels compare the evolution of the satellite's CoM in both simulations and in semi-analytical models, each using the best value for α. From top to bottom, the different panels correspond to the three different initial satellite's velocities, $v_i = 0.75v_c$, $v_i = 0.50v_c$ and $v_i = 0.25v_c$. The right panel depicts the error in the evaluation of the satellite mass for the same values of the initial velocity. The dashed vertical lines represent the initial time of the semi-analytical models, which correspond to the first apocenter, and are colored using the same color code as the solid lines.

As noted in the previous cases, a very good agreement is observed between the results obtained from N-body simulations and the predictions from our semi-analytical models regarding the orbital evolution of the satellite and the associated mass decrease. Notably, this accord is particularly evident for systems featuring satellites on higher eccentric orbits, as consistently demonstrated across all the investigated systems.

4.2.3 Test on models with satellites on low-eccentricity orbits

In this section, we investigate in detail the processes contributing to the systematic overestimation of satellite mass in our semi-analytical model when com-

Table 4.3: Values of the α parameter for each model featuring a disc component in the host galaxy.

v_i/v_c	θ	a_s		
		0.1 kpc	0.5 kpc	1 kpc
No Dynamical friction				
	0	0.2	0.2	0.1
0.75	$\pi/6$	0.3	0.2	0.5
	$\pi/3$	0.3	0.2	0.4
	$\pi/2$	0.5	0.5	0.4
	0	0.1	0.1	0.1
0.50	$\pi/6$	0.3	0.4	0.3
	$\pi/3$	0.3	0.3	0.3
	$\pi/2$	0.3	0.4	0.3
	0	0.05	0.1	0.1
0.25	$\pi/6$	0.1	0.3	0.2
	$\pi/3$	0.1	0.3	0.2
	$\pi/2$	0.1	0.3	0.1
Dynamical friction				
0.75	0	-	0.1	-
0.50	0	-	0.1	-
0.25	0	-	0.1	-

pared to N-body simulations in systems harboring satellites on low-eccentricity orbits. Two primary processes may account for this discrepancy. The first involves tidal heating resulting from rapid changes in the host potential experienced by the satellite, as described in sec. 1.3.2. Another possible factor is the satellite's evaporation induced by mass truncation. During pericenter passages, where the majority of stripping occurs, a substantial portion of the satellite mass is expelled from the system, leading to truncation in the satellite mass distribution. As a result, the satellite is no longer in equilibrium. As it evolves towards a new equilibrium, its mass distribution expands, causing stars with higher velocities to migrate to larger radii. As a consequence, the satellite's profile changes becoming less concentrated, thereby facilitating the particles in the outer layers to become unbound. This results in a continuous mass loss, even if the tidal radius undergoes minimal change, particularly along quasi-circular orbits.

In order to discern the predominant process influencing the excess mass loss

in the satellite, we conducted additional N-body simulations without dynamical friction. This was done to exclude potential additional effects that could contribute to the removal of mass from the satellite. The simulations were executed considering only systems characterized by the lowest initial orbital eccentricity, specifically with $v_i = 0.75v_c$, as these are the most affected by the process under investigation. The satellite under consideration featured a Hernquist mass distribution with $a_s = 0.5$. Instead of randomly oriented velocities, we initialised stars in the satellite on perfectly circular orbits, ensuring that no net rotation was imparted to the satellite as a whole.

To deal with the tendency of the velocities of the satellite stars to re-isotropize, a reorientation of the particles' velocities along the tangential direction was performed at every apocenter. Importantly, this reorientation did not alter the magnitude of the velocity vector, thus keeping the energies of the stars unchanged. This approach prevents stars on radial orbits from rapidly migrating towards larger radii, thereby restraining the overall evaporation of the satellite. This approach enables the discrimination between the processes driving the excess in satellite mass loss. If the dominant factor is satellite evaporation, this methodology allows to reproduce the satellite mass evolution. Alternatively, if tidal heating is the primary driver, injecting energy into the satellite and causing the stars to acquire sufficient energy to escape the system, our simulation will still show an excess in the mass loss.

The results are shown in Fig. 4.9. Each panel illustrates the satellite mass as a function of time for distinct orbital inclinations. The black dashed line represents the satellite mass obtained through the new N-body simulations, compared with the outcomes of the original N-body simulation presented in sec. 4.2.1, displayed as a black solid line. The colored lines depict the predictions of our semi-analytical model for various values of α.

In all systems, a substantial reduction in the mass loss rate is observed. Notably, the system harboring a satellite orbiting within the galactic plane exhibits a satellite mass evolution now compatible with our semi-analytical model, particularly for $\alpha = 0.05$. Conversely, in systems with orbits outside the galactic plane, although the reduction in satellite mass is more gradual compared to the original N-body runs, the stripped mass still exceeds that predicted by the semi-analytical models. This suggests that, at least within the galactic plane, the reorientation of star velocities is sufficient to reconcile the evolution with the semi-analytical model, indicating the dominance of satellite evaporation in shaping the mass evolution. Outside the galactic plane, however, tidal heating effects become significant and cannot be neglected.

Finally, it is important to emphasise that the fact that, in this work, tidal heating is subdominant compared to the evaporation of the satellite, occurring as a consequence of the tidal truncation, in determining the discrepancy between semi-analytical and simulation results in the satellite mass evolution, is not necessarily a universally applicable result. Indeed, repeated tidal shocks, occurring especially along elliptical orbits, could be substantially enhanced if

there were a significant central mass concentration, such as in the presence of dense bulges (see e.g., Gnedin et al., 1999) or in the case of dark matter halos with a pronounced central concentration (see e.g., van den Bosch et al., 2018). Therefore, it would be interesting to conduct future studies by extending the current model to include a dense bulge structure at the center. This would allow for the investigation of the effect of repeated tidal shocks on the satellite mass evolution and determine when this effect becomes dominant compared to tidal stripping in removing mass from the satellite.

4.3   Conclusions

We propose a novel semi-analytical framework for determining the tidal radius and relative mass evolution of satellite galaxies during minor mergers. This approach innovatively extends the definition of the tidal radius to account for various host galaxy geometries and compositions, in contrast to conventional definitions that apply only to circular orbits and assume a spherical host. Additionally, the proposed prescription incorporates a delay in mass stripping and accommodates eccentric orbits

We validated our prescription against N-body simulations, exploring the parameter space by considering different initial orbital velocities, orbital inclination, and satellite scale radii. We also perform simulations in which we account for dynamical friction.

Our model exhibited very good agreement with N-body simulations, accurately reproducing satellite mass evolution across all tested satellite scale lengths and orbital inclinations, particularly for systems with mild and high eccentric orbits. Furthermore, our model generates more realistic predictions of satellite mass evolution compared to those obtained using the King prescription for the tidal radius. However, for systems with initial velocities close to v_c, a slight systematic overestimation of satellite mass loss was observed.

Excess mass loss in systems with satellites on low-eccentricity orbits is likely influenced by two primary processes: tidal heating and satellite evaporation due to mass truncation. Additional N-body simulations were conducted to investigate this effect, in which star velocities are reoriented along the tangential direction at each apocenter.

In galactic plane orbits, reorienting star velocities reduces the excess mass loss, aligning simulations with the semi-analytical model, indicating that the satellite evaporation, coupled with the tidal stripping, dominates mass evolution. Conversely, outside the galactic plane, a gradual reduction in excess mass loss occurs, revealing significant contributions from both tidal heating and satellite evaporation to the observed discrepancies in N-body simulations and the semi-analytical model.
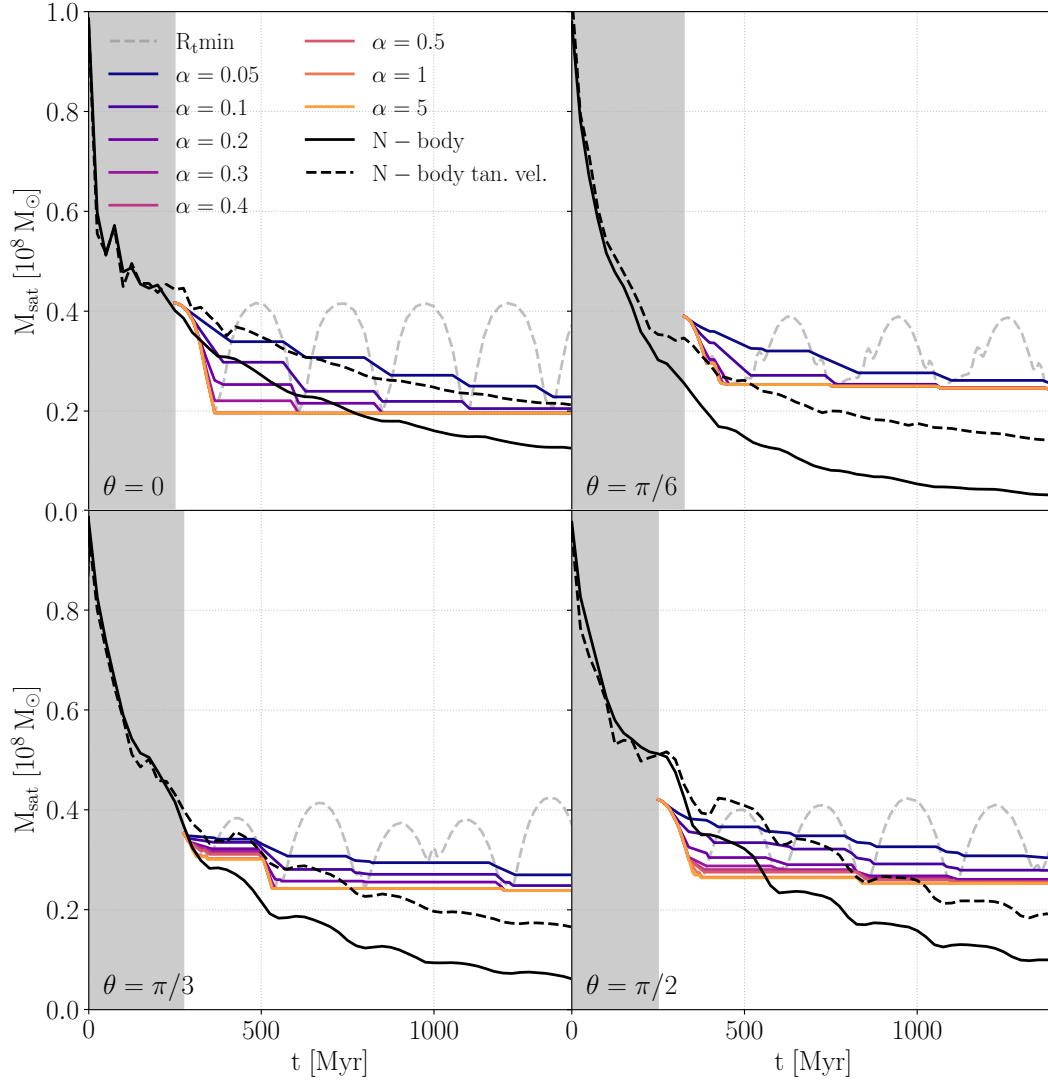
Figure 4.9: Satellite mass as a function of time for systems with the reorientation of the satellite star velocities at the apocenters. The four panels refer to different orbital inclinations, from $\theta = 0$ (leftmost panel) to $\theta = \pi/2$ (rightmost panel). The black dashed line represents the satellite mass obtained through the new N-body simulations, compared with the outcome of the original N-body simulations showed as a black solid line. The colored lines indicate the predictions of our semi-analytical model for various values of α.

<div align="right"># 5</div>

Conclusions and outlook

In this thesis, I used advanced numerical techniques to study dynamical processes related to the evolution of merging systems. On small scales, I investigated the impact of the net rotation of a galaxy hosting a SMBHB as a possible mechanism contributing to the solution of the Final Parsec Problem, according to which, in spherical system, the binary hardening driven by encounters with the stars is not efficient enough to allow the binary to reach the coalescence within an Hubble time.

On larger scales, I investigated the tidal stripping-driven mass loss experienced by a satellite galaxy when affected by tidal forces induced by a flattend host galaxy.

5.1 Impact of the host galaxy rotation on SMBHB hardening

In the first part of my work, I tested the effect of spherical rotating stellar systems onto the dynamics of forming SMBHBs. While I am perfectly aware that realistic rotating systems typically display some degree of flattening, I investigated rotating spherical systems as this allowed to isolate the effect of rotation, avoiding additional effects possibly caused by the the global torques induced by deviations from spherical symmetry[1].

I found that prograde binaries (i.e. binaries with an angular momentum aligned with the net angular momentum of the stellar core) are forced out of the centre of their host galaxies due to the interaction with their background. The CoM of prograde binaries starts moving on quasi-circular orbits around the centre of the stellar core. Such motion is considerably larger than the typical Brownian wandering experienced by SMBHBs evolving in isotropic backgrounds, and introduces a time-dependence in loss-cone of the binaries, that

---

[1]Note that Holley-Bockelmann & Khan (2015) and Khan et al. (2020) do indeed have flattened systems, but the rotation in their models is artificially introduced using our same procedure.

remains full during their whole shrinking. I demonstrated through dedicated numerical experiments that such results (the enhanced binary CoM wandering and the fast hardening rate) are not valid for retrograde binaries nor for single SMBHs: indeed the artificial merger of a wandering prograde SMBHB leads to the return of the SMBH remnant to the centre of the system, demonstrating that the physical process driving the CoM motion is the energy and angular momentum exchange between (prograde) binaries and single stars.

This investigation improves upon the previous papers presenting the circling of the binary CoM and the binary enhanced hardening evolving in rotating axi-symmetric systems (Holley-Bockelmann & Khan, 2015; Khan et al., 2020; Mirza et al., 2017) in two respects: (1) The deviations from spherical symmetry in the initial condition of such seminal investigations prevented a clear identification of the physical driver of the observed binary evolution. Indeed, in such geometries the global torques exerted by the whole stellar distribution onto single stars could play a role in the refilling of the loss-cones of the SMBHBs (but see Vasiliev et al., 2015, for a different point of view). With my simplified (spherical) stellar distribution I proved that rotation alone can cause both the SMBHB circling and the boosted hardening observed; (2) I complemented my numerical study with a phenomenological analytical model that reproduces the evolution of the binary CoM observed in the prograde runs, strengthening the proposed physical interpretation of the behaviours observed in the simulations.

A remarkable difference between my results and those obtained by Holley-Bockelmann & Khan (2015) regards the hardening rates of retrograde binaries. In the rotating-spherical scenario I find that retrograde binaries shrink at a significantly slower pace than their prograde counterparts, while such difference is not observed in the rotating-flattened scenario discussed by Holley-Bockelmann and collaborators. In my analytical model the different behaviours are due to the absence of any binary CoM motion larger than the Brownian motion typically observed in isotropic systems, that prevent any significant collisionless loss-cone refilling associated to the motion of the binary CoM. The disagreement with the findings of Holley-Bockelmann & Khan (2015) could, in principle, be due to the different geometries of the stellar distributions, motivating further modeling of axi-symmetric systems.

My analytical model and numerical experiments agree on the fact that SMBHBs experience the most external angular momentum growth right after their formation, at large semi-major axes. This implies that binaries forming with their internal angular momentum significantly offset from that of the surrounding environment would neither experience the CoM circling nor the enhanced hardening[2], as they would have shrunk their semi-major axis significantly before getting aligned with the environmental angular momentum. It is however possible that, in systems with a significant amount of rotation at large scales, the internal angular momentum of the forming binaries is al-

---

[2]But see the discussion above about the comparison with Holley-Bockelmann & Khan (2015).

ready aligned with the angular momentum of the surrounding environment. Such configurations are expected even for initially strongly misaligned galaxy mergers, as (1) at large scale dynamical friction onto rotating systems would act on the massive bodies dragging them towards a prograde, circular orbit (e.g. Bonetti et al., 2021a, 2020a; Dotti et al., 2006), and (2) the same process can take place even at smaller scales immediately before the binary formation (Gualandris et al., 2012b; Khan et al., 2020; Mirza et al., 2017; Sesana et al., 2011).

Outlook

The relevance of the background rotation for the evolution of SMBHBs depends ultimately on the typical dynamical properties of their hosts. For light host galaxies hosting light SMBHs $10^5 - 10^7 M_\odot$, in the mass range detectable by the forthcoming LISA mission, clear rotation is commonly observed at low redshift both at galactic and sub-kpc scales (e.g. Kormendy, 2013). It is yet unclear for which mass ratios and up to which redshift the same rotationally dominated structures are expected in galaxy mergers. Dedicated observational studies and detailed analyses of cosmologically motivated galaxy merger simulations are needed to properly gauge the impact of the presented results on the whole population of SMBHBs.

Ideed, in lighter, often disc-dominated, galaxies the central regions are typically dominated by secular bulges, as boxy-peanut bulges (usually interpreted as the evolution of the central region of a bar) or discy pseudobulges (flat structures supposedly formed as a consequence of secular gas inflows). Both structures present clear deviations from spherical symmetry and substantial net rotation (see e.g. Kormendy, 2013; Sellwood & Wilkinson, 1993) and, therefore, are not properly modelled by our simplistic assumptions. It should be stressed, however, that typical observations of galactic nuclei are limited by the angular resolution of the instrument used, and that the redshift of galaxy merger most relevant for LISA is expected to be large (> 1), so that the $\sim$ pc surroundings of the binary is typically not resolved. The analysis of nearby galaxies (including our own Milky way, that present a clear rotation in its innermost pc (Ghez et al., 2008) or of very high resolution (zoom-in) cosmological simulations could shed further light on the innermost dynamics of small mass systems.

5.2   Tidal stripping in minor mergers

In the second part of the present work, I focused on minor galaxy mergers, specifically investigating the mass loss experienced by the satellite galaxy due to tidal stripping while merging with a disc-like primary galaxy.

In this context, we propose a new semi-analytical prescription for the tidal radius and the relative mass evolution of satellite galaxies in minor mergers. The novelty of the proposed approach primarily lies in the generalization of the

definition of the tidal radius to be adaptable for any geometry and composition of the host galaxy. This is in contrast to traditional definition of the tidal radius (King, 1962) provided for circular orbits and spherical hosts. The prescription also accounts for a delay in mass stripping and allows for eccentric orbits.

I validated my prescription against N-body simulations. In order to isolate the effects of tidal forces, I firstly consider systems unaffected by dynamical friction, by considering systems composed of a spherically symmetric satellite orbiting within the analytical potential of an exponential-disk host. I explored the parameter space by considering different initial orbital velocities, orbital inclination, and satellite scale radii.

For each tested system, I select the semi-analytical model characterized by the α parameter - which regulates the rapidity of mass loss in my semi-analytical model, with higher values related to faster mass loss- that better reproduces the mass evolution of the satellite in N-body simulations. I found a mild dependence of the best α with the initial orbital velocity, while no significant dependencies are notable with the satellite scale radius and orbital inclination. Lower values of α were associated with more eccentric orbits, reflecting the need for a larger delay in mass loss due to faster pericenter passages.

The proposed model model demonstrated excellent agreement with N-body simulations, accurately reproducing satellite mass evolution, especially for systems with mild and high eccentric orbits. However, for systems with initial velocities close to v_c, a slight systematic overestimation of satellite mass loss was observed. This excess is likely due to two primary processes: tidal heating and satellite evaporation induced by mass truncation. To delve into this discrepancy, additional N-body simulations were conducted, where at each apocenter I reorient star velocities along the tangential direction.

In systems where the satellite orbits within the galactic plane, the reorientation of star velocities mitigates the excess mass loss, aligning the simulation results with the predictions of the semi-analytical model. This suggests that, within the galactic plane, together with tidal stripping, satellite evaporation plays a dominant role in shaping the mass evolution.

However, outside the galactic plane, the reduction in excess mass loss is more gradual, as tidal heating effects become significant. This indicates that, in these configurations, both tidal heating and satellite evaporation contribute to the observed discrepancies between N-body simulations and the semi-analytical model.

Moreover, for orbits within the galactic plane, I compared the semi-analytical prescription for the satellite mass evolution with the instantaneous mass loss predicted using the King's formula in reproducing the results of N-body simulations. I found that the proposed model better reproduces the mass evolution in the simulations. I stress that outside the galactic plane - and in general in every non central potential- the King's tidal radius is not well defined.

To further test the validity of the proposed model and conduct a direct

comparison of its ability to reproduce the results of N-body simulations with those obtained using the standard King's formula, I performed a set of simulations where the satellite galaxy orbits within a spherically symmetric host. I tested the same initial orbital velocities and scale radii lengths as in the case of a disc host. I found that, also in the case of a spherical host, my model better reproduces the results of simulations. Interestingly, the predictions of my model converge to those of the King's formula for lower initial velocities. This further confirms the robustness of my model since the scenario of a satellite orbiting within a spherical host on quasi-circular orbits best matches the assumption underlying the King's formula, thus representing the situation in which the King's formula is expected to be more reliable.

I then consider systems with both tidal stripping and dynamical friction effects. The semi-analytical model accurately reproduces both the orbital evolution and mass loss of the satellite.

These findings provide valuable insights into the complex interplay of tidal forces, dynamical friction, and the orbital parameters of satellite galaxies. Understanding these processes is crucial for accurately modelling the evolution of satellite galaxies within their host galactic environments.

Outlook

The model developed thus far for the mass evolution of a satellite galaxy in a minor merger incorporates the influences of a slowly varying external tidal field. However, as demonstrated by my simulations, tidal heating can play a substantial role in eroding the satellite's mass, particularly when the external potential experienced by the satellite changes rapidly over time. To address the evolution of the mass of satellite galaxies in minor mergers more comprehensively, I am planning to incorporate a detailed prescription for mass loss due to tidal heating effects into my existing model. While, efficient prescriptions for tidal shockings in sperically symmetric host are available in literature, as the one proposed by Gnedin et al. (1999), the situation differs for disk-shaped host galaxies. Indeed, when the primary galaxy is a disk and the smaller companion galaxy orbits out of the galactic plane, tidal shocks manifest as repeated pinchings of the satellite along the normal direction with respect to the disk plane, each pinching occurring during orbital crossing with the galactic plane. This specific kind of tidal shocking are often referred to as disk shocking. In this case, the prescription proposed in literature for estimating the energy gain of the satellite stars determining the amount of material which will be consequently unbound, is made under the simplistic distant tide approximation (see e.g. Binney & Tremaine, 2008). For this reason, while for spherical hosts I am planning to implement in my model the standard treatment for the tidal-heating-driven energy gain and mass loss, I would develope a more general prescription in the case of disk shocking, which also account for close encounters.

In a broader context, galaxies experience morphological evolution through-

out cosmic time due to secular evolution. This evolutionary process may result from interactions between the galaxy and its environment, such as gas accretion or galaxy harassment, or it can be initiated by internal factors such as the presence of spiral arms or bars. In this context, I am currently working on a prescription for the cosmological evolution of the primary galaxy during the pairing phase. For this purpose, I integrated into the MORDOR code (Zana et al., 2022) the computation of half-mass radii for each galactic component, including the bulge, pseudo-bulge, thin and thick discs, and a dark matter halo. I am employing this modified version of MORDOR on Illustris TNG50 snapshots (Nelson et al., 2019) to reconstruct and characterize the evolution of each galaxy component over cosmic time. Through this analysis, it will be possible to construct a semi-analytical model for the cosmological evolution of the entire galaxy to study how the cosmological evolution of the primary galaxy affects the dynamics of minor mergers.

Possible applications

Once the comprehensive model for the evolution of satellite mass under the influence of tidal forces exerted by the host galaxy is completed, including the tidal heating effects, and properly validated, the next step would be to implement it in a semi-analytical code. Among the various options available, L-Galaxies stands out as a particularly suitable choice. Originally developed in the 1990s by White (1989), White & Frenk (1991), and Kauffmann et al. (1999, 1993), L-Galaxies is a C++ based semi-analytic simulation operating at cosmological scales. It simulates the evolution of galaxies using "merger trees" derived from N-body simulations of hierarchical structure formation in dark matter halos. The semi-analytic approach of L-Galaxies facilitates efficient modelling of millions of galaxies from the early Universe to the present day, surpassing the computational efficiency of hydrodynamical simulations of similar scale. This capability makes L-Galaxies well-suited for validating astrophysical models and conducting statistical analyses on significant galaxy samples. These analyses include investigations into various properties of galaxies and the supermassive black holes they host. Implementing my new model for the tidal disruption of satellite galaxies within L-Galaxies, could significantly enhance the predictive power of semi-analytic simulations, particularly in the context of minor mergers.

Another promising application of my semi-analytical model consists in augmenting large scale cosmological simulations, such as the Illustris TNG (Nelson et al., 2018). In these simulations, numerous minor mergers are observed to occur, however their resolution may become inadequate to track the late stages of these events as the satellite galaxies become unresolved. By utilizing data on the properties of the satellite and host galaxy mass distributions, along with the satellite's position and velocity as initial conditions for my semi-analytical model, it would be possible to predict the later phases of the merger and determine the ultimate fate of the satellite and if present, of the MBH embedded

within it.

Bibliography

Aarseth, S. J. (1963). Dynamical evolution of clusters of galaxies, I. , *126*, 223.

Aarseth, S. J. (2003). *Gravitational N-Body Simulations*.

Abbott, B. P., Abbott, R., Abbott, T. D., Abernathy, M. R., Acernese, F., Ackley, K., Adams, C., Adams, T., Addesso, P., Adhikari, R. X., Adya, V. B., Affeldt, C., Agathos, M., Agatsuma, K., Aggarwal, N., Aguiar, O. D., Aiello, L., Ain, A., Ajith, P., Allen, B., Allocca, A., Altin, P. A., Anderson, S. B., Anderson, W. G., Arai, K., Arain, M. A., Araya, M. C., Arceneaux, C. C., Areeda, J. S., Arnaud, N., Arun, K. G., Ascenzi, S., Ashton, G., Ast, M., Aston, S. M., Astone, P., Aufmuth, P., Aulbert, C., Babak, S., Bacon, P., Bader, M. K. M., Baker, P. T., Baldaccini, F., Ballardin, G., Ballmer, S. W., Barayoga, J. C., Barclay, S. E., Barish, B. C., Barker, D., Barone, F., Barr, B., Barsotti, L., Barsuglia, M., Barta, D., Bartlett, J., Barton, M. A., Bartos, I., Bassiri, R., Basti, A., Batch, J. C., Baune, C., Bavigadda, V., Bazzan, M., Behnke, B., Bejger, M., Belczynski, C., Bell, A. S., Bell, C. J., Berger, B. K., Bergman, J., Bergmann, G., Berry, C. P. L., Bersanetti, D., Bertolini, A., Betzwieser, J., Bhagwat, S., Bhandare, R., Bilenko, I. A., Billingsley, G., Birch, J., Birney, R., Birnholtz, O., Biscans, S., Bisht, A., Bitossi, M., Biwer, C., Bizouard, M. A., Blackburn, J. K., Blair, C. D., Blair, D. G., Blair, R. M., Bloemen, S., Bock, O., Bodiya, T. P., Boer, M., Bogaert, G., Bogan, C., Bohe, A., Bojtos, P., Bond, C., Bondu, F., Bonnand, R., Boom, B. A., Bork, R., Boschi, V., Bose, S., Bouffanais, Y., Bozzi, A., Bradaschia, C., Brady, P. R., Braginsky, V. B., Branchesi, M., Brau, J. E., Briant, T., Brillet, A., Brinkmann, M., Brisson, V., Brockill, P., Brooks, A. F., Brown, D. A., Brown, D. D., Brown, N. M., Buchanan, C. C., Buikema, A., Bulik, T., Bulten, H. J., Buonanno, A., Buskulic, D., Buy, C., Byer, R. L., Cabero, M., Cadonati, L., Cagnoli, G., Cahillane, C., Bustillo, J. C., Callister, T., Calloni, E., Camp, J. B., Cannon, K. C., Cao, J., Capano, C. D., Capocasa, E., Carbognani, F., Caride, S., Casanueva Diaz, J., Casentini, C., Caudill, S., Cavaglià, M., Cavalier, F., Cavalieri, R., Cella, G., Cepeda, C. B., Baiardi, L. C., Cerretani, G., Cesarini, E., Chakraborty, R., Chalermsongsak, T., Chamberlin, S. J., Chan, M., Chao, S., Charlton, P., Chassande-Mottin, E., Chen, H. Y., Chen, Y., Cheng, C., Chincarini, A., Chiummo, A., Cho, H. S., Cho, M., Chow, J. H., Christensen, N., Chu, Q., Chua, S., Chung, S., Ciani, G., Clara, F., Clark, J. A., Cleva, F., Coccia,

E., Cohadon, P. F., Colla, A., Collette, C. G., Cominsky, L., Constancio, M., Conte, A., Conti, L., Cook, D., Corbitt, T. R., Cornish, N., Corsi, A., Cortese, S., Costa, C. A., Coughlin, M. W., Coughlin, S. B., Coulon, J. P., Countryman, S. T., Couvares, P., Cowan, E. E., Coward, D. M., Cowart, M. J., Coyne, D. C., Coyne, R., Craig, K., Creighton, J. D. E., Creighton, T. D., Cripe, J., Crowder, S. G., Cruise, A. M., Cumming, A., Cunningham, L., Cuoco, E., Dal Canton, T., Danilishin, S. L., D'Antonio, S., Danzmann, K., Darman, N. S., Da Silva Costa, C. F., Dattilo, V., Dave, I., Daveloza, H. P., Davier, M., Davies, G. S., Daw, E. J., Day, R., De, S., DeBra, D., Debreczeni, G., Degallaix, J., De Laurentis, M., Deléglise, S., Del Pozzo, W., Denker, T., Dent, T., Dereli, H., Dergachev, V., DeRosa, R. T., De Rosa, R., DeSalvo, R., Dhurandhar, S., Díaz, M. C., Di Fiore, L., Di Giovanni, M., Di Lieto, A., Di Pace, S., Di Palma, I., Di Virgilio, A., Dojcinoski, G., Dolique, V., Donovan, F., Dooley, K. L., Doravari, S., Douglas, R., Downes, T. P., Drago, M., Drever, R. W. P., Driggers, J. C., Du, Z., Ducrot, M., Dwyer, S. E., Edo, T. B., Edwards, M. C., Effler, A., Eggenstein, H. B., Ehrens, P., Eichholz, J., Eikenberry, S. S., Engels, W., Essick, R. C., Etzel, T., Evans, M., Evans, T. M., Everett, R., Factourovich, M., Fafone, V., Fair, H., Fairhurst, S., Fan, X., Fang, Q., Farinon, S., Farr, B., Farr, W. M., Favata, M., Fays, M., Fehrmann, H., Fejer, M. M., Feldbaum, D., Ferrante, I., Ferreira, E. C., Ferrini, F., Fidecaro, F., Finn, L. S., Fiori, I., Fiorucci, D., Fisher, R. P., Flaminio, R., Fletcher, M., Fong, H., Fournier, J. D., Franco, S., Frasca, S., Frasconi, F., Frede, M., Frei, Z., Freise, A., Frey, R., Frey, V., Fricke, T. T., Fritschel, P., Frolov, V. V., Fulda, P., Fyffe, M., Gabbard, H. A. G., Gair, J. R., Gammaitoni, L., Gaonkar, S. G., Garufi, F., Gatto, A., Gaur, G., Gehrels, N., Gemme, G., Gendre, B., Genin, E., Gennai, A., George, J., Gergely, L., Germain, V., Ghosh, A., Ghosh, A., Ghosh, S., Giaime, J. A., Giardina, K. D., Giazotto, A., Gill, K., Glaefke, A., Gleason, J. R., Goetz, E., Goetz, R., Gondan, L., González, G., Castro, J. M. G., Gopakumar, A., Gordon, N. A., Gorodetsky, M. L., Gossan, S. E., Gosselin, M., Gouaty, R., Graef, C., Graff, P. B., Granata, M., Grant, A., Gras, S., Gray, C., Greco, G., Green, A. C., Greenhalgh, R. J. S., Groot, P., Grote, H., Grunewald, S., Guidi, G. M., Guo, X., Gupta, A., Gupta, M. K., Gushwa, K. E., Gustafson, E. K., Gustafson, R., Hacker, J. J., Hall, B. R., Hall, E. D., Hammond, G., Haney, M., Hanke, M. M., Hanks, J., Hanna, C., Hannam, M. D., Hanson, J., Hardwick, T., Harms, J., Harry, G. M., Harry, I. W., Hart, M. J., Hartman, M. T., Haster, C. J., Haughian, K., Healy, J., Heefner, J., Heidmann, A., Heintze, M. C., Heinzel, G., Heitmann, H., Hello, P., Hemming, G., Hendry, M., Heng, I. S., Hennig, J., Heptonstall, A. W., Heurs, M., Hild, S., Hoak, D., Hodge, K. A., Hofman, D., Hollitt, S. E., Holt, K., Holz, D. E., Hopkins, P., Hosken, D. J., Hough, J., Houston, E. A., Howell, E. J., Hu, Y. M., Huang, S., Huerta, E. A., Huet, D., Hughey, B., Husa, S., Huttner, S. H., Huynh-Dinh, T., Idrisy, A., Indik, N., Ingram, D. R., Inta, R., Isa, H. N., Isac, J. M., Isi,

M., Islas, G., Isogai, T., Iyer, B. R., Izumi, K., Jacobson, M. B., Jacqmin, T., Jang, H., Jani, K., Jaranowski, P., Jawahar, S., Jiménez-Forteza, F., Johnson, W. W., Johnson-McDaniel, N. K., Jones, D. I., Jones, R., Jonker, R. J. G., Ju, L., Haris, K., Kalaghatgi, C. V., Kalogera, V., Kandhasamy, S., Kang, G., Kanner, J. B., Karki, S., Kasprzack, M., Katsavounidis, E., Katzman, W., Kaufer, S., Kaur, T., Kawabe, K., Kawazoe, F., Kéfélian, F., Kehl, M. S., Keitel, D., Kelley, D. B., Kells, W., Kennedy, R., Keppel, D. G., Key, J. S., Khalaidovski, A., Khalili, F. Y., Khan, I., Khan, S., Khan, Z., Khazanov, E. A., Kijbunchoo, N., Kim, C., Kim, J., Kim, K., Kim, N.-G., Kim, N., Kim, Y. M., King, E. J., King, P. J., Kinzel, D. L., Kissel, J. S., Kleybolte, L., Klimenko, S., Koehlenbeck, S. M., Kokeyama, K., Koley, S., Kondrashov, V., Kontos, A., Koranda, S., Korobko, M., Korth, W. Z., Kowalska, I., Kozak, D. B., Kringel, V., Krishnan, B., Królak, A., Krueger, C., Kuehn, G., Kumar, P., Kumar, R., Kuo, L., Kutynia, A., Kwee, P., Lackey, B. D., Landry, M., Lange, J., Lantz, B., Lasky, P. D., Lazzarini, A., Lazzaro, C., Leaci, P., Leavey, S., Lebigot, E. O., Lee, C. H., Lee, H. K., Lee, H. M., Lee, K., Lenon, A., Leonardi, M., Leong, J. R., Leroy, N., Letendre, N., Levin, Y., Levine, B. M., Li, T. G. F., Libson, A., Littenberg, T. B., Lockerbie, N. A., Logue, J., Lombardi, A. L., London, L. T., Lord, J. E., Lorenzini, M., Loriette, V., Lormand, M., Losurdo, G., Lough, J. D., Lousto, C. O., Lovelace, G., Lück, H., Lundgren, A. P., Luo, J., Lynch, R., Ma, Y., MacDonald, T., Machenschalk, B., MacInnis, M., Macleod, D. M., Magaña-Sandoval, F., Magee, R. M., Mageswaran, M., Majorana, E., Maksimovic, I., Malvezzi, V., Man, N., Mandel, I., Mandic, V., Mangano, V., Mansell, G. L., Manske, M., Mantovani, M., Marchesoni, F., Marion, F., Márka, S., Márka, Z., Markosyan, A. S., Maros, E., Martelli, F., Martellini, L., Martin, I. W., Martin, R. M., Martynov, D. V., Marx, J. N., Mason, K., Masserot, A., Massinger, T. J., Masso-Reid, M., Matichard, F., Matone, L., Mavalvala, N., Mazumder, N., Mazzolo, G., McCarthy, R., McClelland, D. E., McCormick, S., McGuire, S. C., McIntyre, G., McIver, J., McManus, D. J., McWilliams, S. T., Meacher, D., Meadors, G. D., Meidam, J., Melatos, A., Mendell, G., Mendoza-Gandara, D., Mercer, R. A., Merilh, E., Merzougui, M., Meshkov, S., Messenger, C., Messick, C., Meyers, P. M., Mezzani, F., Miao, H., Michel, C., Middleton, H., Mikhailov, E. E., Milano, L., Miller, J., Millhouse, M., Minenkov, Y., Ming, J., Mirshekari, S., Mishra, C., Mitra, S., Mitrofanov, V. P., Mitselmakher, G., Mittleman, R., Moggi, A., Mohan, M., Mohapatra, S. R. P., Montani, M., Moore, B. C., Moore, C. J., Moraru, D., Moreno, G., Morriss, S. R., Mossavi, K., Mours, B., Mow-Lowry, C. M., Mueller, C. L., Mueller, G., Muir, A. W., Mukherjee, A., Mukherjee, D., Mukherjee, S., Mukund, N., Mullavey, A., Munch, J., Murphy, D. J., Murray, P. G., Mytidis, A., Nardecchia, I., Naticchioni, L., Nayak, R. K., Necula, V., Nedkova, K., Nelemans, G., Neri, M., Neunzert, A., Newton, G., Nguyen, T. T., Nielsen, A. B., Nissanke, S., Nitz, A., Nocera, F., Nolting, D., Normandin, M. E. N., Nuttall, L. K., Oberling, J., Ochsner, E., O'Dell, J., Oelker, E.,

Ogin, G. H., Oh, J. J., Oh, S. H., Ohme, F., Oliver, M., Oppermann, P., Oram, R. J., O'Reilly, B., O'Shaughnessy, R., Ott, C. D., Ottaway, D. J., Ottens, R. S., Overmier, H., Owen, B. J., Pai, A., Pai, S. A., Palamos, J. R., Palashov, O., Palomba, C., Pal-Singh, A., Pan, H., Pan, Y., Pankow, C., Pannarale, F., Pant, B. C., Paoletti, F., Paoli, A., Papa, M. A., Paris, H. R., Parker, W., Pascucci, D., Pasqualetti, A., Passaquieti, R., Passuello, D., Patricelli, B., Patrick, Z., Pearlstone, B. L., Pedraza, M., Pedurand, R., Pekowsky, L., Pele, A., Penn, S., Perreca, A., Pfeiffer, H. P., Phelps, M., Piccinni, O., Pichot, M., Pickenpack, M., Piergiovanni, F., Pierro, V., Pillant, G., Pinard, L., Pinto, I. M., Pitkin, M., Poeld, J. H., Poggiani, R., Popolizio, P., Post, A., Powell, J., Prasad, J., Predoi, V., Premachandra, S. S., Prestegard, T., Price, L. R., Prijatelj, M., Principe, M., Privitera, S., Prix, R., Prodi, G. A., Prokhorov, L., Puncken, O., Punturo, M., Puppo, P., Pürrer, M., Qi, H., Qin, J., Quetschke, V., Quintero, E. A., Quitzow-James, R., Raab, F. J., Rabeling, D. S., Radkins, H., Raffai, P., Raja, S., Rakhmanov, M., Ramet, C. R., Rapagnani, P., Raymond, V., Razzano, M., Re, V., Read, J., Reed, C. M., Regimbau, T., Rei, L., Reid, S., Reitze, D. H., Rew, H., Reyes, S. D., Ricci, F., Riles, K., Robertson, N. A., Robie, R., Robinet, F., Rocchi, A., Rolland, L., Rollins, J. G., Roma, V. J., Romano, J. D., Romano, R., Romanov, G., Romie, J. H., Rosińska, D., Rowan, S., Rüdiger, A., Ruggi, P., Ryan, K., Sachdev, S., Sadecki, T., Sadeghian, L., Salconi, L., Saleem, M., Salemi, F., Samajdar, A., Sammut, L., Sampson, L. M., Sanchez, E. J., Sandberg, V., Sandeen, B., Sanders, G. H., Sanders, J. R., Sassolas, B., Sathyaprakash, B. S., Saulson, P. R., Sauter, O., Savage, R. L., Sawadsky, A., Schale, P., Schilling, R., Schmidt, J., Schmidt, P., Schnabel, R., Schofield, R. M. S., Schönbeck, A., Schreiber, E., Schuette, D., Schutz, B. F., Scott, J., Scott, S. M., Sellers, D., Sengupta, A. S., Sentenac, D., Sequino, V., Sergeev, A., Serna, G., Setyawati, Y., Sevigny, A., Shaddock, D. A., Shaffer, T., Shah, S., Shahriar, M. S., Shaltev, M., Shao, Z., Shapiro, B., Shawhan, P., Sheperd, A., Shoemaker, D. H., Shoemaker, D. M., Siellez, K., Siemens, X., Sigg, D., Silva, A. D., Simakov, D., Singer, A., Singer, L. P., Singh, A., Singh, R., Singhal, A., Sintes, A. M., Slagmolen, B. J. J., Smith, J. R., Smith, M. R., Smith, N. D., Smith, R. J. E., Son, E. J., Sorazu, B., Sorrentino, F., Souradeep, T., Srivastava, A. K., Staley, A., Steinke, M., Steinlechner, J., Steinlechner, S., Steinmeyer, D., Stephens, B. C., Stevenson, S. P., Stone, R., Strain, K. A., Straniero, N., Stratta, G., Strauss, N. A., Strigin, S., Sturani, R., Stuver, A. L., Summerscales, T. Z., Sun, L., Sutton, P. J., Swinkels, B. L., Szczepańczyk, M. J., Tacca, M., Talukder, D., Tanner, D. B., Tápai, M., Tarabrin, S. P., Taracchini, A., Taylor, R., Theeg, T., Thirugnanasambandam, M. P., Thomas, E. G., Thomas, M., Thomas, P., Thorne, K. A., Thorne, K. S., Thrane, E., Tiwari, S., Tiwari, V., Tokmakov, K. V., Tomlinson, C., Tonelli, M., Torres, C. V., Torrie, C. I., Töyrä, D., Travasso, F., Traylor, G., Trifirò, D., Tringali, M. C., Trozzo, L., Tse, M., Turconi, M., Tuyenbayev, D., Ugolini, D., Unnikrishnan, C. S., Urban, A. L.,

Usman, S. A., Vahlbruch, H., Vajente, G., Valdes, G., Vallisneri, M., van Bakel, N., van Beuzekom, M., van den Brand, J. F. J., Van Den Broeck, C., Vander-Hyde, D. C., van der Schaaf, L., van Heijningen, J. V., van Veggel, A. A., Vardaro, M., Vass, S., Vasúth, M., Vaulin, R., Vecchio, A., Vedovato, G., Veitch, J., Veitch, P. J., Venkateswara, K., Verkindt, D., Vetrano, F., Viceré, A., Vinciguerra, S., Vine, D. J., Vinet, J. Y., Vitale, S., Vo, T., Vocca, H., Vorvick, C., Voss, D., Vousden, W. D., Vyatchanin, S. P., Wade, A. R., Wade, L. E., Wade, M., Waldman, S. J., Walker, M., Wallace, L., Walsh, S., Wang, G., Wang, H., Wang, M., Wang, X., Wang, Y., Ward, H., Ward, R. L., Warner, J., Was, M., Weaver, B., Wei, L. W., Weinert, M., Weinstein, A. J., Weiss, R., Welborn, T., Wen, L., Weßels, P., West-phal, T., Wette, K., Whelan, J. T., Whitcomb, S. E., White, D. J., Whiting, B. F., Wiesner, K., Wilkinson, C., Willems, P. A., Williams, L., Williams, R. D., Williamson, A. R., Willis, J. L., Willke, B., Wimmer, M. H., Winkel-mann, L., Winkler, W., Wipf, C. C., Wiseman, A. G., Wittel, H., Woan, G., Worden, J., Wright, J. L., Wu, G., Yablon, J., Yakushin, I., Yam, W., Yamamoto, H., Yancey, C. C., Yap, M. J., Yu, H., Yvert, M., ZadroŻny, A., Zangrando, L., Zanolin, M., Zendri, J. P., Zevin, M., Zhang, F., Zhang, L., Zhang, M., Zhang, Y., Zhao, C., Zhou, M., Zhou, Z., Zhu, X. J., Zucker, M. E., Zuraw, S. E., Zweizig, J., LIGO Scientific Collaboration, & Virgo Collaboration (2016). Observation of Gravitational Waves from a Binary Black Hole Merger. , *116*(6), 061102.

Agazie, G., Anumarlapudi, A., Archibald, A. M., Arzoumanian, Z., Baker, P. T., Bécsy, B., Blecha, L., Brazier, A., Brook, P. R., Burke-Spolaor, S., Burnette, R., Case, R., Charisi, M., Chatterjee, S., Chatziioannou, K., Cheeseboro, B. D., Chen, S., Cohen, T., Cordes, J. M., Cornish, N. J., Craw-ford, F., Cromartie, H. T., Crowter, K., Cutler, C. J., Decesar, M. E., Degan, D., Demorest, P. B., Deng, H., Dolch, T., Drachler, B., Ellis, J. A., Ferrara, E. C., Fiore, W., Fonseca, E., Freedman, G. E., Garver-Daniels, N., Gentile, P. A., Gersbach, K. A., Glaser, J., Good, D. C., Gültekin, K., Hazboun, J. S., Hourihane, S., Islo, K., Jennings, R. J., Johnson, A. D., Jones, M. L., Kaiser, A. R., Kaplan, D. L., Kelley, L. Z., Kerr, M., Key, J. S., Klein, T. C., Laal, N., Lam, M. T., Lamb, W. G., Lazio, T. J. W., Lewandowska, N., Lit-tenberg, T. B., Liu, T., Lommen, A., Lorimer, D. R., Luo, J., Lynch, R. S., Ma, C.-P., Madison, D. R., Mattson, M. A., McEwen, A., McKee, J. W., McLaughlin, M. A., McMann, N., Meyers, B. W., Meyers, P. M., Mingarelli, C. M. F., Mitridate, A., Natarajan, P., Ng, C., Nice, D. J., Ocker, S. K., Olum, K. D., Pennucci, T. T., Perera, B. B. P., Petrov, P., Pol, N. S., Radovan, H. A., Ransom, S. M., Ray, P. S., Romano, J. D., Sardesai, S. C., Schmiedekamp, A., Schmiedekamp, C., Schmitz, K., Schult, L., Shapiro-Albert, B. J., Siemens, X., Simon, J., Siwek, M. S., Stairs, I. H., Stinebring, D. R., Stovall, K., Sun, J. P., Susobhanan, A., Swiggum, J. K., Taylor, J., Taylor, S. R., Turner, J. E., Unal, C., Vallisneri, M., van Haasteren, R., Vigeland, S. J., Wahl, H. M., Wang, Q., Witt, C. A., Young, O., &

Nanograv Collaboration (2023). The NANOGrav 15 yr Data Set: Evidence for a Gravitational-wave Background. , *951*(1), L8.

Amaro-Seoane, P., Andrews, J., Arca Sedda, M., Askar, A., Baghi, Q., Balasov, R., Bartos, I., Bavera, S. S., Bellovary, J., Berry, C. P. L., Berti, E., Bianchi, S., Blecha, L., Blondin, S., Bogdanović, T., Boissier, S., Bonetti, M., Bonoli, S., Bortolas, E., Breivik, K., Capelo, P. R., Caramete, L., Cattorini, F., Charisi, M., Chaty, S., Chen, X., Chruślińska, M., Chua, A. J. K., Church, R., Colpi, M., D'Orazio, D., Danielski, C., Davies, M. B., Dayal, P., De Rosa, A., Derdzinski, A., Destounis, K., Dotti, M., Dutan, I., Dvorkin, I., Fabj, G., Foglizzo, T., Ford, S., Fouvry, J.-B., Franchini, A., Fragos, T., Fryer, C., Gaspari, M., Gerosa, D., Graziani, L., Groot, P., Habouzit, M., Haggard, D., Haiman, Z., Han, W.-B., Istrate, A., Johansson, P. H., Khan, F. M., Kimpson, T., Kokkotas, K., Kong, A., Korol, V., Kremer, K., Kupfer, T., Lamberts, A., Larson, S., Lau, M., Liu, D., Lloyd-Ronning, N., Lodato, G., Lupi, A., Ma, C.-P., Maccarone, T., Mandel, I., Mangiagli, A., Mapelli, M., Mathis, S., Mayer, L., McGee, S., McKernan, B., Miller, M. C., Mota, D. F., Mumpower, M., Nasim, S. S., Nelemans, G., Noble, S., Pacucci, F., Panessa, F., Paschalidis, V., Pfister, H., Porquet, D., Quenby, J., Ricarte, A., Röpke, F. K., Regan, J., Rosswog, S., Ruiter, A., Ruiz, M., Runnoe, J., Schneider, R., Schnittman, J., Secunda, A., Sesana, A., Seto, N., Shao, L., Shapiro, S., Sopuerta, C., Stone, N. C., Suvorov, A., Tamanini, N., Tamfal, T., Tauris, T., Temmink, K., Tomsick, J., Toonen, S., Torres-Orjuela, A., Toscani, M., Tsokaros, A., Unal, C., Vázquez-Aceves, V., Valiante, R., van Putten, M., van Roestel, J., Vignali, C., Volonteri, M., Wu, K., Younsi, Z., Yu, S., Zane, S., Zwick, L., Antonini, F., Baibhav, V., Barausse, E., Bonilla Rivera, A., Branchesi, M., Branduardi-Raymont, G., Burdge, K., Chakraborty, S., Cuadra, J., Dage, K., Davis, B., de Mink, S. E., Decarli, R., Doneva, D., Escoffier, S., Gandhi, P., Haardt, F., Lousto, C. O., Nissanke, S., Nordhaus, J., O'Shaughnessy, R., Portegies Zwart, S., Pound, A., Schussler, F., Sergijenko, O., Spallicci, A., Vernieri, D., & Vigna-Gómez, A. (2023). Astrophysics with the Laser Interferometer Space Antenna. *Living Reviews in Relativity*, *26*(1), 2.

Amaro-Seoane, P., Audley, H., Babak, S., Baker, J., Barausse, E., Bender, P., Berti, E., Binetruy, P., Born, M., Bortoluzzi, D., Camp, J., Caprini, C., Cardoso, V., Colpi, M., Conklin, J., Cornish, N., Cutler, C., Danzmann, K., Dolesi, R., Ferraioli, L., Ferroni, V., Fitzsimons, E., Gair, J., Gesa Bote, L., Giardini, D., Gibert, F., Grimani, C., Halloin, H., Heinzel, G., Hertog, T., Hewitson, M., Holley-Bockelmann, K., Hollington, D., Hueller, M., Inchauspe, H., Jetzer, P., Karnesis, N., Killow, C., Klein, A., Klipstein, B., Korsakova, N., Larson, S. L., Livas, J., Lloro, I., Man, N., Mance, D., Martino, J., Mateos, I., McKenzie, K., McWilliams, S. T., Miller, C., Mueller, G., Nardini, G., Nelemans, G., Nofrarias, M., Petiteau, A., Pivato, P., Plagnol, E., Porter, E., Reiche, J., Robertson, D., Robertson, N., Rossi, E., Russano,

G., Schutz, B., Sesana, A., Shoemaker, D., Slutsky, J., Sopuerta, C. F., Sumner, T., Tamanini, N., Thorpe, I., Troebs, M., Vallisneri, M., Vecchio, A., Vetrugno, D., Vitale, S., Volonteri, M., Wanner, G., Ward, H., Wass, P., Weber, W., Ziemer, J., & Zweifel, P. (2017). Laser Interferometer Space Antenna. *arXiv e-prints*, (p. arXiv:1702.00786).

Antoniadis, J., Arumugam, P., Arumugam, S., Babak, S., Bagchi, M., Bak Nielsen, A. S., Bassa, C. G., Bathula, A., Berthereau, A., Bonetti, M., Bortolas, E., Brook, P. R., Burgay, M., Caballero, R. N., Chalumeau, A., Champion, D. J., Chanlaridis, S., Chen, S., Cognard, I., Dandapat, S., Deb, D., Desai, S., Desvignes, G., Dhanda-Batra, N., Dwivedi, C., Falxa, M., Ferdman, R. D., Franchini, A., Gair, J. R., Goncharov, B., Gopakumar, A., Graikou, E., Grießmeier, J. M., Guillemot, L., Guo, Y. J., Gupta, Y., Hisano, S., Hu, H., Iraci, F., Izquierdo-Villalba, D., Jang, J., Jawor, J., Janssen, G. H., Jessner, A., Joshi, B. C., Kareem, F., Karuppusamy, R., Keane, E. F., Keith, M. J., Kharbanda, D., Kikunaga, T., Kolhe, N., Kramer, M., Krishnakumar, M. A., Lackeos, K., Lee, K. J., Liu, K., Liu, Y., Lyne, A. G., McKee, J. W., Maan, Y., Main, R. A., Mickaliger, M. B., Nitu, I. C., Nobleson, K., Paladi, A. K., Parthasarathy, A., Perera, B. B. P., Perrodin, D., Petiteau, A., Porayko, N. K., Possenti, A., Prabu, T., Quelquejay Leclere, H., Rana, P., Samajdar, A., Sanidas, S. A., Sesana, A., Shaifullah, G., Singha, J., Speri, L., Spiewak, R., Srivastava, A., Stappers, B. W., Surnis, M., Susarla, S. C., Susobhanan, A., Takahashi, K., Tarafdar, P., Theureau, G., Tiburzi, C., van der Wateren, E., Vecchio, A., Venkatraman Krishnan, V., Verbiest, J. P. W., Wang, J., Wang, L., & Wu, Z. (2023). The second data release from the European Pulsar Timing Array III. Search for gravitational wave signals. *arXiv e-prints*, (p. arXiv:2306.16214).

Barnes, J., & Hut, P. (1986). A hierarchical O(N log N) force-calculation algorithm. , *324*(6096), 446–449.

Begelman, M. C., Blandford, R. D., & Rees, M. J. (1980a). Massive black hole binaries in active galactic nuclei. , *287*(5780), 307–309.

Begelman, M. C., Blandford, R. D., & Rees, M. J. (1980b). Massive black hole binaries in active galactic nuclei. , *287*, 307–309.

Binney, J., & Tremaine, S. (1987). *Galactic dynamics*.

Binney, J., & Tremaine, S. (2008). *Galactic Dynamics: Second Edition*.

Bonetti, M., Bortolas, E., Lupi, A., & Dotti, M. (2021a). Dynamical evolution of massive perturbers in realistic multicomponent galaxy models I: implementation and validation. , *502*(3), 3554–3568.

Bonetti, M., Bortolas, E., Lupi, A., & Dotti, M. (2021b). Dynamical evolution of massive perturbers in realistic multicomponent galaxy models I: implementation and validation. , *502*(3), 3554–3568.

Bonetti, M., Bortolas, E., Lupi, A., Dotti, M., & Raimundo, S. I. (2020a). Dynamical friction-driven orbital circularization in rotating discs: a semi-analytical description. , *494*(2), 3053–3059.

Bonetti, M., Bortolas, E., Lupi, A., Dotti, M., & Raimundo, S. I. (2020b). Dynamical friction-driven orbital circularization in rotating discs: a semi-analytical description. , *494*(2), 3053–3059.

Bortolas, E., Bonetti, M., Dotti, M., Lupi, A., Capelo, P. R., Mayer, L., & Sesana, A. (2022). The role of bars on the dynamical-friction-driven inspiral of massive objects. , *512*(3), 3365–3382.

Bortolas, E., Gualandris, A., Dotti, M., Spera, M., & Mapelli, M. (2016). Brownian motion of massive black hole binaries and the final parsec problem. , *461*(1), 1023–1031.

Bulirsch, R., & Stoer, J. (1966). Numerical treatment of ordinary differential equations by extrapolation methods. *Numerische Mathematik*, *8*(1), 1–13.

Callegari, S., Kazantzidis, S., Mayer, L., Colpi, M., Bellovary, J. M., Quinn, T., & Wadsley, J. (2011). Growing Massive Black Hole Pairs in Minor Mergers of Disk Galaxies. , *729*(2), 85.

Capetti, A., Zamfir, S., Rossi, P., Bodo, G., Zanni, C., & Massaglia, S. (2002). On the origin of X-shaped radio-sources: New insights from the properties of their host galaxies. , *394*, 39–45.

Capuzzo-Dolcetta, R., Spera, M., & Punzo, D. (2013). A fully parallel, high precision, N-body code running on hybrid computing platforms. *Journal of Computational Physics*, *236*, 580–593.

Chandrasekhar, S. (1943a). Dynamical Friction. I. General Considerations: the Coefficient of Dynamical Friction. , *97*, 255.

Chandrasekhar, S. (1943b). Dynamical Friction. I. General Considerations: the Coefficient of Dynamical Friction. , *97*, 255.

Chatterjee, P., Hernquist, L., & Loeb, A. (2003). Effects of Wandering on the Coalescence of Black Hole Binaries in Galactic Centers. , *592*(1), 32–41.

Colpi, M. (2014). Massive Binary Black Holes in Galactic Nuclei and Their Path to Coalescence. , *183*(1-4), 189–221.

Darg, D. W., Kaviraj, S., Lintott, C. J., Schawinski, K., Sarzi, M., Bamford, S., Silk, J., Proctor, R., Andreescu, D., Murray, P., Nichol, R. C., Raddick, M. J., Slosar, A., Szalay, A. S., Thomas, D., & Vandenberg, J. (2010). Galaxy Zoo: the fraction of merging galaxies in the SDSS and their morphologies. , *401*(2), 1043–1056.

Dehnen, W. (1993). A Family of Potential-Density Pairs for Spherical Galaxies and Bulges. , *265*, 250.

Devecchi, B., & Volonteri, M. (2009). Formation of the First Nuclear Clusters and Massive Black Holes at High Redshift. , *694*(1), 302–313.

Devecchi, B., Volonteri, M., Colpi, M., & Haardt, F. (2010). High-redshift formation and evolution of central massive objects - I. Model description. , *409*(3), 1057–1067.

Devecchi, B., Volonteri, M., Rossi, E. M., Colpi, M., & Portegies Zwart, S. (2012). High-redshift formation and evolution of central massive objects - II. The census of BH seeds. , *421*(2), 1465–1475.

Di Matteo, T., Springel, V., & Hernquist, L. (2005). Energy input from quasars regulates the growth and activity of black holes and their host galaxies. , *433*(7026), 604–607.

Dosopoulou, F., & Antonini, F. (2017). Dynamical Friction and the Evolution of Supermassive Black Hole Binaries: The Final Hundred-parsec Problem. , *840*(1), 31.

Dotti, M., Colpi, M., & Haardt, F. (2006). Laser Interferometer Space Antenna double black holes: dynamics in gaseous nuclear discs. , *367*(1), 103–112.

Einstein, & Lawson. (1961). *Relativity: The Special and the General Theory.*, (pp. 330–458).

Einstein, A. (1939). On a Stationary System with Spherical Symmetry Consisting of Many Gravitating Masses. *Annals of Mathematics*, *40*, 922.

Ekers, R. D., Fanti, R., Lari, C., & Parma, P. (1978). NGC326 - A radio galaxy with a precessing beam. , *276*, 588–590.

EPTA Collaboration, InPTA Collaboration, Antoniadis, J., Arumugam, P., Arumugam, S., Babak, S., Bagchi, M., Bak Nielsen, A. S., Bassa, C. G., Bathula, A., Berthereau, A., Bonetti, M., Bortolas, E., Brook, P. R., Burgay, M., Caballero, R. N., Chalumeau, A., Champion, D. J., Chanlaridis, S., Chen, S., Cognard, I., Dandapat, S., Deb, D., Desai, S., Desvignes, G., Dhanda-Batra, N., Dwivedi, C., Falxa, M., Ferdman, R. D., Franchini, A., Gair, J. R., Goncharov, B., Gopakumar, A., Graikou, E., Grießmeier, J. M., Guillemot, L., Guo, Y. J., Gupta, Y., Hisano, S., Hu, H., Iraci, F., Izquierdo-Villalba, D., Jang, J., Jawor, J., Janssen, G. H., Jessner, A., Joshi, B. C., Kareem, F., Karuppusamy, R., Keane, E. F., Keith, M. J., Kharbanda, D., Kikunaga, T., Kolhe, N., Kramer, M., Krishnakumar, M. A., Lackeos, K., Lee, K. J., Liu, K., Liu, Y., Lyne, A. G., McKee, J. W., Maan, Y., Main, R. A., Mickaliger, M. B., Niţu, I. C., Nobleson, K., Paladi, A. K., Parthasarathy, A., Perera, B. B. P., Perrodin, D., Petiteau, A., Porayko,

N. K., Possenti, A., Prabu, T., Quelquejay Leclere, H., Rana, P., Samajdar, A., Sanidas, S. A., Sesana, A., Shaifullah, G., Singha, J., Speri, L., Spiewak, R., Srivastava, A., Stappers, B. W., Surnis, M., Susarla, S. C., Susobhanan, A., Takahashi, K., Tarafdar, P., Theureau, G., Tiburzi, C., van der Wateren, E., Vecchio, A., Venkatraman Krishnan, V., Verbiest, J. P. W., Wang, J., Wang, L., & Wu, Z. (2023). The second data release from the European Pulsar Timing Array. III. Search for gravitational wave signals. , *678*, A50.

Escala, A., Larson, R. B., Coppi, P. S., & Mardones, D. (2005). The Role of Gas in the Merging of Massive Black Holes in Galactic Nuclei. II. Black Hole Merging in a Nuclear Gas Disk. , *630*(1), 152–166.

Fabbiano, G., Wang, J., Elvis, M., & Risaliti, G. (2011). A close nuclear black-hole pair in the spiral galaxy NGC3393. , *477*(7365), 431–434.

Ferrarese, L., & Merritt, D. (2000). A Fundamental Relation between Supermassive Black Holes and Their Host Galaxies. , *539*(1), L9–L12.

Fiacconi, D., Mayer, L., Roškar, R., & Colpi, M. (2013). Massive Black Hole Pairs in Clumpy, Self-gravitating Circumnuclear Disks: Stochastic Orbital Decay. , *777*(1), L14.

Gajda, G., & Łokas, E. L. (2016). On the Tidal Radius of Satellites on Prograde and Retrograde Orbits. , *819*(1), 20.

Gebhardt, K., Bender, R., Bower, G., Dressler, A., Faber, S. M., Filippenko, A. V., Green, R., Grillmair, C., Ho, L. C., Kormendy, J., Lauer, T. R., Magorrian, J., Pinkney, J., Richstone, D., & Tremaine, S. (2000). A Relationship between Nuclear Black Hole Mass and Galaxy Velocity Dispersion. , *539*(1), L13–L16.

Genzel, R., Eisenhauer, F., & Gillessen, S. (2010). The Galactic Center massive black hole and nuclear star cluster. *Reviews of Modern Physics*, *82*(4), 3121–3195.

Ghez, A. M., Salim, S., Weinberg, N. N., Lu, J. R., Do, T., Dunn, J. K., Matthews, K., Morris, M. R., Yelda, S., Becklin, E. E., Kremenek, T., Milosavljevic, M., & Naiman, J. (2008). Measuring Distance and Properties of the Milky Way's Central Supermassive Black Hole with Stellar Orbits. , *689*(2), 1044–1062.

Gnedin, O. Y., Hernquist, L., & Ostriker, J. P. (1999). Tidal Shocking by Extended Mass Distributions. , *514*(1), 109–118.

Granato, G. L., De Zotti, G., Silva, L., Bressan, A., & Danese, L. (2004). A Physical Model for the Coevolution of QSOs and Their Spheroidal Hosts. , *600*(2), 580–594.

Gualandris, A., Dotti, M., & Sesana, A. (2012a). Massive black hole binary plane reorientation in rotating stellar systems. , *420*, L38–L42.

Gualandris, A., Dotti, M., & Sesana, A. (2012b). Massive black hole binary plane reorientation in rotating stellar systems. , *420*(1), L38–L42.

Gualandris, A., & Merritt, D. (2012). Long-term Evolution of Massive Black Hole Binaries. IV. Mergers of Galaxies with Collisionally Relaxed Nuclei. , *744*(1), 74.

Gualandris, A., Read, J. I., Dehnen, W., & Bortolas, E. (2017). Collisionless loss-cone refilling: there is no final parsec problem. , *464*(2), 2301–2310.

Gültekin, K., Richstone, D. O., Gebhardt, K., Lauer, T. R., Tremaine, S., Aller, M. C., Bender, R., Dressler, A., Faber, S. M., Filippenko, A. V., Green, R., Ho, L. C., Kormendy, J., Magorrian, J., Pinkney, J., & Siopis, C. (2009). The M-σ and M-L Relations in Galactic Bulges, and Determinations of Their Intrinsic Scatter. , *698*(1), 198–221.

Haehnelt, M. G., & Rees, M. J. (1993). The formation of nuclei in newly formed galaxies and the evolution of the quasar population. , *263*(1), 168–178.

Häring, N., & Rix, H.-W. (2004). On the Black Hole Mass-Bulge Mass Relation. , *604*(2), L89–L92.

Hashimoto, Y., Funato, Y., & Makino, J. (2003). To circularize or not to circularize?—orbital evolution of satellite galaxies. *The Astrophysical Journal*, *582*(1), 196.
URL https://dx.doi.org/10.1086/344260

Heger, A., Fryer, C. L., Woosley, S. E., Langer, N., & Hartmann, D. H. (2003). How Massive Single Stars End Their Life. , *591*(1), 288–300.

Henon, M. (1970). Numerical exploration of the restricted problem. VI. Hill's case: Non-periodic orbits. , *9*, 24–36.

Hernquist, L. (1990). An Analytical Model for Spherical Galaxies and Bulges. , *356*, 359.

Holley-Bockelmann, K., & Khan, F. M. (2015). Galaxy Rotation and Rapid Supermassive Binary Coalescence. , *810*(2), 139.

Jahnke, K., & Macciò, A. V. (2011). The Non-causal Origin of the Black-hole-galaxy Scaling Relations. , *734*(2), 92.

Just, A., Khan, F. M., Berczik, P., Ernst, A., & Spurzem, R. (2011). Dynamical friction of massive objects in galactic centres. *Monthly Notices of the Royal Astronomical Society*, *411*(1), 653–674.
URL https://doi.org/10.1111/j.1365-2966.2010.17711.x

Just, A., & Peñarrubia, J. (2005). Large scale inhomogeneity and local dynamical friction. , *431*(3), 861–877.

Katz, J. I. (1997). A Precessing Disk in OJ 287? , *478*(2), 527–529.

Kauffmann, G., Colberg, J. M., Diaferio, A., & White, S. D. M. (1999). Clustering of galaxies in a hierarchical universe - I. Methods and results at z=0. , *303*(1), 188–206.

Kauffmann, G., White, S. D. M., & Guiderdoni, B. (1993). The formation and evolution of galaxies within merging dark matter haloes. , *264*, 201–218.

Kaviraj, S., Peirani, S., Khochfar, S., Silk, J., & Kay, S. (2009). The role of minor mergers in the recent star formation history of early-type galaxies. , *394*(4), 1713–1720.

Keenan, D. W., & Innanen, K. A. (1975). Stability regions in the restricted problem. *Celestial Mechanics*, *11*, 85.

Khan, F. M., Fiacconi, D., Mayer, L., Berczik, P., & Just, A. (2016). Swift Coalescence of Supermassive Black Holes in Cosmological Mergers of Massive Galaxies. , *828*(2), 73.

Khan, F. M., Just, A., & Merritt, D. (2011). Efficient Merger of Binary Supermassive Black Holes in Merging Galaxies. , *732*(2), 89.

Khan, F. M., Mirza, M. A., & Holley-Bockelmann, K. (2020). Inward bound: the incredible journey of massive black holes as they pair and merge - I. The effect of mass ratio in flattened rotating galactic nuclei. , *492*(1), 256–267.

Khan, F. M., Preto, M., Berczik, P., Berentzen, I., Just, A., & Spurzem, R. (2012). Mergers of Unequal-mass Galaxies: Supermassive Black Hole Binary Evolution and Structure of Merger Remnants. , *749*(2), 147.

King, I. (1962). The structure of star clusters. I. an empirical density law. , *67*, 471.

Kippenhahn, R., Weigert, A., & Weiss, A. (2012). *Stellar structure and evolution*. Astronomy and Astrophysics Library. Springer.

Komossa, S., Burwitz, V., Hasinger, G., Predehl, P., Kaastra, J. S., & Ikebe, Y. (2003). Discovery of a Binary Active Galactic Nucleus in the Ultraluminous Infrared Galaxy NGC 6240 Using Chandra. , *582*(1), L15–L19.

Kormendy, J. (2013). *Secular Evolution in Disk Galaxies*, (p. 1).

Kormendy, J., & Richstone, D. (1995). Inward Bound—The Search For Supermassive Black Holes In Galactic Nuclei. , *33*, 581.

Leahy, J. P., & Williams, A. G. (1984). The bridges of classical double radio sources. , *210*, 929–951.

Lehto, H. J., & Valtonen, M. J. (1996). OJ 287 Outburst Structure and a Binary Black Hole Model. , *460*, 207.

Liu, F. K., Wu, X.-B., & Cao, S. L. (2003). Double-double radio galaxies: remnants of merged supermassive binary black holes. , *340*(2), 411–416.

Luo, Y., Ardaneh, K., Shlosman, I., Nagamine, K., Wise, J. H., & Begelman, M. C. (2018). Direct Collapse to Supermassive Black Hole Seeds with Radiative Transfer: Isolated Halos. , *476*(3), 3523–3539.

Lupi, A., Colpi, M., Devecchi, B., Galanti, G., & Volonteri, M. (2014). Constraining the high-redshift formation of black hole seeds in nuclear star clusters with gas inflows. , *442*(4), 3616–3626.

Madau, P., & Rees, M. J. (2001). Massive Black Holes as Population III Remnants. , *551*(1), L27–L30.

Magorrian, J., Tremaine, S., Richstone, D., Bender, R., Bower, G., Dressler, A., Faber, S. M., Gebhardt, K., Green, R., Grillmair, C., Kormendy, J., & Lauer, T. (1998). The Demography of Massive Dark Objects in Galaxy Centers. , *115*(6), 2285–2305.

Marconi, A., & Hunt, L. K. (2003). The Relation between Black Hole Mass, Bulge Mass, and Near-Infrared Luminosity. , *589*(1), L21–L24.

Merritt, D. (2001a). Brownian Motion of a Massive Binary. , *556*(1), 245–264.

Merritt, D. (2001b). Brownian Motion of Single and Binary Black Holes. In *AAS/Division of Dynamical Astronomy Meeting #32*, vol. 32 of *AAS/Division of Dynamical Astronomy Meeting*, (p. 02.05).

Merritt, D. (2013). *Dynamics and Evolution of Galactic Nuclei*.

Merritt, D., & Vasiliev, E. (2011). Orbits Around Black Holes in Triaxial Nuclei. , *726*(2), 61.

Meyer, L., Ghez, A. M., Schödel, R., Yelda, S., Boehle, A., Lu, J. R., Do, T., Morris, M. R., Becklin, E. E., & Matthews, K. (2012). The Shortest-Known-Period Star Orbiting Our Galaxy's Supermassive Black Hole. *Science*, *338*(6103), 84.

Michell, J. (1784). On the Means of Discovering the Distance, Magnitude, &c. of the Fixed Stars, in Consequence of the Diminution of the Velocity of Their Light, in Case Such a Diminution Should be Found to Take Place in any of Them, and Such Other Data Should be Procured from Observations, as Would be Farther Necessary for That Purpose. By the Rev. John Michell,

B. D. F. R. S. In a Letter to Henry Cavendish, Esq. F. R. S. and A. S. *Philosophical Transactions of the Royal Society of London Series I*, *74*, 35–57.

Milosavljević, M., & Merritt, D. (2001). Formation of Galactic Nuclei. , *563*(1), 34–62.

Milosavljević, M., & Merritt, D. (2003a). Long-Term Evolution of Massive Black Hole Binaries. , *596*(2), 860–878.

Milosavljević, M., & Merritt, D. (2003b). Long-Term Evolution of Massive Black Hole Binaries. , *596*(2), 860–878.

Mirza, M. A., Tahir, A., Khan, F. M., Holley-Bockelmann, H., Baig, A. M., Berczik, P., & Chishtie, F. (2017). Galaxy rotation and supermassive black hole binary evolution. , *470*(1), 940–947.

Nelson, D., Pillepich, A., Springel, V., Pakmor, R., Weinberger, R., Genel, S., Torrey, P., Vogelsberger, M., Marinacci, F., & Hernquist, L. (2019). First results from the TNG50 simulation: galactic outflows driven by supernovae and black hole feedback. , *490*(3), 3234–3261.

Nelson, D., Pillepich, A., Springel, V., Weinberger, R., Hernquist, L., Pakmor, R., Genel, S., Torrey, P., Vogelsberger, M., Kauffmann, G., Marinacci, F., & Naiman, J. (2018). First results from the IllustrisTNG simulations: the galaxy colour bimodality. , *475*(1), 624–647.

Nishizawa, A., Berti, E., Klein, A., & Sesana, A. (2016). eLISA eccentricity measurements as tracers of binary black hole formation. , *94*(6), 064020.

Nitadori, K., & Makino, J. (2008). Sixth- and eighth-order Hermite integrator for N-body simulations. , *13*(7), 498–507.

Peng, C. Y. (2007). How Mergers May Affect the Mass Scaling Relation between Gravitationally Bound Systems. , *671*(2), 1098–1107.

Perets, H. B., & Alexander, T. (2008). Massive Perturbers and the Efficient Merger of Binary Massive Black Holes. , *677*(1), 146–159.

Peters, P. C. (1964). Gravitational Radiation and the Motion of Two Point Masses. *Physical Review*, *136*(4B), 1224–1232.

Peterson, B. M. (2014). Measuring the Masses of Supermassive Black Holes. , *183*(1-4), 253–275.

Poon, M. Y., & Merritt, D. (2004). A Self-Consistent Study of Triaxial Black Hole Nuclei. , *606*(2), 774–787.

Press, W. H., & Schechter, P. (1974). Formation of Galaxies and Clusters of Galaxies by Self-Similar Gravitational Condensation. , *187*, 425–438.

Press, W. H., Teukolsky, S. A., Vetterling, W. T., & Flannery, B. P. (2002). *Numerical recipes in C++ : the art of scientific computing.*

Preto, M., Berentzen, I., Berczik, P., & Spurzem, R. (2011). Fast Coalescence of Massive Black Hole Binaries from Mergers of Galactic Nuclei: Implications for Low-frequency Gravitational-wave Astrophysics. , *732*(2), L26.

Pursimo, T., Takalo, L. O., Sillanpää, A., Kidger, M., Lehto, H. J., Heidt, J., Charles, P. A., Aller, H., Aller, M., Beckmann, V., Benítez, E., Bock, H., Boltwood, P., Borgeest, U., de Diego, J. A., De Francesco, G., Dietrich, M., Dultzin-Hacyan, D., Efimov, Y., Fiorucci, M., Ghisellini, G., González-Pérez, N., Hanski, M., Heinämäki, P., Honeycutt, R. K., Hughes, P., Karlamaa, K., Katajainen, S., Knee, L. B. G., Kurtanidze, O. M., Kümmel, M., Kühl, D., Lainela, M., Lanteri, L., Linde, J. V., Lähteenmäki, A., Maesano, M., Mahoney, T., Marchenko, S., Marscher, A., Massaro, E., Montagni, F., Nesci, R., Nikolashvili, M., Nilsson, K., Nurmi, P., Pietilä, H., Poyner, G., Raiteri, C. M., Rekola, R., Richter, G. M., Riehokainen, A., Robertson, J. W., Rodríguez-Espinoza, J. M., Sadun, A., Shakhovskoy, N., Schramm, K. J., Schramm, T., Sobrito, G., Teerikorpi, P., Teräsranta, H., Tornikoski, M., Tosti, G., Turner, G. W., Valtaoja, E., Valtonen, M., Villata, M., Wagner, S. J., Webb, J., Weneit, W., & Wiren, S. (2000). Intensive monitoring of OJ 287. , *146*, 141–155.

Quinlan, G. D. (1996). The dynamical evolution of massive black hole binaries I. Hardening in a fixed stellar background. , *1*(1), 35–56.

Rasskazov, A., & Merritt, D. (2017). Evolution of Binary Supermassive Black Holes in Rotating Nuclei. , *837*(2), 135.

Read, J. I., Wilkinson, M. I., Evans, N. W., Gilmore, G., & Kleyna, J. T. (2006). The tidal stripping of satellites. , *366*(2), 429–437.

Reardon, D. J., Zic, A., Shannon, R. M., Hobbs, G. B., Bailes, M., Di Marco, V., Kapur, A., Rogers, A. F., Thrane, E., Askew, J., Bhat, N. D. R., Cameron, A., Curyło, M., Coles, W. A., Dai, S., Goncharov, B., Kerr, M., Kulkarni, A., Levin, Y., Lower, M. E., Manchester, R. N., Mandow, R., Miles, M. T., Nathan, R. S., Osłowski, S., Russell, C. J., Spiewak, R., Zhang, S., & Zhu, X.-J. (2023). Search for an Isotropic Gravitational-wave Background with the Parkes Pulsar Timing Array. , *951*(1), L6.

Reinoso, B., Schleicher, D. R. G., Fellhauer, M., Leigh, N. W. C., & Klessen, R. S. (2020). The effects of a background potential in star cluster evolution. A delay in the relaxation time-scale and runaway collision processes. , *639*, A92.

Rodriguez, C., Taylor, G. B., Zavala, R. T., Peck, A. B., Pollack, L. K., & Romani, R. W. (2006). A Compact Supermassive Binary Black Hole System. , *646*(1), 49–60.

Salpeter, E. E. (1964). Accretion of Interstellar Matter by Massive Objects. , *140*, 796–800.

Schmidt, M. (1963). 3C 273 : A Star-Like Object with Large Red-Shift. , *197*(4872), 1040.

Schoenmakers, A. P., de Bruyn, A. G., Röttgering, H. J. A., & van der Laan, H. (2000). Radio galaxies with a 'double-double' morphology - III. The case of B1834+620. , *315*(2), 395–406.

Sellwood, J. A., & Wilkinson, A. (1993). Dynamics of barred galaxies. *Reports on Progress in Physics*, *56*(2), 173–256.

Sersic, J. L. (1968). *Atlas de Galaxias Australes*.

Sesana, A., Gualandris, A., & Dotti, M. (2011). Massive black hole binary eccentricity in rotating stellar systems. , *415*(1), L35–L39.

Sesana, A., Haardt, F., & Madau, P. (2006). Interaction of Massive Black Hole Binaries with Their Stellar Environment. I. Ejection of Hypervelocity Stars. , *651*(1), 392–400.

Sesana, A., Haardt, F., & Madau, P. (2008). Interaction of Massive Black Hole Binaries with Their Stellar Environment. III. Scattering of Bound Stars. , *686*(1), 432–447.

Shlosman, I., Choi, J.-H., Begelman, M. C., & Nagamine, K. (2016). Supermassive black hole seed formation at high redshifts: long-term evolution of the direct collapse. , *456*(1), 500–511.

Silk, J., & Rees, M. J. (1998). Quasars and galaxy formation. , *331*, L1–L4.

Sillanpaa, A., Haarala, S., Valtonen, M. J., Sundelius, B., & Byrd, G. G. (1988). OJ 287: Binary Pair of Supermassive Black Holes. , *325*, 628.

Spitzer, L. (1987). *Dynamical evolution of globular clusters*.

Springel, V., Pakmor, R., Zier, O., & Reinecke, M. (2021). Simulating cosmic structure formation with the GADGET-4 code. , *506*(2), 2871–2949.

Tremaine, S., Gebhardt, K., Bender, R., Bower, G., Dressler, A., Faber, S. M., Filippenko, A. V., Green, R., Grillmair, C., Ho, L. C., Kormendy, J., Lauer, T. R., Magorrian, J., Pinkney, J., & Richstone, D. (2002). The Slope of the Black Hole Mass versus Velocity Dispersion Correlation. , *574*(2), 740–753.

Tremaine, S., Richstone, D. O., Byun, Y.-I., Dressler, A., Faber, S. M., Grill-mair, C., Kormendy, J., & Lauer, T. R. (1994). A Family of Models for Spherical Stellar Systems. , *107*, 634.

Valtaoja, E., Teräsranta, H., Tornikoski, M., Sillanpää, A., Aller, M. F., Aller, H. D., & Hughes, P. A. (2000). Radio Monitoring of OJ 287 and Binary Black Hole Models for Periodic Outbursts. , *531*(2), 744–755.

Valtonen, M. J. (1996). Are supermassive black holes confined to galactic nuclei? *Comments on Astrophysics*, *18*, 191–206.

van den Bosch, F. C., Ogiya, G., Hahn, O., & Burkert, A. (2018). Disruption of dark matter substructure: fact or fiction? , *474*(3), 3043–3066.

Varisco, L., Bortolas, E., Dotti, M., & Sesana, A. (2021). Stellar hardening of massive black hole binaries: the impact of the host rotation. , *508*(1), 1533–1542.

Vasiliev, E., Antonini, F., & Merritt, D. (2014). The Final-parsec Problem in Nonspherical Galaxies Revisited. , *785*(2), 163.

Vasiliev, E., Antonini, F., & Merritt, D. (2015). The Final-parsec Problem in the Collisionless Limit. , *810*(1), 49.

von Hoerner, S. (1957). Internal structure of globular clusters. , *125*, 451.

von Hoerner, S. (1960). Die numerische Integration des n-Körper-Problemes für Sternhaufen. I. , *50*, 184–214.

Wang, L., Berczik, P., Spurzem, R., & Kouwenhoven, M. B. N. (2014). The Link between Ejected Stars, Hardening and Eccentricity Growth of Super Massive Black Holes in Galactic Nuclei. , *780*(2), 164.

Wang, T.-G., Zhou, H.-Y., & Dong, X.-B. (2003). 4C +01.30: An X-shaped Radio Source with a Quasar Nucleus. , *126*(1), 113–118.

Webster, B. L., & Murdin, P. (1972). Cygnus X-1-a Spectroscopic Binary with a Heavy Companion ? , *235*(5332), 37–38.

White, S. D. M. (1976). A note on the minimum impact parameter for dynamical friction involving spherical clusters. , *174*, 467–470.

White, S. D. M. (1989). Observable signatures of young galaxies. In C. S. Frenk, R. S. sEllis, T. Shanks, A. R. Heavens, & J. A. Peacock (Eds.) *The Epoch of Galaxy Formation*, vol. 264 of *NATO Advanced Study Institute (ASI) Series C*, (p. 15).

White, S. D. M., & Frenk, C. S. (1991). Galaxy Formation through Hierarchical Clustering. , *379*, 52.

White, S. D. M., & Rees, M. J. (1978). Core condensation in heavy halos: a two-stage theory for galaxy formation and clustering. , *183*, 341–358.

Yu, Q. (2002). Evolution of massive binary black holes. , *331*(4), 935–958.

Yurin, D., & Springel, V. (2014). An iterative method for the construction of N-body galaxy models in collisionless equilibrium. , *444*(1), 62–79.

Zana, T., Lupi, A., Bonetti, M., Dotti, M., Rosas-Guevara, Y., Izquierdo-Villalba, D., Bonoli, S., Hernquist, L., & Nelson, D. (2022). Morphological decomposition of TNG50 galaxies: methodology and catalogue. , *515*(1), 1524–1543.

Zel'dovich, Y. B., & Novikov, I. D. (1964). The Radiation of Gravity Waves by Bodies Moving in the Field of a Collapsing Star. *Soviet Physics Doklady*, *9*, 246.